

RETRIEVAL OF AEROSOL MICROPHYSICAL PROPERTIES FROM THE AERONET
PHOTO-POLARIMETRIC MEASUREMENTS

by

Xiaoguang Xu

A DISSERTATION

Presented to the Faculty of
The Graduate College at the University of Nebraska
In Partial Fulfilment of Requirements
For the Degree of Doctor of Philosophy

Major: Earth & Atmospheric Sciences
(Meteorology/Climatology)

Under the Supervision of Professor Jun Wang

Lincoln, Nebraska

August, 2015

RETRIEVAL OF AEROSOL MICROPHYSICAL PROPERTIES FROM THE AERONET
PHOTO-POLARIMETRIC MEASUREMENTS

Xiaoguang Xu, Ph.D.

University of Nebraska, 2015

Adviser: Jun Wang

Atmospheric aerosols play an important role in earth climate change by scattering and absorbing solar and terrestrial radiation, and indirectly through altering the cloud formation, lifetime, and radiative properties. However, accurate quantification of these effects is in no small part hindered by our limited knowledge about the particle size distribution (PSD) and refractive index, the aerosol microphysical properties essentially pertain to aerosol optical and cloud-forming properties. The research goal of this thesis is to obtain these properties of both fine and coarse aerosol modes from the direct and diffuse polarimetric solar radiation measured by the SunPhotometer of the Aerosol Robotic Network (AERONET). We achieve so by (1) developing an inversion algorithm that integrates rigorous radiative transfer model with a statistical optimization approach, (2) conducting a sensitivity study and error budgeting exercise to examine the potential value of adding polarization to the current radiance-only inversion, and (3) performing retrievals using available AERONET polarimetric measurements.

The results from theoretical information and error analysis indicate a remarkable increase in information by adding additional polarization and/or radiances into the inversion: an overall increase of 2–5 of degree of freedom for signal comparing with radiance-only measurements. Correspondingly, retrieval uncertainty can be reduced by 79% (57%), 76% (49%), 69% (52%), 66% (46%), and 49% (20%) for the fine-mode (coarse-mode) aerosol volume concentration, the effective radius, the effective variance, the real part of refractive

index, and single scattering albedo, respectively, resulting in their retrieval errors of 2.3% (2.9%), 1.3% (3.5%), 7.2% (12%), 0.005 (0.035), and 0.019 (0.068).

In real cases, we demonstrate that our retrievals are overall consistent with current AERONET operational inversions, but can offer mode-resolved refractive index and SSA with sufficient accuracy for the aerosol composed by spherical particles. Along with the retrieval using both radiance and polarization, we also performed radiance-only retrieval to reveal the improvements by adding polarization in the inversion. Such contrast analysis indicates that with polarization, retrieval error can be reduced by over 50% in PSD parameters, by 10–30% in the refractive index, and by 10–40% in SSA, which is consistent with the theoretical results.

ACKNOWLEDGMENTS

Acknowledgment to be filled . . .

GRANT INFORMATION

The NASA Earth and Space Science Fellowship funded this project from September 2012 to August 2015. I am also grateful to the support from NASA's New Investigator Program and Radiation Science Program (to Dr. Jun Wang).

Table of Contents

| | |
|--|-------------|
| Acknowledgments | iv |
| Grant Information | v |
| List of Figures | x |
| List of Tables | xvii |
| 1 Introduction | 1 |
| 1.1 Background and Motivation | 1 |
| 1.1.1 Previous studies on aerosol microphysical retrievals | 2 |
| 1.1.2 The AERONET measurements | 3 |
| 1.1.3 Challenges and opportunities | 6 |
| 1.2 Research Goals and Thesis Outline | 10 |
| 2 Model Developments | 12 |
| 2.1 Introduction | 12 |
| 2.2 The UNL-VRTM | 14 |
| 2.2.1 Molecular scattering and absorption | 16 |
| 2.2.2 Aerosol single scattering | 18 |
| 2.2.3 Surface representations | 20 |

| | | |
|----------|---|-----------|
| 2.2.4 | Radiative transfer | 21 |
| 2.2.5 | Capability of calculating Jacobians | 22 |
| 2.3 | Model Benchmarking and Verifications | 26 |
| 2.4 | Acknowledgements | 31 |
| 3 | Inversion Theories and Algorithm | 34 |
| 3.1 | Introduction | 34 |
| 3.2 | Inversion Theories | 35 |
| 3.2.1 | Maximum a posteriori solution of an inverse problem | 35 |
| 3.2.2 | Information theory | 38 |
| 3.3 | New Research Algorithm for AERONET Inversion | 40 |
| 3.3.1 | Definition of state vector and observation vector | 42 |
| 3.3.2 | Combine a priori and smoothness constraints | 43 |
| 3.3.3 | Statistical optimized inversion | 46 |
| 3.3.4 | Characterizing retrieval error | 48 |
| 3.3.5 | Quality control of measurements | 49 |
| 3.4 | Acknowledgements | 50 |
| 4 | Information Content Analysis | 51 |
| 4.1 | Introduction | 51 |
| 4.2 | Experimental Design | 53 |
| 4.2.1 | <i>a priori</i> characteristics | 53 |
| 4.2.2 | Synthetic observations | 54 |
| 4.3 | Results | 57 |
| 4.3.1 | Error-normalized (EN) Jacobian matrix | 57 |
| 4.3.2 | Information content and retrieval error | 62 |
| 4.3.2.1 | Aerosol PSD | 64 |

| | | |
|----------|---|------------|
| 4.3.2.2 | Refractive indices | 66 |
| 4.3.2.3 | Single scattering albedo | 69 |
| 4.4 | Sensitivity of Retrieval Error to AOD and fmf_v | 70 |
| 4.5 | Summary | 75 |
| 4.6 | Acknowledgements | 77 |
| 5 | Case Demonstrations | 79 |
| 5.1 | Introduction | 79 |
| 5.2 | Selected Cases and the <i>a priori</i> Characterization | 79 |
| 5.3 | Fitting Residuals | 82 |
| 5.4 | Retrieved Aerosol Properties | 84 |
| 5.5 | Improvement over Radiance-Only Retrievals | 87 |
| 5.6 | Summary | 90 |
| 5.7 | Acknowledgements | 91 |
| 6 | Conclusions and Outlook | 92 |
| 6.1 | Conclusions | 92 |
| 6.1.1 | UNL-VRTM and new AERONET inversion algorithm | 93 |
| 6.1.2 | Potential information contained in AERONET polarization | 94 |
| 6.1.3 | Application to real retrieval | 95 |
| 6.2 | Outlook and Future Work | 95 |
| A | Derivations of Transformation Vector Π | 97 |
| B | Optimizing Species-Specified Aerosol Emissions from Satellite Measured Radiances | 103 |
| B.1 | Introduction | 103 |
| B.2 | Observational Constraints and Inversion Methodology | 108 |

| | | |
|-------------------|---|------------|
| B.2.1 | GEOS-Chem model | 109 |
| B.2.2 | GEOS-Chem adjoint modeling | 111 |
| B.2.3 | Constraints from Satellite Radiances | 112 |
| B.2.4 | Selection of emissions for optimization | 115 |
| B.2.5 | Sensitivity test with pseudo AOD observations | 116 |
| B.3 | Inversion Results | 118 |
| B.4 | Results Evaluations | 124 |
| B.4.1 | Comparison with AERONET AOD | 125 |
| B.4.2 | Comparison with MISR AOD | 127 |
| B.4.3 | Comparisons with OMI columnar SO ₂ and NO ₂ | 127 |
| B.4.4 | Comparisons with near-surface aerosol mass concentrations | 130 |
| B.4.5 | Evaluation summary | 133 |
| B.5 | Implications of Results | 134 |
| B.5.1 | SO ₂ | 135 |
| B.5.2 | NH ₃ | 136 |
| B.5.3 | NOx | 136 |
| B.5.4 | BC and OC | 138 |
| B.5.5 | Mineral dust | 138 |
| B.6 | Summary | 139 |
| B.7 | Acknowledgements | 142 |
| C | Abbreviations and Acronyms | 144 |
| D | Symbols | 145 |
| E | List of Publications Generated During PhD Study | 146 |
| References | | 147 |

List of Figures

| | | |
|-----|--|----|
| 1.1 | A photo of the CIMEL CE318 type SunPhotometer (a) and its observational modes: (b) direct-sun radiance scan, (b) sky-radiance scan on the solar almu-cantar, (c) solar principal-plane scan for sky radiance and polarization. Detail scan information are presented in Table 1.1 and text. | 4 |
| 2.1 | Flowchart of the UNL-VRTM components. See text for detail. | 15 |
| 2.2 | Some benchmark simulations by the UNL-VRTM: (a) Downward solar spectral irradiance at the TOA and the surface for solar zenith angle of 30°. (b) Total-atmosphere gas absorption optical depth in the range 0.2–0.8 μm . (c) Same as (b) but for 0.8–4 μm . (d) Optical depth of SO_2 and NO_2 in polluted cases. Also shown in (b) and (c) are the optical depth computed from Santa Barbara DISORT Atmospheric Radiative Transfer (SBDART) model [Ricchiazzi <i>et al.</i> , 1998]. The mid-latitude summer atmospheric profile is assumed [McClatchey <i>et al.</i> , 1972]. (Figure adopted from Wang <i>et al.</i> [2014].) | 27 |
| 2.3 | Degree of linear polarization ($-Q/I$) of downward radiation for a pure Rayleigh atmosphere: (a) computed by UNL-VRTM for the case analyzed in Figure 5.7 of Coulson [1988] and shown here as (b). (c)–(e) shows the comparisons of I , Q , and U computed by Coulson <i>et al.</i> [1960] and those from UNL-VRTM. In (a) and (b), A_s represents the surface albedo value. In (c) and (d), the calculation is for $\tau = 1.0$, surface albedo is 0.25, $\cos \theta_0 = 0.8$, and for 8 different viewing angles. (Figure adopted from Wang <i>et al.</i> [2014].) | 28 |

| | | |
|-----|--|----|
| 2.4 | Counterparts in Tables 3–10 of <i>Garcia and Siewert</i> [1989] for upwelling radiation on the top of the same atmospheric conditions of aerosol scattering. No gas absorption and Rayleigh scattering are considered. Note that compared here are I and Q values reported in <i>Garcia and Siewert</i> [1989] for 9 view angles (with cosine values from 0.1 to 0.9 at equal spacing of 0.1) and 3 relative azimuth angles ($0, \pi/2$, and π), which yields a total of 27 data points. For U and V , their values are reported for the same 9 viewing angles but for one relative azimuth angle ($\pi/2$) only. The calculation is performed at wavelength of 951 nm and τ of 1.0, and aerosol size distribution parameters $r_{\text{eff}} = 0.2$, $v_{\text{eff}} = 0.07$, refractive index $m_r = 1.44$, and SSA of 0.99. (Figure adopted from <i>Wang et al.</i> [2014]). | 29 |
| 2.5 | Intercomparison of Jacobians ($\partial\xi / \partial \ln x$) calculated with UNL-VRTM using the analytical method (y-axis) with those computed from UNL-VRTM using finite-difference estimates (x-axis). Here ξ is one of the Stokes parameters: I (top row), Q (middle row), and U (last row). x is one of 7 parameters associated with fine-mode aerosols: mass concentration m_A , τ_A , m_r , m_i , r_g and σ_g (of the lognormal PSD), and height (H) of peak aerosol concentration in the vertical. Note, the calculation is done for an atmosphere containing both fine- and coarse-mode aerosols as described in <i>Hess et al.</i> [1998]. (Figure adopted from <i>Wang et al.</i> [2014]). | 32 |
| 2.6 | Same as in Figure 2.5, but for coarse mode aerosols. (Figure adopted from <i>Wang et al.</i> [2014]) | 33 |
| 3.1 | The concept of an inverse problem that optimizes an estimate from observations. (Courtesy: Daniel Jacobs) | 36 |
| 3.2 | General structure of the new research inversion algorithm for the retrieval of aerosol microphysical parameters from AERONET photo-polarimetric measurements. | 42 |
| 4.1 | Volume size distribution for the aerosol types adopted for the information analysis. Relevant aerosol parameters are summarized in the Tables 4.1 and 4.2. | 54 |
| 4.2 | (a) Simulated radiances in the solar almucantar plane as a function of azimuth angle. (b) Simulated degree of linear polarization (DOLP) in the solar principal plane as a function of view zenith angle. Simulations are for the well-mixed aerosol type with columnar AOD of 1.0 at 440 nm as shown in the Table 4.2. Solar zenith angle is 55° and top abscissas show corresponding scattering angles. | 58 |

| | | |
|------|--|----|
| 4.3 | Error-normalized Jacobians of almucantar radiances I_{alm} (left column) and degree of linear polarization DOLP _{pp} (right column) with respect to retrieved aerosol parameters in the <i>fine</i> mode: (a, f) V_0 , (b, g) r_{eff} , (c, h) v_{eff} , (d, i) m_r , and (e, j) m_i . Simulations use type-II aerosols with columnar AOD of 1.0 at 440 nm and solar zenith angle of 55°. The top and bottom abscissas are respectively the scattering angle and SunPhotometer scanning geometries. | 59 |
| 4.4 | Same as Figure 4.3 but for parameters of aerosol in the <i>coarse</i> mode. | 60 |
| 4.5 | Degree of freedom for signal (DFS) as a function of solar zenith angle for retrieving all 22 parameters when using aerosol type of (a) fine-dominated, (b) well-mixed, and (c) coarse-dominated. Four differently colored-curves denote four observation scenarios defined in Table 1. Panel (d) shows the maximum scattering angles that can be reached by the almucantar and the principal-plane scans. | 63 |
| 4.6 | DFS components (left column) and retrieval uncertainty (right column) as a function solar zenith angle with different observation scenarios defined in Table 4.3. Quantities are averages for three aerosol types defined in Table 4.2, and error bars represent one fifth of standard deviation. Three rows from top to bottom are respectively for retrieving V_0 , r_{eff} , and v_{eff} . In each panel, shown in the left is for the fine mode and in the right is for the coarse mode. | 65 |
| 4.7 | Same as Figure 4.6 but for DFS components (a-b) and retrieval uncertainty (c-d) for retrieving real part refractive index m_{real} in four wavelength bands. (a) and (c) are for the fine aerosol mode, while (b) and (d) for the coarse mode. | 67 |
| 4.8 | Same as Figure 4.7 but for retrieving imaginary part refractive index m_i | 68 |
| 4.9 | Contours of DFS as a function of fmf_v and AOD in scenarios I1 (a) and P1 (b). (c) the difference of DFS between (a) and (b). Simulations are for solar zenith angle of 55°. The top abscissa denotes Ångström exponent (AE). | 71 |
| 4.10 | Retrieval uncertainties as a function of fmf_v (or AE) and AOD for each individual aerosol parameters (V_0 , r_{eff} , v_{eff} , m_r , m_i , and ω_A)in the both <i>fine</i> (a-f)and <i>coarse</i> (g-l) modes. Two sub-panels in each panel indicate observations in the scenarios I1 and P1, respectively. Simulations are for solar zenith angle of 55°. The x- and y-axis are identical to those in Figure 4.9. Relative uncertainties are shown for V_0 , r_{eff} and v_{eff} , while absolute errors for m_r , m_i , and ω_A . Retrieval errors for m_r , m_i , and ω_A are averaged values over the four spectral bands. | 72 |

| | | |
|-----|---|-----|
| 5.1 | Climatology of aerosol properties over the Beijing_RADI site derived from AERONET daily inversion products during 2011–2013. The variables are shown as functions of the fine-mode-fraction in terms of the aerosol volume, or fmf_v . Eight bins are applied for fmf_v from 0 to 0.8 with an increment of 0.1. The six panels are: (a) Histogram of used data; (b) the Ångström exponents (AE) derived from from 870 to 1020 nm (red) and from 440 to 870 nm (green) wavelength pairs; (c) the effective radius for aerosols in the fine (red) and coarse (green) mode; (d) the effective variance in the fine (red) and coarse (green) mode (green); (e) the real part of the refractive index at 440, 675, 870, and 1020 nm; and (f) the imaginary part of the refractive index and aerosol SSA at the same wavelengths. | 81 |
| 5.2 | a) Measured almucantar normalized radiances. (b) Measured DOLP in the solar principal plane. (c) Fitting residuals for almucantar radiances by the P-type inversion (solid curves) and I-type inversion (crosses). (d) Same as panel (c), but for fitting the residuals of principal-plane DOLP. Four colors indicate different wavelengths: blue for 440 nm, green for 675 nm, red for 870 nm, and orange for 1020 nm. Gray areas in panels c–d indicate the measurement uncertainty. | 83 |
| 5.3 | Retrieved aerosol volume size distribution (PSD) and refractive index compared with Dubovik00&06 inversions (gray). P-type and I-type inversions are represented by green and red colors, respectively. In panels d–i, the retrievals are shown for aerosols in both fine (dotted) and coarse (dashed) modes, as well as bulk averages (solid). The PSD relevant quantities for panels a–c are summarized in Table 5.3. | 86 |
| 5.4 | Same as Figure 5.3, but for derived aerosol SSA and Asy. | 87 |
| B.1 | Flowchart of the proposed top-down inversion framework [Xu <i>et al.</i> , 2013]. | 109 |
| B.2 | The 0.65 μm AOD retrieved by [Wang <i>et al.</i> , 2010] compared with the MODIS operational collection 5 AOD products. (a) and (b) are their two-month averages for the period of April–May, 2008. The correspondong two-month averages of 0.65- μm AOD collected at size AERONET sites are color-coded as circles. (c) and (d) are their scatterplot against AOD observed from AERONET sites indicated on the above map. [Figure adopted from Wang <i>et al.</i> , 2010]. | 114 |

| | | |
|-----|--|-----|
| B.3 | Relative changes in posterior aerosol emissions from <i>a priori</i> in the pseudo-observation experiment. Six panels are respectively for anthropogenic emissions of SO ₂ , NH ₃ , NOx, BC, and OC, and mineral dust from both natural and anthropogenic sources. The red box in panel (a) indicates the region where AOD observations are selected. [Figure adopted from Xu <i>et al.</i> , 2013] | 117 |
| B.4 | Comparison of the prior (a) and posterior (b) GEOS-Chem (GC) simulation of 0.65 μm AOD with the AOD at the same wavelength retrieved from MODIS reflectance using GEOS-Chem aerosol optical properties (c) averaged for the period of April 2008. Satellite retrievals with 10 km by 10 km at nadir are aggregated to GEOS-Chem grid cells; and the model AOD are sampled coincidentally with those retrievals. Panel (d) and (e) respectively show the difference of prior and posterior simulated from the satellite retrieved AODs. The red box in panel (c) indicates the region where AOD observations are selected. [Figure adopted from Xu <i>et al.</i> , 2013] | 119 |
| B.5 | (a) Time series of the spatially averaged daily MODIS AOD retrievals (purple) for April 2008 over the Eastern China, compared by the prior (orange) and posterior (green) spatial averaged daily GEOS-Chem AOD that are sampled in the MODIS AOD tempo-spatial space. (b) Time series of the expected daily AOD adjustments (orange) that are the differences between MODIS AOD and the prior GEOS-Chem AOD and their real adjustments (green) that are the differences of posterior from prior GEOS-Chem AOD. (c) Time series of the prior (orange) and posterior (green) daily dust emissions over China for April 2008. [Figure adopted from Xu <i>et al.</i> , 2013] | 120 |
| B.6 | The prior (or bottom-up based, left column), optimized (or top-down constrained, middle column) aerosol emissions over China for the period of April 2008, and their relative differences (right column). Six rows from top to bottom are respectively for anthropogenic emissions of SO ₂ , NH ₃ , NOx, BC, and OC, and mineral dust from both natural and anthropogenic sources. [Figure adopted from Xu <i>et al.</i> , 2013] | 122 |

| | |
|--|-----|
| B.7 (a – i) Scatterplots of GEOS-Chem AOD versus AERONET AOD at $0.55 \mu\text{m}$ prior (red scatters) and posterior (green scatters) to the aerosol emission optimization over nine stations. AERONET AODs are 3-hour averages following the GEOS-Chem output frequency. (j) The overall comparison for eight AERONET sites excluding Beijing. Also shown are the number of valid sampled pairs (n), correlation coefficients (R), bias, and root-mean-square-error (rmse). | 126 |
| B.8 Comparison of the prior and posterior GEOS-Chem simulation of $0.55 \mu\text{m}$ AOD with the level 3 MISR $0.55 \mu\text{m}$ AOD for the period April 2008. (a) The prior GEOS-Chem $0.55 \mu\text{m}$ AOD that are sampled coincidentally with MISR AODs for the period of April 2008. Also overlaid circles are the monthly AOD averages at $0.55 \mu\text{m}$ observed from the nine AEORNET sites shown in Figure B.7. (b) Same as (a) but for the monthly average of posterior GEOS-Chem AOD. (c) Monthly average of the Level 3 daily MISR $0.55 \mu\text{m}$ AOD. (d) Scatter plot the GEOS-Chem AOD versus the MISR AOD before (red scatters) and after optimization (green scatters), in which each point indicates an AOD pair over a model grid cell with value over 0.2. Also shown are the statistics including number of sampled pairs (n), correlation coefficient (R), bias and root-mean-square-error (rmse). Comparisons of the monthly GEOS-Chem AOD versus AERONET AOD are also included as the black circles; each circle indicates an AOD pair over an individual site. [Figure adopted from Xu <i>et al.</i> , 2013] | 128 |
| B.9 Same as figure B.8 but for comparison of the GEOS-Chem SO_2 simulation with OMI column SO_2 retrievals for the period of April 2008. The OMI planetary boundary layer (PBL) column SO_2 from the Level 3 daily products with 0.25° by 0.25° resolutions are aggregated into GEOS-Chem grid cells. | 129 |
| B.10 Same figure B.8 but for comparison of the GEOS-Chem NO_2 simulation with OMI column NO_2 retrievals for the period of April 2008. The OMI tropospheric column NO_2 from Level 2 daily products with 0.25° by 0.25° resolutions are aggregated into GEOS-Chem grid cells. | 130 |
| B.11 Comparison of the GEOS-Chem surface mass concentration of sulfate-nitrate-ammonium (SNA) aerosols with ground-based observations over Qingdao (120.34°E , 36.06°N), China. Discontinuity in time series is due to missing or quality filtered observations. | 131 |

| | |
|--|-----|
| B.12 Time serial plot of the GEOS-Chem simulated surface PM ₁₀ concentrations by prior (red) and posterior (red) aerosol emissions compared with the <i>in situ</i> measured PM ₁₀ (black) over Zhangye (a) and SACOL (b) stations for 15 – 30 April 2008; also shown are the average values over same the period. Discontinuity in time series is due to missing or quality filtered observations. | 132 |
| B.13 Taylor diagram for the model evaluations before (squares) and after (circles) optimization when comparing against (1) AERONET AOD at 0.55 μm , (2) MISR 0.55 μm AOD, (3) OMI column SO ₂ , (4) OMI column NO ₂ , (5) surface SNA concentrations at Qingdao site, and (6) surface PM ₁₀ concentrations measured at Zhangye and SACOL sites. The color coded on each point indicates the relative bias. It should be noted that the ratio of standard deviations and correlation coefficient between prior GEOS-Chem simulated and measured surface PM ₁₀ over Zhangye and SACOL are 6.5 and 0.45, which makes the point number 6 for the prior simulation far beyond the range of this Taylor diagram. | 134 |
| B.14 Change of April monthly 0.55 μm AOD from 2006 to 2008 from MODIS (a) and MISR (b) Level 3 daily products. [Figure adopted from Xu <i>et al.</i> , 2013] . . | 135 |

List of Tables

| | | |
|-----|--|-----|
| 1.1 | Measurement sequences of the CIMEL CE318 SunPhotometer. | 5 |
| 2.1 | Elements of transformation vector for various aerosol single scattering parameters (composite of fine and coarse mode). | 24 |
| 2.2 | Elements of transformation vector for various microphysical parameters of fine and coarse mode aerosols ^a | 25 |
| 3.1 | AERONET observation characteristics. | 43 |
| 3.2 | State vector elements and associated constraints for inversion. ^a | 44 |
| 4.1 | The aerosol parameters defined for both fine and coarse aerosol modes ^a | 52 |
| 4.2 | The aerosol scenarios adapted for numerical experiments ^a | 53 |
| 4.3 | List of scenarios of AERONET observations used for information content analysis. | 55 |
| 4.4 | Error for retrieved and derived parameters among <i>a priori</i> , <i>a posteriori</i> , and Glory characterization ^a | 69 |
| 4.5 | Required aerosol conditions (τ_{A440} and AE) to achieve anticipated retrieval accuracy $\langle \epsilon \rangle$ for observations in scenario I1 and P1. | 74 |
| 5.1 | Main characteristics of case studies in this work. | 80 |
| 5.2 | Summary of measurement fitting errors. | 84 |
| 5.3 | PSD-related parameters retrieved by our P-type inversion, compared with values from the AERONET Dubovik00&06 inversion. | 88 |
| 5.4 | Errors on the retrieved and derived parameters from both types of inversion ^a . . . | 89 |
| B.1 | Prior, posterior, and perturbed aerosol emissions over China in the pseudo experiment. | 118 |
| B.2 | List of prior and posterior aerosol emissions in China during April 2008. . . . | 121 |
| B.3 | Test of the sensitivity of optimization with respect to prescribed <i>a priori</i> error. . | 124 |

CHAPTER 1

INTRODUCTION

1.1 Background and Motivation

Atmospheric aerosols play a crucial role in global climate change. They affect earth's energy budget directly by scattering and absorbing solar and terrestrial radiation, and indirectly through altering the cloud formation, lifetime, and radiative properties [[Haywood and Boucher, 2000](#); [Ramanathan et al., 2001](#)]. However, quantification of these effects in current climate models is fraught with uncertainties. The global average of the aerosol effective radiative forcing were estimated to range from -0.1 to -1.9 Wm^{-2} with the best estimate of -0.9 Wm^{-2} [[Boucher et al., 2013](#)], indicating that the cooling effects of aerosol might counteract the warming effects of $1.82 \pm 0.19 \text{ Wm}^{-2}$ caused by the increase of carbon dioxide since the industrial revolution [[Myhre et al., 2013](#)]. The climate effects of aerosol particles depend on their geographical distribution, optical properties, and efficiency as cloud condensation nuclei and ice nuclei. Key quantities pertain to the aerosol optical and cloud-forming properties include particle size distribution (PSD), chemical composition, mixing state, and morphology [[Boucher et al., 2013](#)]. While the daily aerosol optical depth (AOD) can be well measured from current satellite and ground-based remote sensing instrumentations [e.g., [Holben et al., 1998](#); [Kaufman et al., 2002](#)], the accurate quantification of aerosol ERF is in no small part hindered by our limited knowledge about the aerosol PSD and refractive index (describing chemical composition and mixing state).

To fully understand the role of aerosol particles in global climate change, further development in observations along with retrieval algorithms for these aerosol microphysical properties from different platforms are thus highly needed [Mishchenko *et al.*, 2004], and the focus of this two-part series study is the characterization of aerosol properties from ground-based passive remote sensing.

1.1.1 Previous studies on aerosol microphysical retrievals

There have been continuous efforts in determining aerosol microphysical properties from ground-based measurements of direct and/or diffuse solar radiation since Ångström [1929] first suggested an empirical relationship between the spectral dependency of extinction coefficients and the size of aerosol particles. Over thirty years later, Curcio [1961] inferred the aerosol PSD from the spectral particulate extinction coefficients in the visible and near-infrared regions. Soon with the effective numerical inversion technique developed by Phillips [1962] and Twomey [1963] specifically for error-involved inverse problem, a number of studies explored the use of either spectral attenuations or scattered radiances (in a small range of scattering angles) to determine the aerosol PSD [Twomey and Howell, 1967; Yamamoto and Tanaka, 1969; Dave, 1971; Grassl, 1971; Herman *et al.*, 1971; King *et al.*, 1978]. Shaw [1979] and Nakajima *et al.* [1983] were among the first studies that have combined optical scattering measurements with spectral extinctions to recover particle size spectrum. Kaufman *et al.* [1994] suggested that useful information is contained in the sky radiances of larger scattering angles for retrieval of the aerosol scattering phase function and PSD. The first operational retrieval algorithm for aerosol microphysical properties was introduced by Nakajima *et al.* [1996], when the multi-band automatic sun- and sky-scanning radiometer was deployed in the AErosol RObotic NETwork, or the AERONET [Holben *et al.*, 1998]. All of above mentioned methods treated aerosol particles as homogeneous

spheres and with refractive index assumed a priori, even though the refractive index can highly impact the optical characteristics, especially the scattering [Hansen and Travis, 1974]. Tanaka *et al.* [1982, 1983] developed an inversion library method to estimate the complex refractive index and PSD simultaneously from measurements of scattered radiances polarized in the perpendicular and parallel directions. Another concept for determining refractive index from both direct and diffuse angular radiances was developed by Wendisch and Von Hoyningen-Huene [1994] and Yamasoe *et al.* [1998], which were based on the fact that sensitivities of scattered radiances to the PSD and those to the refractive index are dominated on different scattering-angular regions. The current AERONET operational inversion algorithm was developed by Dubovik and King [2000], which has heritage from algorithms developed by King *et al.* [1978] and Nakajima *et al.* [1983, 1996] but was implemented for simultaneous retrieval of particle size distribution and complex refractive index with sophisticated inclusion of multiple a priori constraints. Dubovik *et al.* [2002a, 2006] further implemented the spheroids in the particle shape consideration for desert dust in the retrieval, and added fractional volume of non-spherical particles to the inversion products.

1.1.2 The AERONET measurements

With over 400 locations around the word, most AERONET sites are equipped with an automatic sun and sky scanning spectral radiometer, or the CIMEL CE318 type SunPhotometer (Figure 1.1a), to routinely measure direct and diffuse solar radiation in various atmospheric window channels [Holben *et al.*, 1998]. As listed in Table 1.1 and illustrated in Figure 1.1, these measurements include direct sun radiances, sky radiance on both the solar almucantar and principal planes, as well as the optional polarization of sky light on the solar principal plane.

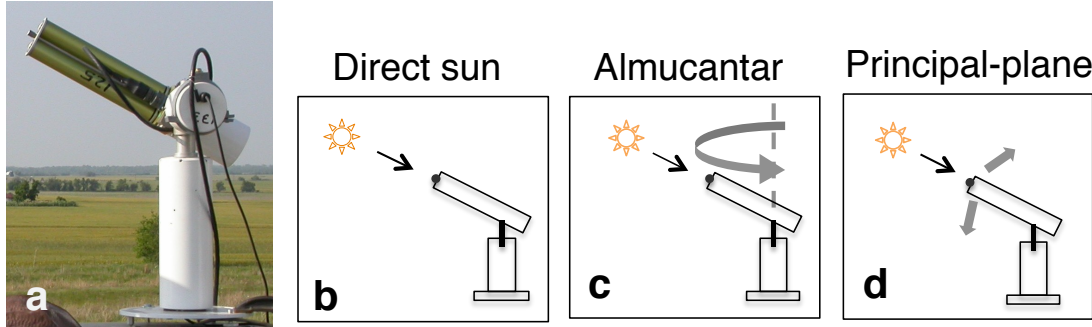


Figure 1.1: A photo of the CIMEL CE318 type SunPhotometer (a) and its observational modes: (b) direct-sun radiance scan, (b) sky-radiance scan on the solar almucantar, (c) solar principal-plane scan for sky radiance and polarization. Detail scan information are presented in Table 1.1 and text.

Direct sun radiances at various atmospheric window channels from the ultra-violet (UV) to near-infrared (NIR) are used to infer the spectral AODs with the Beer-Lambert-Bouguer Law [Holben *et al.*, 1998; Smirnov *et al.*, 2000]. Depending on site-specific instruments, AOT values are typically reported at 7 wavelengths centered at 340 nm, 380 nm, 440 nm, 500 nm, 675 nm, 870 nm, and 1020 nm. Their calibration errors are believed to as small as 0.01 for visible and NIR bands and 0.02 for UV bands.

Sky radiance measurements, which are performed at 440, 670, 870, and 1020-nm bands with full width spectrum at half maximum (FWHM) of 10 nm, are acquired from both solar almucantar and solar principal plane. An almucantar is a series of measurements taken at the viewing angle of the sun for 76 specified relative azimuthal angles (Table 1.1). To achieve a wide enough range of scattering angles, almucantar scans are usually made at an optical air mass of 1.7 or more (corresponding to solar zenith angle larger than about 50°). The principal-plane sequence for each spectrum performs right after almucantar scans. It begins with a sun observation, moves 6° below the sun-ray, sweeps up through the sun, and ends at a scattering angle of 150° or viewing angle achieves horizon, collecting radiances from up to 42 viewing angles. Hereinafter, we will use I_{alm} and I_{ppl} to represent the sky radiances

Table 1.1: Measurement sequences of the CIMEL CE318 SunPhotometer.

| | Spectra (nm) | Viewing Geometry ($^{\circ}$) | Applications |
|---|---|--|---|
| Direct sun | 340–1020 340–1640 ^a | Target to the sun | AOD, P_w , AE |
| Almucantar (I_{alm}) | 440, 675, 870, 1020 (340, 380, 500, 1640) ^a | Azimuth angles relative to Sun: 6, 5, 4.5, 4, 3.5, 3, 2.5, 2, -2, -2.5, -3, -3.5, -4, -4.5, -5, -6, -8, -10, -12, -14, -16, -18, -20, -25, -30, -35, -40, -45, -50, -60, -70, -80, -90, -100, -110, -120, -130, -140, -160, -180 (Duplicate above sequence for a complete counter clockwise rotation to -6) | PSD, m_r , m_i , SSA, phase function |
| Principal- plane (I_{pp}) | Same as above | Scattering angle from Sun: -6, -5, -4.5, -4, -3.5, -3, -2.5, -2, 2, 2.5, 3, 3.5, 4, 4.5, 5, 6, 8, 10, 12, 14, 16, 18, 20, 25, 30, 35, 40, 45, 50, 60, 70, 80, 90, 100, 110, 120, 130, 140 (negative is below the Sun) | Same as above |
| Polarization (I_{pp} , DOLP _{pp}) | 870, (340, 380, 440, 500, 675, 870, 1020, 1640) ^a | Zenith angle on the solar principal plane: -85, -80, -75, -70, -65, -60, -55, -50, -45, -40, -35, -30, -25, -20, -15, -10, -5, 5, 10, 15, 20, 25, 30, 35, 40, 45, 50, 55, 60, 65, 70, 75, 80, 85 (negative is in the anti-solar direction) | Not used yet |

^aAdditional measurements taken by the newer-generation CIMEL-318DP SunPhotometer.

from the solar almucantar and solar principal plane, respectively.

These sky radiance data are used in the current AEROENT operational inversion algorithm [Dubovik and King, 2000; Dubovik et al., 2006] (hereafter Dubovik00&06) to derive: (1) the aerosol particle size distribution (PSD) in terms of the aerosol volume (in the atmospheric column) at 22 size bins, (2) the fractional volume of non-spherical particles, and (3) the complex refractive index assumed to be independent of particle size. From those microphysical parameters, the Dubovik00&06 algorithm computes the aerosol single scattering albedo (SSA) and the phase function. Uncertainties in the AERONET inversion products are 15–100% for the bin-based PSD parameters, 0.025–0.05 for real-part refractive index and 0.03 for SSA [Dubovik et al., 2000].

Light polarization measurements are performed optionally over many sites. They are measured by the SunPhotometer with three polarizers placed 60° between each axial direc-

tion. The total radiance is derived by

$$I_{\text{pp}} = \frac{2}{3} (I_1 + I_2 + I_3), \quad (1.1)$$

where I_1 , I_2 , and I_3 are radiance with these three polarizers, respectively. The degree of linear polarization (DOLP) of skylight is inferred by

$$\text{DOLP}_{\text{pp}} = \frac{2(I_1^2 + I_2^2 + I_3^2 - I_1 I_2 - I_2 I_3 - I_1 I_3)^{(1/2)}}{I_1 + I_2 + I_3}. \quad (1.2)$$

It should be noted that we prefer to use DOLP_{pp} instead of polarized radiance in our inversion, since as a relative quantity it is more accurate. Polarization measurements are made every hour (right after principal plane scans) at 870 nm in the principal plane at 5° increments between viewing zenith angle of -85° and $+85^\circ$. These measurements are optional depending on the instrument version and configuration, and are currently available mostly over European and African stations. Recently, multi-spectral polarizations have also been taken with a newer-generation SunPhotometer (CIMEL CE318-DP) at some sites [[Li et al., 2009](#)] and the UAE² fields campaign [[Reid et al., 2008](#)]. Here we focus our study on using multi-spectral polarizations for the inversion of aerosol parameters.

1.1.3 Challenges and opportunities

While the AERONET AOD and other inversion products have been widely used to study the climatology of aerosol optical properties [[Dubovik et al., 2002b; Levy et al., 2007a](#)] and for the development and validation of aerosol retrieval algorithms for satellite sensors such as the Moderate Resolution Imaging Spectrometer (MODIS) [[Kaufman et al., 1997; Remer et al., 2005; Levy et al., 2007b, 2010; Wang et al., 2010](#)] and the Multi-angle Imaging SpectroRadiometer (MISR) [[Diner et al., 1998; Kahn et al., 2010](#)], the AERONET

operational algorithm also faces: (i) challenges in evaluation of aerosol data either retrieved from newer-generation satellite sensors or simulated from chemistry transport models, and (ii) opportunities to improve the retrieval through the use of multi-spectral polarization measurements that are now available at a few sites and will be made available at more sites as part of the AERONET future research development (<http://aeronet.gsfc.nasa.gov>). These challenges and opportunities, as further described below, are also the motivation for us to develop a new research algorithm.

The first challenge is that newer-generation satellite sensors are expected to offer aerosol microphysical products with accuracy that is equivalent to, if not higher than, that of the current AERONET microphysical products. For instance, the Aerosol Polarimetry Sensor (APS) for the NASA Glory mission, through measuring the first three Stokes vector elements simultaneously from 250 viewing angles at nine spectral bands (410, 443, 556, 670, 865, 910, 1370, 1610, and 2200 nm), was designed to retrieve aerosol effective radius (r_{eff}), effective variance (v_{eff}), and spectral complex index of refraction for both fine and coarse modes [Mishchenko *et al.*, 2007]. While no actual product is available because of the failure of Glory launch, several case studies with the APS's prototype airborne sensor, RSP (the Remote Sensing Polarimeter), demonstrated feasibility of APS algorithm [Chowdhary *et al.*, 2002, 2005; Mishchenko *et al.*, 2004; Waquet *et al.*, 2009]. At least in the case of spherical particles, the accuracy of APS's bi-modal aerosol products was expected to be 10% for r_{eff} , 40% for v_{eff} , 0.02 for m_r , and 0.03 for the SSA (ω_A) [Mishchenko *et al.*, 2007]. Some of these accuracy expectations are unlikely to be matched by existing ground-based and in situ instruments, including those at the AERONET sites. Moreover, the current AERONET retrieval of the refractive index and the ω_A are not recommended to use when the 440-nm AOD is lower than 0.4 [Holben *et al.*, 2006] due to expected limited accuracy identified in the detailed sensitivity study by [Dubovik *et al.*, 2000].

The second challenge is associated with the inconsistency in assumptions of PSD that

exists between current AERONET inversion products and satellite retrievals on the one hand, and the aerosol models used by climate models on the other hand. Specifically, the Dubovik00&06 algorithm retrieves the aerosol PSD on in 22 discrete size bins. In contrast, a continuous PSD function (e.g., lognormal) is usually assumed in satellite retrieval algorithms, such as those for APS/RSP [Mishchenko *et al.*, 2007; Waquet *et al.*, 2009] and the POLDER/PARASOL algorithm [Hasekamp *et al.*, 2011]. Also, aerosol microphysical properties are usually calculated with continuous PSD assumptions in many chemistry transport models, such as GEOS-Chem [Drury *et al.*, 2010; Wang *et al.*, 2010] and the GOCART model [Chin *et al.*, 2002]. Clearly, the actual aerosol PSD is never a perfect lognormal distribution, but neither is it discrete. At least from the scattering perspective, the aerosol PSD can be well characterized with an effective radius r_{eff} and an effective variance v_{eff} , while the specific function of the PSD is shown to be much less important [Hansen and Travis, 1974]. In other words, since the retrieval is based on the information content in the particle optical scattering, the most relevant size parameters, regardless of the PSD shape, should be r_{eff} and v_{eff} , at least for spherical particles.

The third challenge is that the assumption of a size-independent refractive index (and SSA) in Dubovik00&06 is not in line with the majority of counterpart satellite retrieval algorithms [e.g., Mishchenko *et al.*, 2007; Hasekamp *et al.*, 2011; Martonchik *et al.*, 2009], which often uses different refractive indices for various individual aerosol modes. In many cases, tropospheric aerosol is a mixture of modes with substantially different refractive indices. For example, smoke from biomass burning can be mixed with mineral dust over western coastal North Africa [Yang *et al.*, 2013]. Furthermore, the assumption of size-independent refractive index can lead to errors in the retrieval of the size distributions when the refractive indices for fine- and coarse-mode aerosols differ substantially [Dubovik *et al.*, 2000; Chowdhary *et al.*, 2001]. Thus, a mode-resolved parameterization of the refractive index in an aerosol retrieval algorithm not only can facilitate the validation of satellite

products and chemistry transport models, but also is expected to improve the accuracy of PSD and SSA retrievals for each mode. [Dubovik *et al.*, 2000] have tested the possibility of retrieving separated refractive indices of fine and coarse modes, however, they concluded that the retrieval of bi-modal refractive indices is essentially non-unique due to limited information in the AERONET radiance-only observations.

Therefore, this work aims to developing an algorithm to retrieve the aerosol microphysical properties of both fine and coarse aerosol modes, which embraces the future opportunities of deploying polarization measurements through AERONET, and ameliorates the aforementioned limitations in the Dubovik00&06 algorithm by incorporating both radiance and polarization data. Polarization measurements contain valuable information on aerosol microphysical properties [Mishchenko and Travis, 1997], as the polarization of the scattered light is highly sensitive to aerosol size and refractive index [Hansen and Travis, 1974; Mishchenko *et al.*, 2002]. We note, however, their conclusions were based on consideration of spherical aerosol particles and were primarily from a theoretical point of view. In contrast, the studies by Dubovik *et al.* [2006] and Deuzé *et al.* [1993, 2001] revealed serious limitation of polarimetric retrieval of the properties for the coarse mode, especially non-spherical aerosols. Moreover, Dubovik *et al.* [2006] have shown that while the polarimetric observation of fine particles and large spheres are highly sensitive to the real part of refractive index, even they have non-negligible sensitivity to particle shape. Therefore, adding polarization measurements to the inversion has great potential to improve the accuracy of AERONET microphysical retrievals, provided that the difficulty of representing aerosol particle shapes is recognized or adequately addressed. In these regards, most of the past efforts seem to suggest clear improvements in characterization of fine mode aerosol using polarimetric observations. For example, Li *et al.* [2009], based upon the Dubovik00&06 algorithm, demonstrated the possibility to reduce errors in the fine-mode size distribution, real part of the refractive index, and particle shape parameters.

1.2 Research Goals and Thesis Outline

As discussed above, this dissertation seeks to contribute an improved research algorithm that retrieves aerosol microphysical properties from AERONET measurements of light radiance and polarization, with emphasis on elucidating the potential value of polarization measurements. It does so by pursuing the following three objectives:

- 1. Develop ground-based inversion algorithms for the retrieval of aerosol refractive indices and particle size distribution from a combined use of direct and diffuse solar radiation measurements from AERONET.*

Retrieving aerosol information from remote sensing observation involves two type of development, i.e., the forward modeling and inverse modeling. In Chapter 2, I present a unified radiative transfer model—UNL-VRTM—that we have developed specifically for inversion of aerosol properties from remote sensing measurements [[Wang et al., 2014](#)]. The key feature of UNL-VRTM is that it not only simulates the polarimetric radiation in the atmosphere but also, more importantly, can compute the analytical derivatives of these radiation fields with respect to aerosol microphysical parameters. In the subsequent chapter, I describe an inversion algorithm that is developed by integrating the UNL-VRTM with statistically optimization approach to retrieve 22 aerosol microphysical parameters from the AERONET measured multi-spectral and multi-angular light radiance and polarization.

- 2. Conduct a sensitivity study and error budgeting exercise to characterize retrieval accuracy and error sources.*

In order to explore the potential of the AERONET polarization measurements for improving aerosol microphysical retrieval, our inversion testbed is used to examine the information content of these measurements with and without radiation in the

Chapter 4. The analysis focuses on how the added polarization measurements impact on the retrieval accuracy the in aerosol particle size distribution, spectral refractive index, and single scattering albedo. We also investigate the how the added polarization measurements can reduce the retrieval error for these properties.

3. *Perform ground-based retrievals using available AERONET polarimetric measurements.*

In Chapter 5, I applied our new research algorithm to a suite of photo-polarimetric measurements taken from the new-generation SunPhotometer at the Beijing_RADI AERONET station. In order to demonstrate the value of adding polarization measurements, we performed aerosol retrievals from radiance measurements only, in addition to the retrievals using both radiance and polarization measurements.

CHAPTER 2

MODEL DEVELOPMENTS

2.1 Introduction

Retrieving aerosol information from remote sensing observation involves two types of development, i.e., the forward modeling and the inverse modeling. Mathematically, the forward modeling constructs a complete physical system to predict the outcome of measurements. The inverse modeling uses the actual measurements to infer the values of the parameters that characterize the system. The focus of this chapter is the development of a forward model that can accurately simulate the multi-spectral and multi-angular polarimetric quantities measured by the AERONET SunPhotometer. In the following text of this section, I present the general physics of light propagation within the atmosphere. Then I describe the forward model (UNL-VRTM) in section 2.2. Finally, I show the benchmark simulations and verifications of the forward model in section 2.3.

The radiation fields—radiance and the state of polarization—measured by the AERONET SunPhotometer are the outcome of solar radiation interacting with various physical processes including the absorption and scattering by atmospheric molecules, aerosols and clouds, as well the reflection and absorption by underlying surface. The radiance and polarization of light at any wavelength can be represented by a Stokes column vector \mathbf{I} having four elements [*Hansen and Travis, 1974*]:

$$\mathbf{I} = [I, Q, U, V]^T, \quad (2.1)$$

where I is the total intensity (or radiance), Q and U describe the state of linear polarization, V describes the state of circular polarization, and T indicates a transposed matrix. It should be noted that all radiation fields and optical parameters used in this paper are functions of the light wavelength λ . For simplicity, however, we omit λ in all formulas. The degree of linear polarization (DOLP) is defined by

$$\text{DOLP} = \frac{\sqrt{Q^2 + U^2}}{I}. \quad (2.2)$$

In the solar principal plane, U is negligibly small and the above formula becomes $\text{DOLP} = -Q/I$. Let $\mathbf{I}_0 = [I_0, 0, 0, 0]^T$ denote the Stokes vector for incident Solar radiation at the top of the atmosphere (TOA) from the direction (θ_0, ϕ_0) , where θ_0 and ϕ_0 are the incident solar zenith and azimuth angles, respectively. For a plane-parallel atmosphere bounded below by a reflective surface, the vector radiative transfer equation in the medium for the specific intensity column vector \mathbf{I} of light propagating in the viewing direction (θ, ϕ) can be written [[Hovenier et al., 2004](#); [Mishchenko et al., 2002](#)]:

$$\mu \frac{\partial \mathbf{I}(\tau, \mu, \phi)}{\partial \tau} = \mathbf{I}(\tau, \mu, \phi) - \mathbf{J}(\tau, \mu, \phi; \mu_0, \phi_0) \quad (2.3)$$

$$\begin{aligned} \mathbf{J}(\tau, \mu, \phi; \mu_0, \phi_0) &= \frac{\omega}{4\pi} \int_{-1}^1 \int_0^{2\pi} \mathbf{P}(\tau, \mu, \mu_0, \phi - \phi_0) \mathbf{I}(\tau, \mu_0, \phi_0) d\phi_0 d\mu_0 \\ &\quad + \frac{\omega}{4\pi} \mathbf{P}(\tau, \mu, \mu_0, \phi - \phi_0) \mathbf{I}_0 \exp(-\tau/\mu_0) \end{aligned} \quad (2.4)$$

Here, τ is the extinction optical depth measured from TOA, μ and μ_0 are cosines of θ and θ_0 , respectively, ω is the SSA and \mathbf{P} is the phase matrix. The first term in equation (2.3) represents multiple scattering contributions, while the second indicates scattered light from the direct solar beam.

Parameters required to solve the above radiative transfer equation are τ , ω , and $\mathbf{P}(\Theta)$ for the atmosphere, and the reflectance matrix $\mathbf{R}_s(\tau, \mu, \phi; \mu_0, \phi_0)$ of the underlying surface.

Considering a cloud-free atmosphere, the solar radiation is attenuated by molecular scattering, gaseous absorption, and aerosol scattering and absorption. For a given layer, we have

$$\tau = \tau_A + \tau_R + \tau_G \quad (2.5)$$

$$\omega = \frac{\tau_A \omega_A + \tau_R}{\tau} \quad (2.6)$$

$$\mathbf{P}(\Theta) = \mathbf{P}_A(\Theta) \frac{\tau_A \omega_A}{\tau_A \omega_A + \tau_R} + \mathbf{P}_R(\Theta) \frac{\tau_R}{\tau_A \omega_A + \tau_R} \quad (2.7)$$

where τ_A , τ_R , and τ_G are optical depth, respectively, by aerosol extinction, Rayleigh scattering of air density fluctuations, and gaseous absorption. ω_A is the SSA of aerosol, and $\mathbf{P}_A(\Theta)$ and $\mathbf{P}_R(\Theta)$ are, respectively, the aerosol and Rayleigh phase matrices as functions of the scattering angle Θ . Therefore, the forward modeling development thus requires the computation of single scattering properties for aerosols and air density fluctuations, rigorous treatment for absorption of trace gases, accurate representation of reflectance/polarization by surface, and the realistic simulation of polarimetric radiative transfer.

2.2 The UNL-VRTM

We have developed the UNified Linearized Vector Radiative Transfer Model, or UNL-VRTM, specifically for simulation, analysis, and inversion of the photo-polarimetric measurements. As shown in Figure 2.1, the UNL-VRTM comprises 6 modules; they are

1. A module computing Rayleigh scattering (section 2.2.1);
2. A module that deal with gaseous absorption (section 2.2.1);
3. A linearized Mie scattering code (section 2.2.2);
4. A linearized T-matrix electromagnetic scattering code (section 2.2.2);

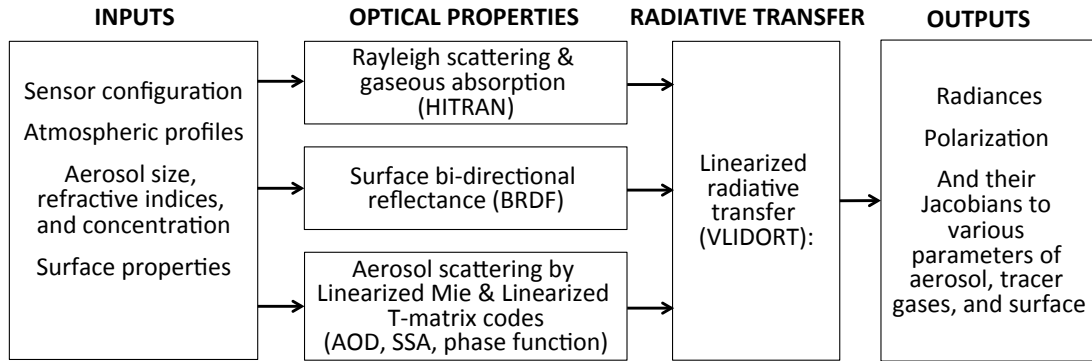


Figure 2.1: Flowchart of the UNL-VRTM components. See text for detail.

5. A surface model computing various bidirectional reflectance/polarization functions (BRDF/BPDF) (section 2.2.3);
6. A vector linearized radiative transfer model—VLIDORT (section 2.2.4).

These modules are integrated for the forward calculation of aerosol single scattering, gas absorption, and vector radiative transfer hereafter, and thus they together constitute the UNified Linearized Radiative Transfer Model, UNL-VRTM.

Inputs for the UNL-VRTM are profiles of atmospheric properties and constituents (temperature, pressure, aerosol mass concentration or layer AOD, water vapor amount and other trace gas volume mixing ratio profiles [[McClatchey et al., 1972](#)]), the surface properties, as well as the aerosol parameters (such as PSD parameters and refractive index) themselves. Bearing in mind the lack of sensitivity in passive remote sensing for the retrieval of vertical profiles of aerosol properties, the UNL-VRTM as it stands now is only designed to deliver radiative calculations for a maximum of two sets of aerosol single scattering properties (e.g., aerosol PSD, refractive index, and particle shape), typically with one fine-mode and one coarse-mode aerosol. Other inputs for model include spectral and geometrical definitions that characterizing specification of an observing sensor.

Outputs of the model include the Stokes vector (\mathbf{I}) at user-defined spectral wavelengths and desired atmospheric levels for both upwelling and downwelling radiation, from which the light radiance and degree of polarization can be derived. Outputs also include analytical Jacobians of \mathbf{I} with respect to all aerosol particle parameters (PSD, refractive index, vertical profile), Rayleigh scattering optical depth, optical depth of all trace gases, and parameters describing surface optical property. A detail description of the UNL-VRTM's Jacobian capability is presented in section 2.2.5.

Although the UNL-VRTM is used to simulate the AERONET measurements in this work, the module-based structure of UNL-VRTM allows its application not limit to the AERONET inversion. It can be easily used to simulate observations from other remote sensing platforms, like satellite sensors. For example, we have employed it to explore the aerosol information content of observations from the future TEMPO/GEO-CAPE geostationary satellite sensors [Wang *et al.*, 2014], to investigate the potential application of hyper-spectral radiances at O₂A and O₂B bands for the retrieval of aerosol vertical profile [Wang *et al.*, 2014; Ding *et al.*, 2014], to retrieve aerosol microphysical properties from GeoTASO measured UV-to-visible continuous radiance spectra [Hou *et al.*, 2014], and to perform AOD retrieval from GOSAT/TANSO-CAI's UV radiance [Han *et al.*, 2014].

Recently, we have made the UNL-VRTM publicly accessible. We published the source code on <http://meteo.unl.edu/~xxu/unlvrtm.php>. A detail description and a dedicated User's Guide for the model is also available on the webpage.

2.2.1 Molecular scattering and absorption

The Rayleigh scattering optical depth at certain wavelength in any atmospheric layer (τ_R) is computed by

$$\tau_R = N_{\text{air}} \sigma_R \quad (2.8)$$

where N_{air} is air molecular number density of that layer (molec cm^{-2}), and σ_R is the Rayleigh scattering cross-section ($\text{cm}^2 \text{ molec}^{-1}$) computed following [Bodhaine et al. \[1999\]](#). The Rayleigh phase matrix, $\mathbf{P}_R(\Theta)$, depends upon molecular anisotropy through the depolarization factor, also computed from the same source. [Bodhaine et al. \[1999\]](#) computes the wavelength-dependent Rayleigh scattering cross-section as a function of mixing ratios for N_2 , O_2 , H_2O , and CO_2 . The phase matrix for Rayleigh scattering follows [Hansen and Travis \[1974\]](#); we use the set of spherical-function expansion coefficients for the phase matrix as supplied for VLIDORT [[Spurr, 2006](#)].

Calculation of the absorption optical depth (τ_G) at any atmospheric layer for K different trace gases follows

$$\tau_G = \sum_{i=1}^K N_{\text{gas},i} \sigma_{A,i}(T, P) \quad (2.9)$$

where $N_{\text{gas},i}$ is the number density of i th gas within that layer, and $\sigma_{A,i}$ is the corresponding absorption cross-section, a function of temperature and pressure. Our model accounts for absorptions by a total number of 22 trace gases: H_2O , CO_2 , O_3 , N_2O , CO , CH_4 , O_2 , NO , SO_2 , NO_2 , NH_3 , HNO_3 , OH , HF , KCl , HBr , HI , ClO , OCS , H_2CO , HOCl , and N_2 . The determination of σ_A utilizes a UV-to-visible cross-section library and the line-spectroscopic absorption parameters archived in the HITRAN database [[Orphal and Chance, 2003](#); [Rothman et al., 2009](#)]. The cross-section library compiles the extinction cross-section for O_3 , NO_2 , SO_2 , and O_2-O_2 in the UV and/or visible spectral regions. Meanwhile, line-spectroscopic absorption databased are used to simulate the pressure- and temperature-dependent extinction cross-section with line-by-line (LBL) approach [[Liou, 2002](#); [Rothman et al., 2009](#)] by accumulating each individual absorption line. Doppler broadening is calculated from the molecular mass and the temperature, and Doppler and Lorentz broadening are included in the Voigt calculation.

Particular to work, we only consider the most influential trace species for the AERONET

spectral bands: H₂O (vapor), O₃, and NO₂. In our algorithm (section 3), the columnar amounts of O₃ and NO₂ are dynamically adjusted with retrievals from the Ozone Monitoring Instrument (OMI) [Leveld *et al.*, 2006] on board the AURA satellite. We apply the columnar water vapor amount retrieved from the 940-nm radiances measured by the AERONET SunPhotometer *Halthore et al.* [1997].

2.2.2 Aerosol single scattering

Aerosol single scattering properties necessary to the radiative transfer calculation include aerosol optical depth (τ_A) (Q_{ext}), SSA (ω_A), and scattering phase matrix ($\mathbf{P}_A(\Theta)$). The calculation of these parameters is made with a Linearized Mie (LMIE) scattering electromagnetic code for spherical particles and a Linearized T-matrix (LTMATRIX) scattering code for non-spherical convex and axially symmetric particles [Spurr *et al.*, 2012]. The LMIE code originates from the Mie code of *de Rooij and Stap* [1984], and the LTMATRIX code originates from the T-Matrix code developed by *Mishchenko et al.* [1996]; *Mishchenko and Travis* [1998]; both include linearization capability developed by Spurr *et al.* [2012].

Common inputs for both codes are the complex refractive index ($m_r + im_i$), and the particle size distribution (PSD) parameters for polydisperse scattering. The codes have several options to specify the PSD function: two-parameter gamma, two-parameter lognormal, three-parameter modified gamma, and four-parameter bi-lognormal. In addition, the linearized T-matrix code offers options to characterize the shape of non-spherical aerosols (spheroids, cylinders, or Chebyshev particles) [Spurr *et al.*, 2012]. For non-spherical particles, the specified size distribution is interpreted as the equivalent surface-area sphere in the linearized T-matrix calculation, regardless of the shape.

For AERONET inversion algorithm, we assume that the aerosol volume distribution follows a bi-modal lognormal function [in agreement with *Schuster et al.*, 2006; *Waquet et al.*,

2009]:

$$\frac{dV}{d\ln r} = \sum_{i=1}^2 \frac{V_0^i}{\sqrt{2\pi} \ln \sigma_g^i} \exp \left[-\frac{(\ln r - \ln r_v^i)^2}{2 \ln^2 \sigma_g^i} \right] \quad (2.10)$$

where V_0 , r_v , and σ_g are the total volume concentration, geometric median radius, and standard deviation, respectively. The superscript i indicates the size mode, and later will be replaced by ‘f’ for fine mode and ‘c’ for coarse mode. We assume that particle size ranges from 0.01 to 10 μm for the fine mode and from 0.05 to 20 μm for the coarse mode, both covering $> 99.9\%$ of the total volume of an idealistic size range $(0, +\infty)$. An advantage of the lognormal distribution is that standard deviations for the number, area, and volume PSD functions are identical, and therefore allowing that the median radii for these PSD functions can be converted from one to another [Seinfeld and Pandis, 2006]. The r_{eff} and v_{eff} are related to the geometric parameters through:

$$r_{\text{eff}} = r_v \exp \left(-\frac{1}{2} \ln^2 \sigma_g \right), \quad (2.11)$$

$$v_{\text{eff}} = \exp (\ln^2 \sigma_g) - 1. \quad (2.12)$$

The LMIE/LTMATRIX code computes the aerosol extinction efficiency factor Q_{ext} , single scattering albedo ω_A , and phase matrix $\mathbf{P}_A(\Theta)$, as well as Jacobians of these quantities with respect to input parameters including r_{eff} , v_{eff} , m_r , and m_i . The phase matrix and its Jacobians are expressed in terms of the coefficients $\mathbf{B}_A(\Theta)$ for each moment l in terms of the generalized spherical function expansions for each non-zero phase matrix element. Let $\boldsymbol{\Lambda}$ denotes the vector of aerosol microphysical parameters, $\boldsymbol{\Lambda} = [V_0, r_{\text{eff}}, v_{\text{eff}}, m_r, m_i]^T$, and \mathbf{M} the vector of aerosol optical parameters, $\mathbf{M} = [\tau_A, \omega_A, \mathbf{B}_A(\Theta)]^T$, where τ_A is related to Q_{ext} by $\tau_A = \frac{3V_0 Q_{\text{ext}}}{4r_{\text{eff}}}$. The LMIE/LTMATRIX code acts as an operator that maps vector $\boldsymbol{\Lambda}$ to \mathbf{M} . The Jacobian matrix of \mathbf{M} with respect to $\boldsymbol{\Lambda}$, or $\frac{\partial \mathbf{M}}{\partial \boldsymbol{\Lambda}}$, is calculated by means of the linearization feature of the code.

2.2.3 Surface representations

VLIDORT has a supplementary module for specification of the surface BRDF as a linear combination of (up to) three semi-empirical kernel functions; for details, see [Spurr \[2004\]](#). This supplementary module can also provide partial derivatives of the BRDF with respect to the kernel weighting factors or with respect to kernel parameters such as the wind speed for glitter reflectance. These kernel functions include Lambertian, Ross-Thick, and Li-Sparse functions [[Wanner et al., 1995](#); [Lucht et al., 2000](#)], a Bi-directional Polarization Distribution Function (BPDF) [[Maignan et al., 2009](#)], and an ocean surface model based on the Cox-Munk model [[Cox and Munk, 1954](#)]. In addition, VLIDORT has an option for using a surface-leaving radiation field, either as a fluorescence term or as a water-leaving term expressed as a function of chlorophyll absorption.

Although surface reflectance has in general a low influence on AERONET down-welling sky radiances and polarization, a state-of-the-art representation of the surface reflectivity potentially reduces model uncertainties, especially for measurements taken at low elevation angles that could be affected by surface diffusion. Here, we utilize the spectral BRDF parameters from the MODIS surface products that are operationally reported every 16 days at a 1-km resolution [[Lucht et al., 2000](#)]. Here we use time-matched MODIS BRDF products to reconstruct the bidirectional reflectance over AERONET stations. The MODIS BRDF product supplies three weighting parameters (f_{iso} , f_{vol} , and f_{geo}) for the first 7 MODIS bands, respectively, corresponding to three kernel types: isotropic, Ross-Thick (K_{vol}), and Li-Sparse (K_{geo}):

$$\rho_R(\mu, \phi; \mu_0, \phi_0) = f_{\text{iso}} + f_{\text{vol}}K_{\text{vol}}(\mu, \phi; \mu_0, \phi_0) + f_{\text{geo}}K_{\text{geo}}(\mu, \phi; \mu_0, \phi_0) \quad (2.13)$$

Expanded expressions for K_{vol} and K_{geo} appear in [Wanner et al. \[1995\]](#); [Lucht et al. \[2000\]](#).

Studies have shown that the BPDF for land surfaces is generally rather small and is “spectrally neutral” [Nadal and Breon, 1999; Maignan et al., 2004, 2009; Waquet et al., 2007; Litvinov et al., 2011]. Most empirical BPDF models are based on Fresnel coefficients of light reflectance from the surface. Here we have incorporated the one-parameter model developed by Maignan et al. [2009], which was derived from analyses of several years of POLDER/PARASOL measurements. This model describes the polarized reflectance at any viewing geometry (μ, ϕ) from the given incident geometry (μ_0, ϕ_0) as:

$$\rho_P(\mu, \phi; \mu_0, \phi_0) = \frac{C_0 \exp(-\tan \theta_h) \exp(-\text{NDVI})}{\mu_0 + \mu} \mathbf{F}_P(\theta_h, n_v) \quad (2.14)$$

where C_0 is a constant parameter chosen for a certain surface type, θ_h is half of the phase angle of reflectance, n_v is the refractive index of vegetation (1.5 is used), and \mathbf{F}_P is the Fresnel reflection matrix. We chose a spectrally-independent value for C_0 based on the recommendations by Maignan et al. [2009] for relevant surface types.

The combination of the BRDF and BPDF for land surface follows the discussion by Dubovik et al. [2011]. The surface reflectance matrix $\mathbf{R}_s(\mu, \phi; \mu_0, \phi_0)$ is represented as a sum of diffuse unpolarized reflectance and specular reflectance; the former is modeled using the MODIS BRDF in equation (2.13), and the latter using the BPDF formula in equation (2.14).

2.2.4 Radiative transfer

The radiative transfer equation (2.3) is solved with the Vector Linearized Discrete Ordinate Radiative Transfer (VLIDORT) model, which is a core part of the UNL-VRTM. VLIDORT, developed by Spurr [2006], is a linearized pseudo-spherical vector discrete ordinate radiative transfer model for multiple scattering of diffuse radiation in a stratified multi-layer atmosphere. It computes four elements of the Stokes vector I for downwelling and upwelling

radiation at any desired atmospheric level. The VLIDORT includes the pseudo-spherical approximation to calculate solar beam attenuation in a curved medium. It also uses the delta-M approximation for dealing with sharply peaked forward scattering. Specifically for the AERONET inversion, we consider 16 discrete ordinate streams in the radiative transfer calculation and retain 180 terms in the spherical-function expansion of the scattering matrix to ensure accurate calculation of diffuse radiation.

Along with the Stokes vector \mathbf{I} , VLIDORT also computes the Jacobian matrix of \mathbf{I} with respect to aerosol optical vector \mathbf{M} , $\frac{\partial \mathbf{I}}{\partial \mathbf{M}}$. Therefore, the combination of the VLIDORT and the LMIE/LTMATRIX codes allows for a direct calculation of the Jacobian matrix of the Stokes vector with respect to aerosol microphysics $\mathbf{\Lambda}$ by

$$\frac{\partial \mathbf{I}}{\partial \mathbf{\Lambda}} = \frac{\partial \mathbf{I}}{\partial \mathbf{M}} \cdot \frac{\partial \mathbf{M}}{\partial \mathbf{\Lambda}} \quad (2.15)$$

Essentially, the above equation can yield the derivatives of the radiance I and DOLP with respect to any aerosol microphysical parameter, i.e., $\frac{\partial I}{\partial \mathbf{\Lambda}}$ and $\frac{\partial \text{DOLP}}{\partial \mathbf{\Lambda}}$. While obtaining $\frac{\partial I}{\partial \mathbf{\Lambda}}$ is straightforward, $\frac{\partial \text{DOLP}}{\partial \mathbf{\Lambda}}$ can be derived from equation (2.2) following:

$$\frac{\partial \text{DOLP}}{\partial \mathbf{\Lambda}} = -\frac{\text{DOLP}}{I} \frac{\partial I}{\partial \mathbf{\Lambda}} + \frac{Q \frac{\partial Q}{\partial \mathbf{\Lambda}} + U \frac{\partial U}{\partial \mathbf{\Lambda}}}{I \sqrt{Q^2 + U^2}} \quad (2.16)$$

2.2.5 Capability of calculating Jacobians

This section analytically derives the Jacobian of \mathbf{I} with respect to various aerosol related parameters, including τ_A , ω_A , \mathbf{B}_A , refractive index, PSD parameters, and aerosol vertical profile. Computation of the Stokes vector in VLIDORT requires input of an optical property set $[\tau, \omega, \langle \mathbf{B}^j \rangle_{j=0,J}]$ for each atmospheric layer, where $\langle \rangle_{j=0,J}$ denotes the vector that consists of elements having the similar expression as that inside $\langle \rangle$ but for $j = 0, J$. For

each atmospheric layer L , the optical property inputs are assumed constant and are given by equations (2.5)–(2.6), as well as equation (2.7) with $\mathbf{P}(\Theta)$ replaced by \mathbf{B}^j . It should be noted that all parameters in these equations are for each layer, but we ignore L for convenience.

Since VLIDORT generates Jacobians with respect to layer-integrated single scattering properties in each atmospheric layer as well as column-integrated single scattering property as a whole, and LMIE and LTMATRIX offer the sensitivity of aerosol scattering properties to microphysical aerosol physical parameters, an integrated use of VLIDORT and LTATRIX/LMIE can, in principle, provide the Jacobians of Stokes parameters with respect to both aerosol single scattering properties as well as aerosol microphysical parameters (as expressed by equations (2.15)–(2.16)). Practically, the VLIDORT calculation of Jacobians of any Stokes parameter ξ with respect to any aerosol parameter x proceeds according to

$$\begin{aligned} x \frac{\partial \xi}{\partial x} &= x \left[\frac{\partial \xi}{\partial \tau}, \frac{\partial \xi}{\partial \omega}, \left\langle \frac{\partial \xi}{\partial \mathbf{B}^j} \right\rangle_{j=1,J} \right] \left[\frac{\partial \tau}{\partial x}, \frac{\partial \omega}{\partial x}, \left\langle \frac{\partial \mathbf{B}^j}{\partial x} \right\rangle_{j=1,J} \right]^T \\ &= \left[\tau \frac{\partial \xi}{\partial \tau}, \omega \frac{\partial \xi}{\partial \omega}, \left\langle \mathbf{B}^j \frac{\partial \xi}{\partial \mathbf{B}^j} \right\rangle_{j=1,J} \right] \left[\phi_x, \varphi_x, \langle \Psi_x^j \rangle_{j=1,J} \right]^T. \end{aligned} \quad (2.17)$$

The first square bracket on the right-hand side of equation (2.17) contains quantities computed internally by VLIDORT, while the second so-called “transformation vector” must be supplied by users and is defined as:

$$\phi_x = \frac{x \partial \tau}{\tau \partial x}; \quad \varphi_x = \frac{x \partial \omega}{\omega \partial x}; \quad \Psi_x^j = \frac{x}{\mathbf{B}^j} \frac{\partial \mathbf{B}^j}{\partial x}. \quad (2.18)$$

As we are interested in aerosol parameters, this transformation vector can be further expanded as

$$\left[\phi_x, \varphi_x, \langle \Psi_x^j \rangle_{j=1,J} \right]^T = \boldsymbol{\Pi} \left[\phi'_x, \varphi'_x, \langle \Psi'^j_x \rangle_{j=1,J} \right]^T, \quad (2.19)$$

Table 2.1: Elements of transformation vector for various aerosol single scattering parameters (composite of fine and coarse mode).

| x | ϕ_x | φ_x | Ψ_x^j |
|------------|-----------------------|--|---|
| τ_A | $\frac{\tau_A}{\tau}$ | $\frac{\tau_A}{\tau} \left(\frac{\omega_A}{\omega} - 1 \right)$ | $\begin{cases} \frac{\omega_A \tau_A}{\omega \tau} \left(\frac{\mathbf{B}_A^j}{\mathbf{B}^j} - 1 \right) & \text{for } j < 3 \\ \frac{\tau_R}{\omega \tau} & \text{for } j \geq 3 \end{cases}$ |
| ω_A | 0 | $\frac{\tau_A \omega_A}{\tau \tau_A \omega_A + \tau_R}$ | Same as above |
| B_A^j | 0 | 0 | $\begin{cases} \frac{\omega_A \tau_A \mathbf{B}_A^j}{\omega_A \tau_A \mathbf{B}_A^j + \tau_R \mathbf{B}_R^j} & \text{for } m = j < 3 \\ 1 & \text{for } m = j \geq 3 \\ 0 & \text{for } m \neq j \end{cases}$ |

where

$$\phi'_x = x \frac{\partial \tau_A}{\partial x}, \quad \varphi'_x = x \frac{\partial \delta_A}{\partial x}, \quad \text{and} \quad \Psi'_x^j = x \frac{\partial \mathbf{B}_A^j}{\partial x}, \quad (2.20)$$

and Π is a matrix expressed by

$$\Pi = \begin{bmatrix} \frac{1}{\tau} & \mathbf{0} & \mathbf{0} \\ -\frac{1}{\tau} & \frac{1}{\delta_A + \tau_R} & \mathbf{0} \\ \mathbf{0} & \left\langle \frac{\mathbf{B}_A^j - \mathbf{B}_R^j}{\mathbf{B}^j (\delta_A + \tau_R)} \right\rangle_{j=1,J} & \left\langle \frac{\delta_A}{\mathbf{B}^j (\delta_A + \tau_R)} \right\rangle_{j=1,J} \end{bmatrix}. \quad (2.21)$$

Here, δ_A is the scattering optical depth of aerosols. The detailed derivations of the matrix Π are presented in Appendix A. Hence, the transformation vector for calculating Stokes profile Jacobians with respect to τ_A , ω_A , \mathbf{B}_A^j can be obtained by combining equations (2.19) and (2.21), and the components of this vector are listed in Table 2.1.

In an atmosphere where both fine (superscript “f”) and coarse (superscript “c”) aerosol particles co-exist, the ensemble aerosol optical properties may be derived by assuming external mixing:

$$\begin{cases} \tau_A = \tau_A^f + \tau_A^c \\ \delta_A = \delta_A^f + \delta_A^c \\ \mathbf{B}_A^j = \frac{\delta_A^f + \delta_A^c}{\delta_A^f \mathbf{B}_A^{f,j} + \delta_A^c \mathbf{B}_A^{c,j}} \end{cases} \quad (2.22)$$

Table 2.2: Elements of transformation vector for various microphysical parameters of fine and coarse mode aerosols^a.

| x | ϕ'_{x^f} | φ'_{x^f} | $\Psi'^j_{x^f}$ |
|------------------------------------|---|---|---|
| τ_A^f | τ_A^f | δ_A^f | $\frac{\delta_A^f}{\tau_A} (\mathbf{B}_A^{fj} - \mathbf{B}_A^j)$ |
| ω_A | 0 | δ_A^f | $\frac{\delta_A^f}{\tau_A} (\mathbf{B}_A^{fj} - \mathbf{B}_A^j)$ |
| V_0^f | $\frac{3V_0^f Q_{ext}^f}{4r_{eff}^f}$ | $\frac{3V_0^f Q_{sca}^f}{4r_{eff}^f}$ | $\frac{\delta_A^f}{\tau_A} (\mathbf{B}_A^{fj} - \mathbf{B}_A^j)$ |
| m_r^f, m_i^f | $\tau_A^f \frac{x^f}{Q_{ext}^f} \frac{\partial Q_{ext}^f}{\partial x^f}$ | $\delta_A^f \frac{x^f}{Q_{sca}^f} \frac{\partial Q_{sca}^f}{\partial x^f}$ | $\frac{\phi'_{x^f}}{\delta_A^f} (\mathbf{B}_A^{fj} - \mathbf{B}_A^j) + x^f \frac{\partial \mathbf{B}_A^{fj}}{\partial x^f}$ |
| $r_g^f, \sigma_g^f, \varepsilon^f$ | $\tau_A^f \left(\frac{x^f}{Q_{ext}^f} \frac{\partial Q_{ext}^f}{\partial x^f} - \frac{x^f}{r_{eff}^f} \frac{\partial r_{eff}^f}{\partial x^f} \right)$ | $\delta_A^f \left(\frac{x^f}{Q_{sca}^f} \frac{\partial Q_{sca}^f}{\partial x^f} - \frac{x^f}{r_{eff}^f} \frac{\partial r_{eff}^f}{\partial x^f} \right)$ | $\frac{\phi'_{x^f}}{\delta_A^f} (\mathbf{B}_A^{fj} - \mathbf{B}_A^j) + x^f \frac{\partial \mathbf{B}_A^{fj}}{\partial x^f}$ |
| H^f | $H^f \frac{\partial \tau_A^f}{\partial H^f}$ | $\phi'_{x^f} \omega_A^f$ | $\frac{\delta_A^f}{\tau_A} (\mathbf{B}_A^{fj} - \mathbf{B}_A^j)$ |

^a Expressions are shown only for fine-mode parameters; expressions for coarse-mode parameters are the same but with superscripts replaced by 'c'

We can generate the transformation vectors (as listed in Table 2.2) for any of the following parameters: τ_A^f , ω_A^f , V_0^f , m_r^f , m_i^f , r_g^f , σ_g^f , ε^f , H^f , and τ_A^c , ω_A^c , V_0^c , m_r^c , m_i^c , r_g^c , σ_g^c , ε^c , and H^c . Here, r_g , σ_g , and H denote the median and standard deviation of the particle radius (e.g., two parameters in the log-normal aerosol number distribution), and the scale height of aerosol extinction, respectively. V_0 is the aerosol volume concentration and ε the shape factor of the non-spherical particle. Details of the algebra for deriving the transformation vectors may be found in Appendix A. Note that the shape of the aerosol extinction vertical profile in the testbed is assumed to be constant or exponentially decreasing with height or quasi-Gaussian (Appendix A). The analytical formulas for ϕ'_x , φ'_x , and Ψ'^j_x for coarse mode aerosol parameters are the same as their counterparts for fine-mode aerosols; we need only replace superscript "s" with "c" in Table 3 entries. Jacobians with respect to the fine mode fraction, either in terms of AOD (fmf_τ) or in terms of the volume concentration (fmf_v), can be derived from the corresponding Jacobians with respect to modal AOD and volume,

respectively:

$$\text{fmf}_\tau \frac{\partial \xi}{\partial \text{fmf}_\tau} = \tau_A^f \frac{\partial \xi}{\partial \tau_A^f} - \frac{\text{fmf}_\tau}{1 - \text{fmf}_\tau} \tau_A^c \frac{\partial \xi}{\partial \tau_A^c} \quad (2.23)$$

$$\text{fmf}_v \frac{\partial \xi}{\partial \text{fmf}_v} = V_0^f \frac{\partial \xi}{\partial V_0^f} - \frac{\text{fmf}_v}{1 - \text{fmf}_v} V_0^c \frac{\partial \xi}{\partial V_0^c} \quad (2.24)$$

Details of these necessary VLIDORT inputs are presented in Appendix A, and a comprehensive verification of these Jacobian calculation are presented in following section 2.3.

2.3 Model Benchmarking and Verifications

Figure 2.2a shows the downward solar spectral irradiance at the top-of-atmosphere and at the surface for a solar zenith angle of 30°. Spectral regions dominated by gas absorption can be clearly identified, including the O₃ Hartley-Huggins bands in the UV, the O₂B band (0.69 μm) and O₂A band (0.76 μm), as well as a number of water vapor bands. The spectroscopic calculations shown in Figure 2.2 were performed at a resolution of 0.01 nm. In general this resolution is high enough to pick up fine structure in gas absorptions. In the UV below 300 nm, and in parts of the O₂A and O₂B bands, whole-atmosphere gas absorption optical depths can reach 50 or more, and the downward irradiance is nearly zero at the ground (Figure 2.2b). The inset in Figure 2.2b shows a close-up view of the fine structure in absorption optical depth for the O₂A band, with dual peaks centered at 0.761 μm and 0.764 μm, and a deep, narrow valley around 0.762 μm. Similarly, the continuum of water vapor absorption from the near-infrared to about 4 μm is also well simulated (Figure 2.2c). Also of note is the non-negligible absorption of SO₂ and NO₂ in UV and blue wavelength regions respectively (Figure 2.2d). In urban regions, high SO₂ and NO₂ can together contribute optical depths of around 0.03–0.07 (Figure 2.2d). Hence, in order to take

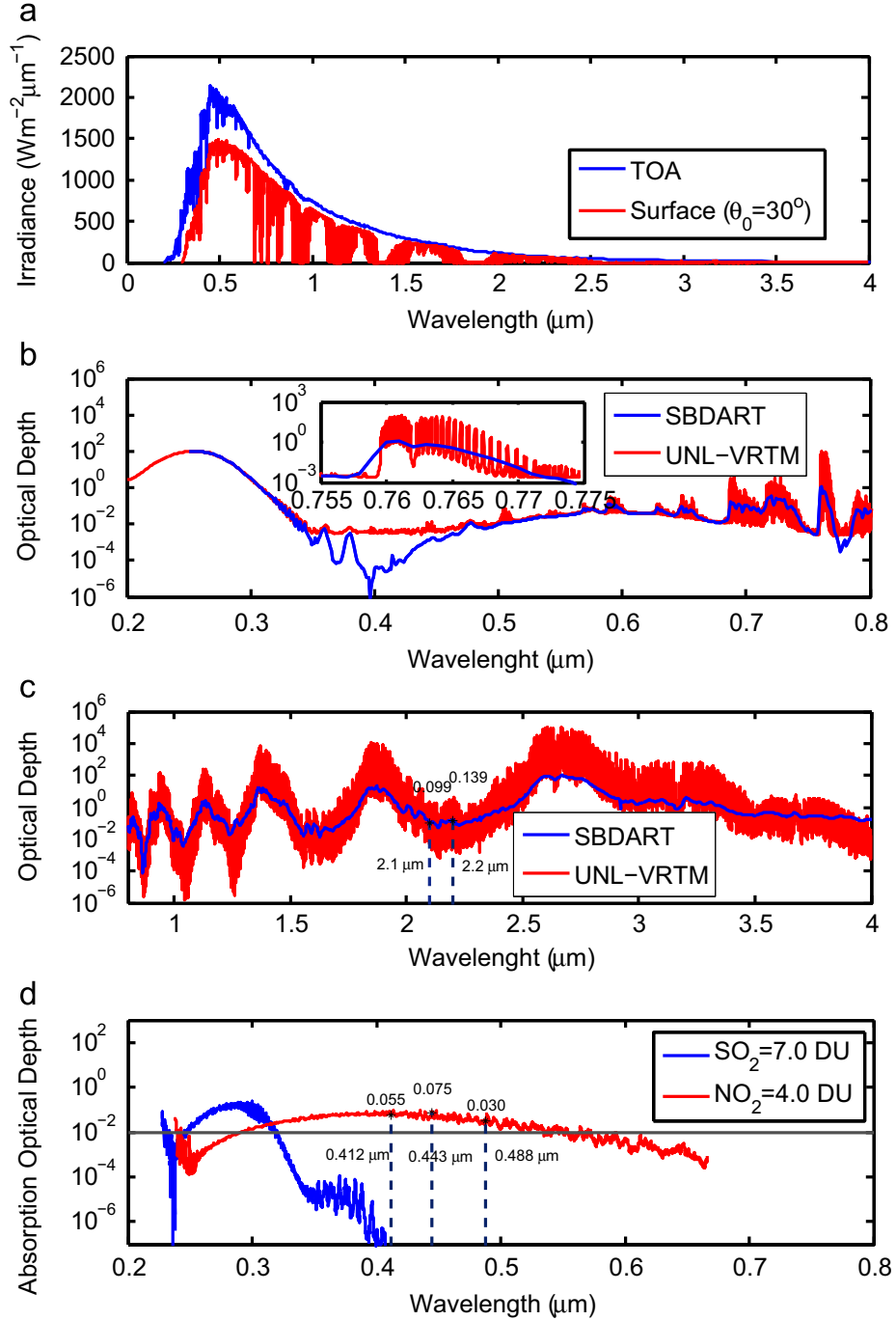


Figure 2.2: Some benchmark simulations by the UNL-VRTM: (a) Downward solar spectral irradiance at the TOA and the surface for solar zenith angle of 30° . (b) Total-atmosphere gas absorption optical depth in the range 0.2 – $0.8 \mu\text{m}$. (c) Same as (b) but for 0.8 – $4 \mu\text{m}$. (d) Optical depth of SO_2 and NO_2 in polluted cases. Also shown in (b) and (c) are the optical depth computed from Santa Barbara DISORT Atmospheric Radiative Transfer (SBDART) model [Ricchiazzi *et al.*, 1998]. The mid-latitude summer atmospheric profile is assumed [McClatchey *et al.*, 1972]. (Figure adopted from Wang *et al.* [2014].)

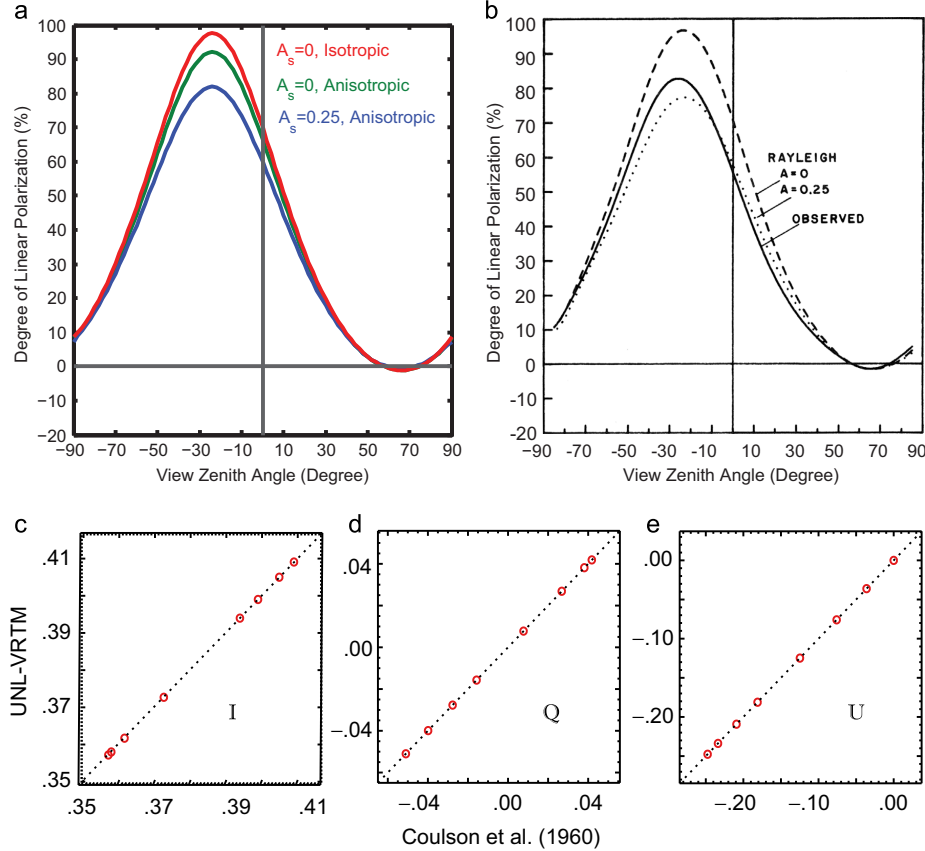


Figure 2.3: Degree of linear polarization ($-Q/I$) of downward radiation for a pure Rayleigh atmosphere: (a) computed by UNL-VRTM for the case analyzed in Figure 5.7 of [Coulson \[1988\]](#) and shown here as (b). (c)–(e) shows the comparisons of I , Q , and U computed by [Coulson et al. \[1960\]](#) and those from UNL-VRTM. In (a) and (b), A_s represents the surface albedo value. In (c) and (d), the calculation is for $\tau = 1.0$, surface albedo is 0.25, $\cos \theta_0 = 0.8$, and for 8 different viewing angles. (Figure adopted from [Wang et al. \[2014\]](#).)

advantage of low surface reflectance in the UV and the use of deep-blue wavelengths for the retrieval of AOD in urban regions, it is critical to treat absorption by SO_2 and NO_2 . In contrast, calculations performed at moderate spectral resolution (such as those from Santa Barbara Discrete-Ordinate Atmospheric Radiative Transfer, or SBDART [[Ricchiazzi et al., 1998](#)], shown as the blue lines in Figure 2.2b and c) do not resolve fine-structure details, sometimes missing the absorption lines for SO_2 or NO_2 , and in general producing significant underestimation of optical depths in the O_2A band.

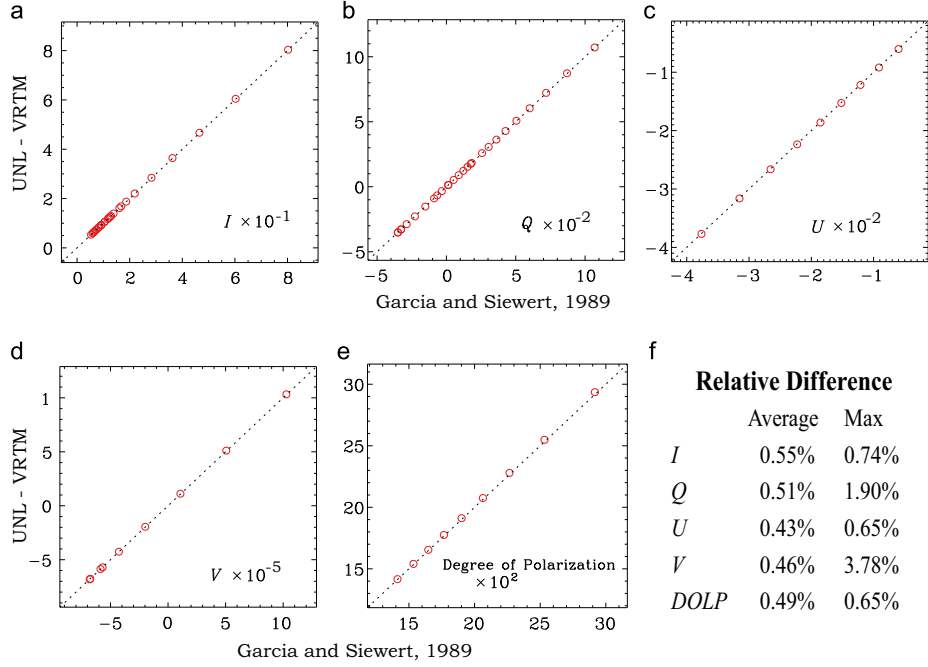


Figure 2.4: Counterparts in Tables 3–10 of [Garcia and Siewert \[1989\]](#) for upwelling radiation on the top of the same atmospheric conditions of aerosol scattering. No gas absorption and Rayleigh scattering are considered. Note that compared here are I and Q values reported in [Garcia and Siewert \[1989\]](#) for 9 view angles (with cosine values from 0.1 to 0.9 at equal spacing of 0.1) and 3 relative azimuth angles ($0, \pi/2$, and π), which yields a total of 27 data points. For U and V , their values are reported for the same 9 viewing angles but for one relative azimuth angle ($\pi/2$) only. The calculation is performed at wavelength of 951 nm and τ of 1.0, and aerosol size distribution parameters $r_{\text{eff}} = 0.2$, $v_{\text{eff}} = 0.07$, refractive index $m_r = 1.44$, and SSA of 0.99. (Figure adopted from [Wang et al. \[2014\]](#).)

Figure 2.3 shows the calculation of the degree of linear polarization (DOLP) of downward radiation in a pure Rayleigh scattering atmosphere. The solid blue line in Figure 2.3a (dotted line in Figure 2.3b) reproduces the theoretical results shown in Figure 5.7 of [Coulson \[1988\]](#), which was used to interpret the DOLP measured at Mauna Loa Observatory on February 19, 1977. Furthermore, Figure 2.3a shows that the anisotropy in Rayleigh scattering reduces the peak DOLP by 5% (e.g., the difference between the green and red lines) at $0.7 \mu\text{m}$. Surface reflection and its concomitant increase of atmosphere scattering will decrease the DOLP of downward radiation. An increase of surface reflectance from 0 to 0.25 decreases the peak

DOLP by 10%.

Quantitatively, the Stokes-vector I , Q , and U components computed with UNL-VRTM differ from their counterparts found in the tables by [Coulson et al. \[1960\]](#) by average (relative) deviations of 1.9×10^{-4} (0.05%), 2×10^{-5} (0.14%), and 4×10^{-5} (0.03%), respectively (Figure 2.3c–e). These differences are similar to the values 2.1×10^{-4} , 9×10^{-5} , and 4×7^{-5} identified by [Evans and Stephens \[1991\]](#). More recently, Rayleigh-atmosphere benchmark results have been re-computed by [Vijay and Hovenier \[2012\]](#) to a much higher degree of accuracy; this work also included benchmarking of the VLIDORT model.

Figure 2.4 shows benchmark calculations of four Stokes parameters for radiative transfer in an aerosol-only atmosphere. [Garcia and Siewert \[1989\]](#) documented their results for unpolarized incident radiation at 951 nm and $\cos\Theta_0$ of 0.2, for an atmosphere with a Lambertian reflectance of 0.1. The aerosols in that atmosphere were assumed to satisfy a gamma-function size distribution with r_{eff} of 0.2 μm and v_{eff} of 0.07, and a refractive index yielding an aerosol single scattering albedo of 0.99. Compared to their results, the Stokes parameters computed by UNL-VRTM show relative differences of less than 0.6%, with maximum relative differences (at certain viewing geometries) of up to 2% for Q and 3.8% for V . The DOLP computed from the UNL-VRTM (with 15 streams for the hemisphere) and documented by [Garcia and Siewert \[1989\]](#) (with 3 streams) differ on average by 0.5%, with a maximum relative difference of 0.65%.

The simultaneous calculation of analytic Jacobians of the four Stokes parameters with respect to the aerosol optical depth, size parameters, refractive indices, and aerosol-loading peak height for both fine and coarse model aerosols may be validated against Jacobians calculated using the finite difference method (Figures 2.5 and 2.6). Overall, results from the two methods are highly correlated as seen in the scatter plots shown in these figures. Relative differences in all comparisons are less than 0.5%, and in many cases the differences are less than 0.05%.

2.4 Acknowledgements

I thank Rob Spurr for sharing the VLIDORT, Linearized Mie, and Linearized T-matrix codes, Xiong Liu and Kelly Chance for providing the HITRAN database and the line-by-line computing code. I also thank Shouguo Ding for plotting Figures 2.2 and 2.3. Funding for this study was provided by the NASA Earth Science Division as part of GEO-CAPE mission study and Glory mission science activities. This chapter has been published in an article in *Journal of Quantitative Spectroscopy and Radiative Transfer* [[Wang et al., 2014](#)].

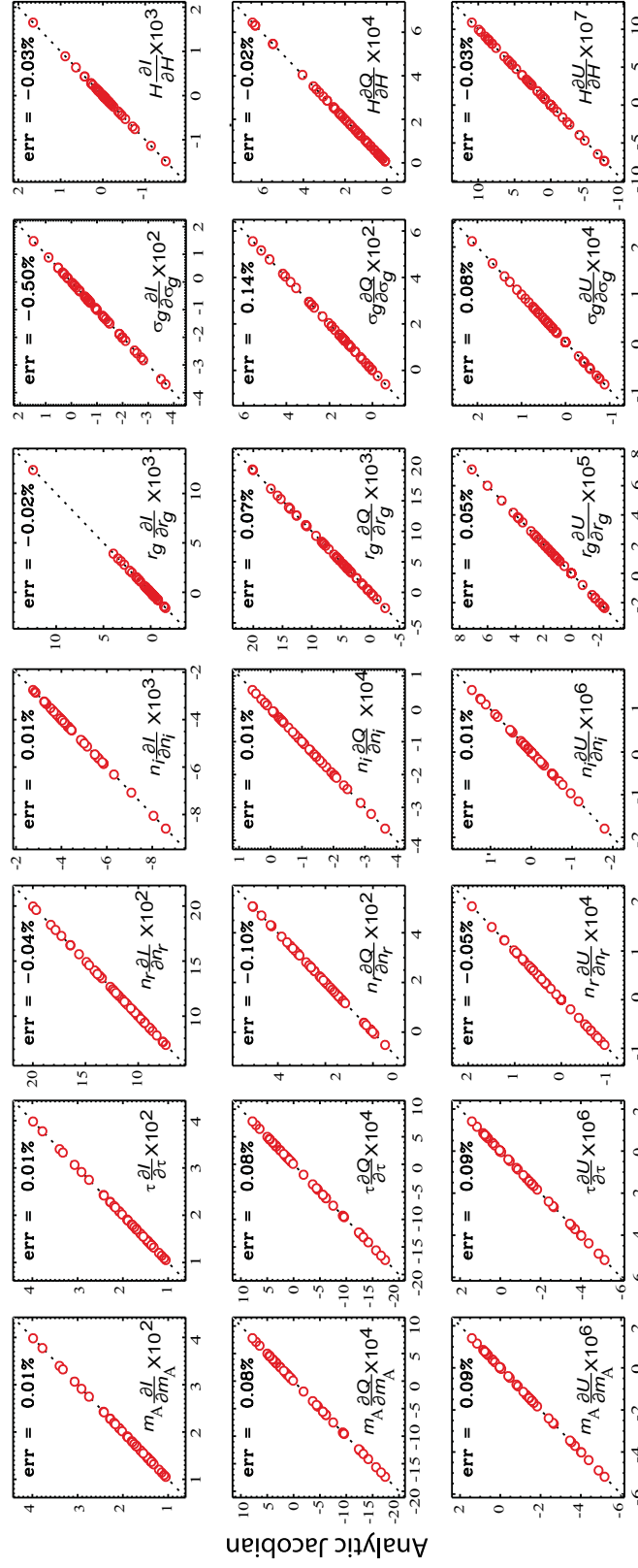


Figure 2.5: Intercomparison of Jacobians ($\partial \xi / \partial \ln x$) calculated with UNL-VRTM using the analytical method (y-axis) with those computed from UNL-VRTM using finite-difference estimates (x-axis). Here ξ is one of the Stokes parameters: I (top row), Q (middle row), and U (last row). x is one of 7 parameters associated with fine-mode aerosols: mass concentration m_A , τ_A , m_r , m_i , r_g and σ_g (of the lognormal PSD), and height (H) of peak aerosol concentration in the vertical. Note, the calculation is done for an atmosphere containing both fine- and coarse-mode aerosols as described in [Hess et al. \[1998\]](#). (Figure adopted from [Wang et al. \[2014\]](#).)

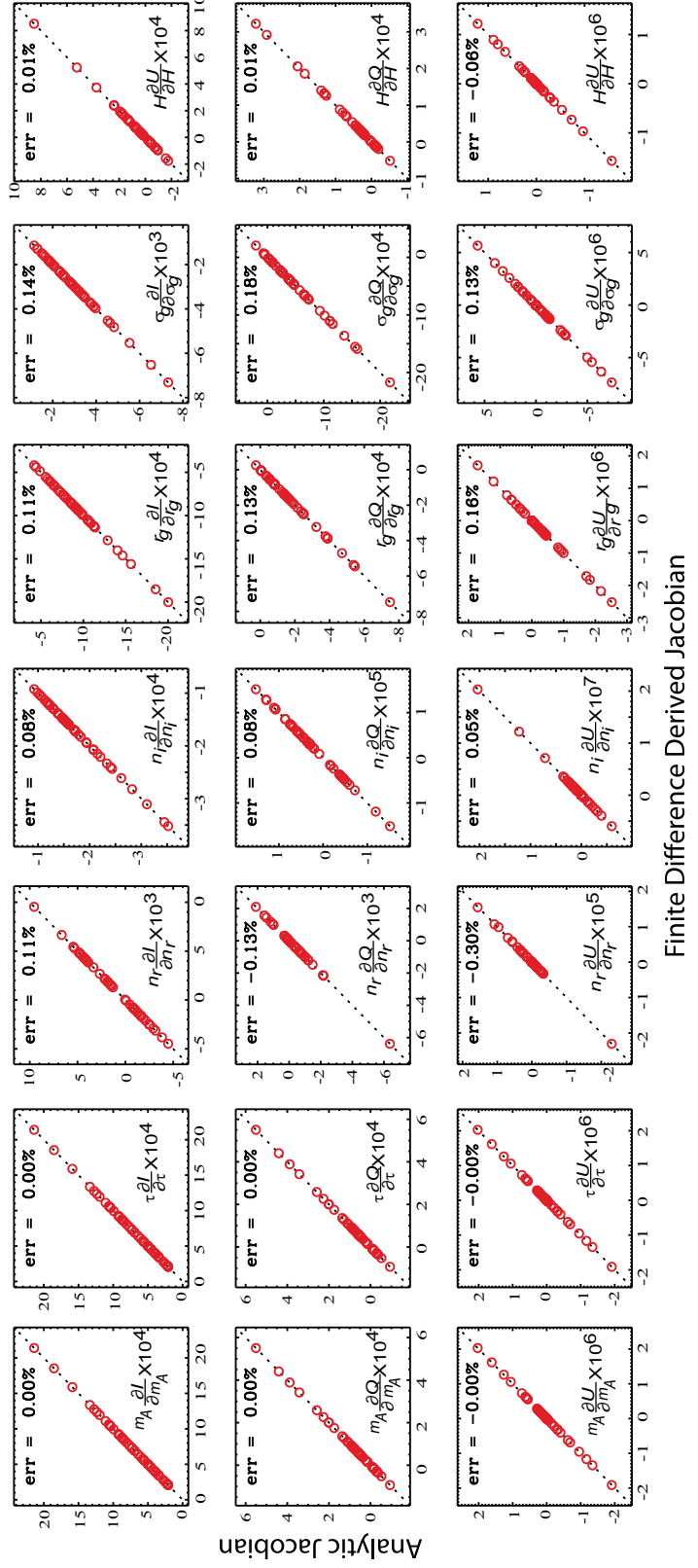


Figure 2.6: Same as in Figure 2.5, but for coarse mode aerosols. (Figure adopted from Wang *et al.* [2014])

CHAPTER 3

INVERSION THEORIES AND ALGORITHM

3.1 Introduction

The inverse problem of this work seeks the solution of a number of microphysical parameters from observations of different categories. We thus need to develop an retrieval algorithm that uses statistically optimized multi-variable fitting, in which the solution is sought not only rely on the presumed classes of potential solutions, but also in a continuous space of solutions under statistically formulated criteria optimizing the error distribution of the retrieval parameters. It should be noted that the development of this inversion algorithm was built upon our experience with optimization of aerosol emissions using the adjoint chemistry transport model (CTM) (See Appendix B and [[Wang et al., 2012; Xu et al., 2013](#)]). In essence, the optimization method is consistent with the adjoint modeling [e.g., [Henze et al., 2007](#)] that constrains aerosol emissions from measurements through inverting a CTM, although different physical processes are involved for inversion of AERONET observation. Both inversions seek the optimal solutions for a state vector that minimizes the differences between the model simulation and observation.

In this chapter, I first present the general theory of inverse problem (section 3.2), covering the Bayesian-based inversion (section 3.2.1) and information content analysis (3.2.2). After that in section 3.3, I describe the key aspects of designed inversion algorithm: the definition of the state vector (section 3.3.1) and considered constraining its *a priori* and smoothness

feature (section 3.3.2), how the state vector is sought statistically (section 3.3.3), how the retrieval error is characterized (section 3.3.4), and quality control of measurements (section 3.3.5).

It should be noted that

3.2 Inversion Theories

3.2.1 Maximum a posteriori solution of an inverse problem

Let \mathbf{x} denote a state vector that contains n parameters to be retrieved (such as PSD parameters and complex indices of refraction), and \mathbf{y} an observation vector with m elements of measurements (such as multi-band radiances from different viewing angles). Furthermore, let \mathbf{F} indicate a forward model (such as the radiative transfer model) that describes the physics on how \mathbf{y} and \mathbf{x} are related. Then, we have

$$\mathbf{y} = \mathbf{F}(\mathbf{x}, \mathbf{b}) + \boldsymbol{\epsilon}_y \quad (3.1)$$

where the vector \mathbf{b} consists of forward model parameters (such as the surface reflectance) that are not included in \mathbf{x} but quantitatively influence the estimates to our known, and $\boldsymbol{\epsilon}_y$ term is the error that results from inaccurate modeling and measurement processes. In this study, we use the best-estimated $\hat{\mathbf{b}}$ in the forward model and consider its contributions to the total measurement accuracy. Linearizing the forward model at $\mathbf{b} = \hat{\mathbf{b}}$:

$$\mathbf{y} = \mathbf{F}(\mathbf{x}, \hat{\mathbf{b}}) + \hat{\mathbf{K}}_b(\mathbf{b} - \hat{\mathbf{b}}) + \boldsymbol{\epsilon}_y \quad (3.2)$$

where $\hat{\mathbf{K}}_b$ is the weighting function (or Jacobian matrix) of the forward model to model parameters \mathbf{b} at $\hat{\mathbf{b}}$, $\left. \frac{\partial \mathbf{F}}{\partial \mathbf{b}} \right|_{\mathbf{b}=\hat{\mathbf{b}}}$. If we treat the forward model as linear in the vicinity of the true

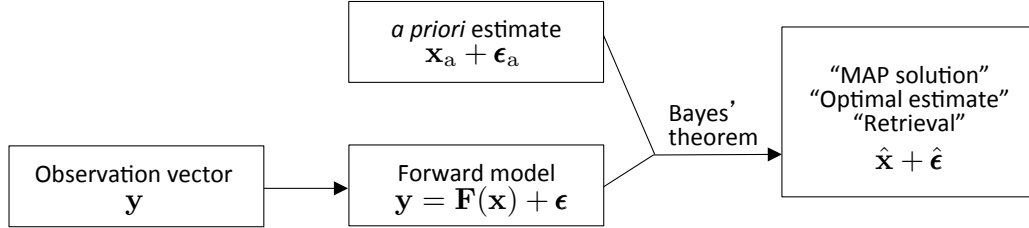


Figure 3.1: The concept of an inverse problem that optimizing an estimates from observations.
(Courtesy: Daniel Jacobs)

state of x , the forward model can be rewritten as:

$$\mathbf{y} = \mathbf{K}\mathbf{x} + \boldsymbol{\epsilon} \quad (3.3)$$

Where $\boldsymbol{\epsilon}$ represents the error that sums the errors from forward modeling and measurement processes. We only consider the errors propagated from errors in \mathbf{b} , but omit any other source in the forward modeling. Thus, $\boldsymbol{\epsilon} = \boldsymbol{\epsilon}_y + \hat{\mathbf{K}}_b \boldsymbol{\epsilon}_b$, where $\boldsymbol{\epsilon}_b = \mathbf{b} - \hat{\mathbf{b}}$ indicates error of \mathbf{b} . K is the $m \times n$ Jacobian matrix comprising derivatives of the forward model with respect to each retrieved parameter, $\frac{\partial \mathbf{F}}{\partial \mathbf{x}}$.

The inverse problem is to solve \mathbf{x} from the measurement \mathbf{y} by inverting the forward model \mathbf{F} . In many situations, the forward model is a complex process with large number of internal uncertainties. As a result, the inverse problem tends to be an ill-posed problem. In this regard, the *a priori* constraints are usually considered. *A priori* represents the knowledge of the state before the measurement is made. And the true state occurs nearby the *a priori*:

$$\mathbf{x} = \mathbf{x}_a + \boldsymbol{\epsilon}_a. \quad (3.4)$$

where \mathbf{x}_a is the *a priori estimate* and $\boldsymbol{\epsilon}_a$ indicates *apriori* error.

Then, the inverse problem becomes to solve the equation set (as illustrated in Figure

3.1):

$$\begin{cases} \mathbf{y} = \mathbf{Kx} + \boldsymbol{\epsilon} \\ \mathbf{x} = \mathbf{x}_a + \boldsymbol{\epsilon}_a. \end{cases} \quad (3.5)$$

Provided that errors of measurements and the a priori are characterized by a Gaussian probability distribution function (PDF) and the forward model is linear in the vicinity of the true state, the maximum a posteriori (MAP) solution of the state vector, also called the retrieval or the a posteriori, can be derived with the Bayes's Theorem [Rodgers, 2000]:

$$\hat{\mathbf{x}} = \mathbf{x}_a + (\mathbf{K}^T \mathbf{S}_y^{-1} \mathbf{K} + \mathbf{S}_a^{-1})^{-1} \mathbf{K}^T \mathbf{S}_y^{-1} (\mathbf{y} - \mathbf{Kx}_a) \quad (3.6)$$

Here, \mathbf{S}_a is the error covariance matrix of *a priori*, \mathbf{x}_a ; \mathbf{S}_y is the error covariance matrix of the measurements; T denote matrix transpose operation.

The "retrieval", $\hat{\mathbf{x}}$, in above equation (3.6) is corresponding to the maximum posterior PDF and the minimum of a cost function defined by

$$J = (\mathbf{y} - \mathbf{Kx})^T \mathbf{S}_y^{-1} (\mathbf{y} - \mathbf{Kx}) + (\mathbf{x} - \mathbf{x}_a)^T \mathbf{S}_a^{-1} (\mathbf{x} - \mathbf{x}_a). \quad (3.7)$$

J is indeed the negative exponent term of the posterior PDF, which also follows a Gaussian shape with the expected value of $\hat{\mathbf{x}}$ and the error covariance matrix $\hat{\mathbf{S}}$ given by

$$\hat{\mathbf{S}}^{-1} = \mathbf{K}^T \mathbf{S}_y^{-1} \mathbf{K} + \mathbf{S}_a^{-1}. \quad (3.8)$$

$\hat{\mathbf{S}}$ describes the statistical uncertainties in retrieved $\hat{\mathbf{x}}$ due to measurement noise, forward modeling uncertainty, and smoothing error [Rodgers, 2000]. The square roots of its diagonals are the one-sigma uncertainties of each retrieved parameters given the observation uncertainties, forward model uncertainties, and prior knowledge of the state. With $\hat{\mathbf{S}}$, we can

also estimate the uncertainty for any parameter (for example, the aerosol single scattering albedo in this study) that can be fully determined by parameters (for example, aerosol refractive index and PSD parameters) in \mathbf{x} but is not directly retrieved. If one parameter is a function defined by $\zeta = \text{zeta}\mathbf{x}$, then the uncertainty in derived ζ is [Rodgers, 2000]:

$$\hat{\varepsilon}_\zeta = \sqrt{\sum_{i=1}^n \sum_{j=1}^n \frac{\partial \zeta}{\partial x_i} \frac{\partial \zeta}{\partial x_j}}. \quad (3.9)$$

3.2.2 Information theory

The Jacobian matrix \mathbf{K} usually serves as gradients in the sensitivity analysis and can be a useful indicator of information. For a linear system in the absence of measurement error, the rank of \mathbf{K} indicates independent pieces of information that can be determined from the measurements. In practice, error inevitably presents in measurements and thus can impact the effective rank. To identify the effective sensitivity of individual measurement to each retrieved parameter, we define the error-normalized (EN) Jacobian matrix by

$$\tilde{\mathbf{K}} = \mathbf{S}_y^{-\frac{1}{2}} \mathbf{K} \mathbf{S}_a^{\frac{1}{2}} \quad (3.10)$$

$\tilde{\mathbf{K}}$ is also called the ‘pre-whitening’ by Rodgers [2000]. The superiority of the matrix $\tilde{\mathbf{K}}$ over the matrix \mathbf{K} is that it compares the observation error covariance ($\mathbf{S}_y^{\frac{1}{2}}$) with the natural variability of the observation vector as expressed by its prior covariance ($\mathbf{K} \mathbf{S}_a^{\frac{1}{2}}$). Any component whose natural variability is smaller than the observation error is not measurable. Therefore, an element $\tilde{\mathbf{K}}_{i,j}$ less than unity indicates that the measurement component y_i contains null useful information for determining parameter x_j . In contrast, when $\tilde{\mathbf{K}}_{i,j} > 1$, the larger of its value, the more useful information retained in y_i for determining x_j . Therefore, the $\tilde{\mathbf{K}}$ matrix provides not only sensitivity of individual measurements to each retrieved

parameter, but also a capacity-metric for those observations to infer retrieved parameters.

The averaging kernel matrix has been widely used to quantify the information gained by making a measurement [e.g., *Rodgers*, 1998; *Hasekamp and Landgraf*, 2005a; *Frankenberg et al.*, 2012; *Sanghavi et al.*, 2012]. It provides the sensitivity of the retrieval to the true state and is defined by

$$\mathbf{A} = \frac{\partial \hat{\mathbf{x}}}{\partial \mathbf{x}}. \quad (3.11)$$

Replace y in equation (3.6) with equation (3.3) at $\mathbf{x} = \mathbf{x}_a$,

$$\hat{\mathbf{x}} = \mathbf{x}_a + (\mathbf{K}^T \mathbf{S}_y^{-1} \mathbf{K} + \mathbf{S}_a^{-1})^{-1} \mathbf{K}^T \mathbf{S}_y^{-1} [\mathbf{K}(\mathbf{x} - \mathbf{x}_a) + \boldsymbol{\epsilon}] \quad (3.12)$$

Then we have

$$\mathbf{A} = \frac{\partial \hat{\mathbf{x}}}{\partial \mathbf{x}} = (\mathbf{K}^T \mathbf{S}_y^{-1} \mathbf{K} + \mathbf{S}_a^{-1})^{-1} \mathbf{K}^T \mathbf{S}_y^{-1} \mathbf{K} \quad (3.13)$$

Matrix \mathbf{A} quantifies the ability of the retrieval to infer $\hat{\mathbf{x}}$ given the relationship between y and \mathbf{x} (i.e., \mathbf{K}) and given the observation noise and a priori characterization. Thus, an identity matrix of \mathbf{A} represents a perfect retrieval, while a null matrix of \mathbf{A} indicates that no information can be gained from the observation. The trace of \mathbf{A} is the degree of freedom for signal, i.e., $DFS = \text{Trace}(\mathbf{A})$, which represents independent pieces of information that the observation can provide. The diagonal elements of the averaging kernel matrix \mathbf{A} , or the DFS components, indicate the partial sensitivity of each individual retrieved parameters with respect to their corresponding truth:

$$\mathbf{A}_{i,i} = \frac{\partial \hat{x}_i}{\partial x_i} \quad (3.14)$$

Clearly, $\mathbf{A}_{i,i} = 1$ indicates that the observation is capable of fully characterizing the truth of x_i ; while $\mathbf{A}_{i,i} = 0$ indicates the observation contains zero information on x_i and x_i is

not measurable. From the formulation of $\hat{\mathbf{S}}$ and \mathbf{A} , we can conclude that only the error covariance and Jacobian matrix, but not the retrieval, are important for the purpose of understanding information content.

Other quantities used for information analysis of a measurement include the Shannon information content (SIC) [Shannon, 1948] and the Fisher information matrix. SIC, a widely used quantity [e.g., Rodgers, 1998; Knobelspiesse et al., 2012], is defined as the reduction in entropy after the measurement

$$H = \frac{1}{2} \ln |\mathbf{S}_a| - \frac{1}{2} \ln |\hat{\mathbf{S}}| = -\frac{1}{2} \ln |\hat{\mathbf{S}} \mathbf{S}_a^{-1}| = -\frac{1}{2} \ln |\mathbf{I}_n - \mathbf{A}| \quad (3.15)$$

where \mathbf{I}_n is an identity matrix of order n . Clearly, SIC is highly related to the DFS for the information analysis. In the Gaussian linear case, the Fisher information matrix is equal to the inverse of *a posteriori* error covariance matrix, $\hat{\mathbf{S}}^{-1}$. The retrieval indeed corresponds to the maximum of *a posteriori* PDF and the minimum of retrieval error. It is thus straightforward that a higher level of the Fisher information is subject to a smaller retrieval error. Due to their close relationship with the DFS and $\hat{\mathbf{S}}$, we will not present the SIC and Fisher information analysis in this study.

3.3 New Research Algorithm for AERONET Inversion

Figure 3.2 gives an overview of the retrieval algorithm specifically designed for the analysis and inversion of photo-polarimetric remote sensing observations, such as those from AERONET. The algorithm builds upon the UNified and Linearized Vector Radiative Transfer Model (UNL-VRTM), which consists of seven component modules for the forward simulation of observations (section 2.2). The forward modeling includes the linearized vector radiative transfer model (VLIDORT) developed by Spurr [2006], a linearized Mie

code and a linearized T-Matrix code calculating aerosol single scattering properties [Spurr *et al.*, 2012], a module calculating Rayleigh scattering and a module for gas absorption, plus a surface model computing bidirectional reflectance/polarization distribution function (BRDF/BPDF) [Spurr, 2004]. The required input parameters for the algorithm are the relevant atmospheric profiles (of pressure, temperature, and gaseous mixing ratio), aerosol loading in terms of AOD or aerosol columnar volume, aerosol vertical profiles, aerosol microphysical and chemical parameters (size distribution and complex refractive index), and surface reflection parameters. The users can specify up to two modes of the aerosol population. Each mode is characterized by the total particle number (or volume), the vertical profile, size distribution, and refractive index. The aerosol-related modules—Mie, T-matrix, and VLIDORT—are analytically linearized and fully coupled. Thus, the forward model not only simulates radiance and/or polarization for a given spectrum, but also simultaneously computes the Jacobians of these radiation fields with respect to input aerosol microphysical parameters. Our inversion-oriented UNL-VRTM supplies these Jacobians together with observation error characterizations and *a priori* constraints to the statistical optimization procedure for the retrieval. Objective information content (section 3.2.2) and error analysis (section 3.2.1) are also included in the procedure along with the inversion. Although our algorithm is tailored to measurements from the AERONET SunPhotometer, its modularized framework enables the simulation and inversion of observations from various platforms, including satellite sensors.

Development of the inversion component in our algorithm was built upon our experience with optimization of aerosol emissions using the adjoint chemistry transport model (CTM) (See Appendix B and [Wang *et al.*, 2012; Xu *et al.*, 2013]). In essence, the optimization method is consistent with the adjoint modeling [e.g., Henze *et al.*, 2007] that constrains aerosol emissions from measurements through inverting a CTM, although different physical processes are involved for inversion of AERONET observation. Both inversions seek

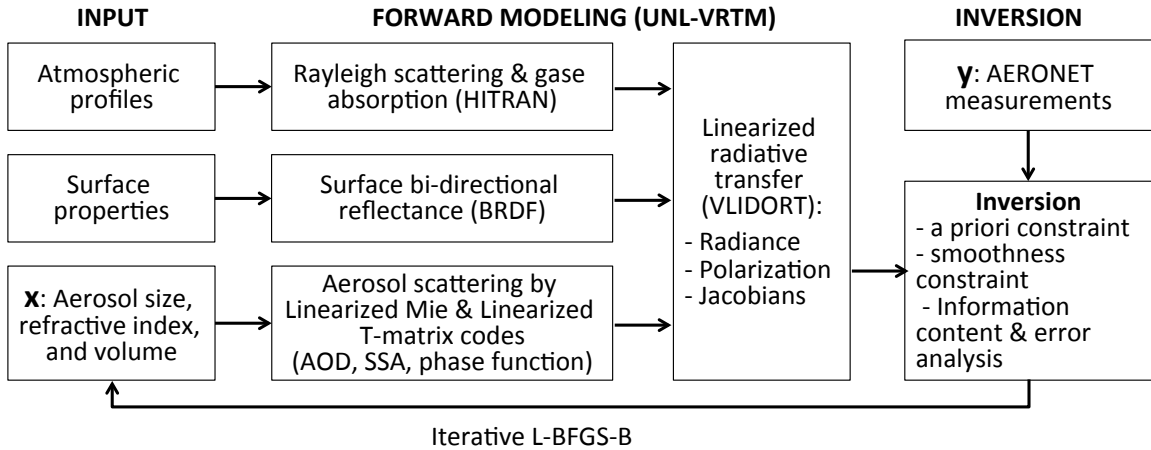


Figure 3.2: General structure of the new research inversion algorithm for the retrieval of aerosol microphysical parameters from AERONET photo-polarimetric measurements.

the optimal solutions for a state vector that minimizes the differences between the model simulation and observation. In addition, our algorithm inherits the inversion strategy from the Dubovik00&06 algorithm, in particular with regard to the smoothness constraint on the spectral dependence of the complex refractive index.

3.3.1 Definition of state vector and observation vector

For this study, the observation vector \mathbf{y} comprises components from different sources. As listed in Table 3.1 (and Table 1.1 for specific measurements by the SunPhotometer), there are four categories of observations, i.e., the direct sun AOD, the sky radiance around the solar aureole, the sky radiance in the solar principal plane, and the DOLP in the solar principal plane, with all measurements performed at 440, 675, 870, and 1020 nm. Also indicated in Table 3.1 are the calibration errors and other measurement uncertainties that make of the term $\boldsymbol{\varepsilon}$.

The state vector x contains 11 pairs of parameters characterizing aerosol properties in the fine and the coarse modes, respectively, the columnar volume concentration V_0 , the effective radius r_{eff} , the effective variance v_{eff} , and the complex refractive index $m_r - m_i i$ at 440, 675,

Table 3.1: AERONET observation characteristics.

| Symbol | Parameter | Instrumental uncertainty | Other uncertainties |
|--------|----------------------------------|--------------------------|----------------------------------|
| y_1 | Direct sun AOD | 0.01–0.02 | ~0.02 spatial/temporal variation |
| y_2 | Sky radiance in solar almucantar | 5% | Surface BRDF and BPDF |
| y_3 | Sky radiance in principal plane | 5% | Surface BRDF and BPDF |
| y_4 | DOLP in principal plane | 0.01 | Surface BRDF and BPDF |

870, and 1020 nm (Table 3.2). r_{eff} and v_{eff} are two commonly used size parameters in the aerosol radiative quantification, because different types of size distribution function having same values of r_{eff} and v_{eff} possess similar scattering and absorption properties [Hansen and Travis, 1974]. In line with many studies [Schuster et al., 2006; Hasekamp and Landgraf, 2005a, 2007; Mishchenko et al., 2007; Waquet et al., 2009], we assume the aerosol PSD follows a bi-modal lognormal function expressed in equation (2.10). All parameters include both the fine and coarse modes and account for a total of 22 elements ($n = 22$).

3.3.2 Combine a priori and smoothness constraints

A priori information describes our knowledge of the state vector before measurements are applied, and an *a priori* constraint is commonly used to achieve a well-defined stable and physically reasonable solution to an ill-posed problem. Usually, a priori knowledge comprises both a mean state \mathbf{x}_a and its error $\boldsymbol{\epsilon}_a$ (equation (3.4)). One of the satisfactory sources for the *a priori* knowledge is a climatology based on historical measurements. For a given AERONET site, we use the available inversion products that have been obtained with the Dubovik00&06 algorithm, for which the *a priori* can be well characterized by the mean values and standard deviations of each component in the state vector. At the same time, the *a priori* can also be determined from other sources if a historical AERONET retrieval is not available. For example, we could extract aerosol microphysical climatology from chemistry

Table 3.2: State vector elements and associated constraints for inversion.^a

| Symbol | Parameter | <i>a priori</i> constraint? | Smoothness constraint? |
|--------------------------------------|--|--------------------------------|---------------------------|
| V_0^f, V_0^c | Columnar volume ($\mu\text{m}^3 \mu\text{m}^{-2}$) | ✓ | |
| $r_{\text{eff}}^f, r_{\text{eff}}^c$ | Effective radiance (μm) | ✓ | |
| $v_{\text{eff}}^f, v_{\text{eff}}^c$ | Effective variance | ✓ | |
| $\mathbf{m}_r^f, \mathbf{m}_r^c$ | Real part refractive index | ✓ | ✓ |
| $\mathbf{m}_i^f, \mathbf{m}_i^c$ | Imaginary part refractive index | ✓ | ✓ |

^aThe superscripts, ‘c’ and ‘f’, respectively denote fine and coarse aerosol modes. Refractive indices are for spectral wavelengths of 440, 675, 870, and 1020 nm.

transport model simulations [e.g., [Wang et al., 2010](#)] or from measurements of in situ and/or even satellite sensors.

Among those retrieved parameters, the aerosol volumes— V_0^f and V_0^c —are the most variable or uncertain quantities. A reasonable initial guess for these quantities could speed up the iterative inversion. Here, we “look up” their initial values from the AOD measurements at two spectral wavelengths. Given the *a priori* information on the aerosol PSD and refractive indices, the aerosol extinction efficiency Q_{ext} can be obtained for each fine and coarse mode with the Mie code. And the AOD is related to the V_0^f and V_0^c via equation:

$$\tau_A = \tau_A^f + \tau_A^c = \frac{3V_0^f Q_{\text{ext}}^f}{4r_{\text{eff}}^f} + \frac{3V_0^c Q_{\text{ext}}^c}{4r_{\text{eff}}^c}. \quad (3.16)$$

Clearly, applying the above equation to the AODs at any two spectral wavelengths, we can easily solve V_0^f and V_0^c .

For some parameters, the *a priori* estimates may be poorly known, but these parameters behave smoothly with no sharp oscillations. For example, the aerosol refractive index usually does not vary rapidly over the visible to near-infrared spectral range. In this regard, a smoothness constraint could be a preferable addition. The technique of constraining a smooth solution was pioneered by [Phillips \[1962\]](#); [Twomey \[1963\]](#), and has been successfully used

to retrieve coherent aerosol size distributions [Dubovik and King, 2000] and atmospheric vertical profiles [Twomey, 1977]. The principle of the smoothness constraint is to restrain the degree of non-linearity of a certain physical parameter by limiting the values of its d th derivatives:

$$\mathbf{G}_d + \boldsymbol{\epsilon}_\Delta = \mathbf{0} \quad (3.17)$$

where \mathbf{G}_d is a differential matrix composed of coefficients for calculating the d th derivatives of \mathbf{x} with respect to the dependent variable, and the vector $\boldsymbol{\epsilon}_\Delta$ indicates uncertainties in these derivatives.

In particular, for constraining the dependence of the spectral refractive index with wavelength, the matrix \mathbf{G}_d calculates the d th difference of the refractive index at four wavelengths (440, 675, 870, and 1020 nm). As discussed by Dubovik and King [2000], we assume a linear relationship between the logarithm of the refractive index and the logarithm of the wavelength: $m_r \sim \lambda^{-\alpha}$, and $m_i \sim \lambda^{-\beta}$. Further, the matrix \mathbf{G}_1 for the first difference (of either m_r or m_i of one mode) can be expressed as:

$$\begin{aligned} \mathbf{G}_1 &= \begin{bmatrix} 1/\Delta\lambda_1 & 0 & 0 \\ 0 & 1/\Delta\lambda_2 & 0 \\ 0 & 0 & 1/\Delta\lambda_3 \end{bmatrix} \begin{bmatrix} -1 & 1 & 0 & 0 \\ 0 & -1 & 1 & 0 \\ 0 & 0 & -1 & 1 \end{bmatrix} \\ &= \begin{bmatrix} -1/\Delta\lambda_1 & 1/\Delta\lambda_1 & 0 & 0 \\ 0 & -1/\Delta\lambda_2 & 1/\Delta\lambda_2 & 0 \\ 0 & 0 & -1/\Delta\lambda_3 & 1/\Delta\lambda_3 \end{bmatrix} \end{aligned} \quad (3.18)$$

Here, $\Delta\lambda_1$, $\Delta\lambda_2$, and $\Delta\lambda_3$ are the denominators for the first-order differences in the logarithm, e.g., $\Delta\lambda_1 = \ln \frac{675}{440}$. As to $\boldsymbol{\epsilon}_\Delta$, we assume errors in first differences of the refractive index following Dubovik and King [2000], i.e., 0.2 for m_r and 1.5 for m_i .

Similar to the approach suggested by Dubovik and King [2000], we use multiple *a priori*

constraints in the retrieval. Specifically, we combine the *a priori* constraint of equation (3.4) and the smoothness constraint of equation (3.17); our inverse problem is equivalent to solving the following set of three equations (in contrast to (3.5) that has two equations):

$$\begin{cases} \mathbf{y} = \mathbf{F}(\mathbf{x}) + \boldsymbol{\epsilon} \\ \mathbf{x} = \mathbf{x}_a + \boldsymbol{\epsilon}_a \\ \mathbf{0} = \mathbf{G}_d + \boldsymbol{\epsilon}_\Delta. \end{cases} \quad (3.19)$$

3.3.3 Statistical optimized inversion

Under the assumption of Gaussian-distributed errors, the optimized solution of equation (3.19) according to the MAP method corresponds to the state vector that minimizes the quadratic cost function consisting of multiple terms [Dubovik and King, 2000; Dubovik, 2004]:

$$J(\mathbf{x}) = \boldsymbol{\gamma}_y [\mathbf{y} - \mathbf{F}(\mathbf{x})]^T \mathbf{S}_y^{-1} [\mathbf{y} - \mathbf{F}(\mathbf{x})] + \boldsymbol{\gamma}_a (\mathbf{x} - \mathbf{x}_a)^T \mathbf{S}_a^{-1} (\mathbf{x} - \mathbf{x}_a) + \boldsymbol{\gamma}_\Delta \mathbf{x}^T \boldsymbol{\Omega} \mathbf{x}. \quad (3.20)$$

where $\boldsymbol{\Omega}$ is a smoothing matrix related to \mathbf{G}_d and the error covariance matrix \mathbf{S}_Δ (of the d th derivatives of \mathbf{x}) by $\boldsymbol{\Omega} = \mathbf{G}_d^T \mathbf{S}_\Delta^{-1} \mathbf{G}_d$. The vectors $\boldsymbol{\gamma}_y$, $\boldsymbol{\gamma}_a$, and $\boldsymbol{\gamma}_\Delta$ are regularization parameters. In principle, the minimization of three-term cost function given by the equation (3.20) is conceptually analogous to the minimization of bi-component cost functions (3.7) generally considered in the Bayesian approach [Rodgers, 2000]. These three terms on the right-hand side of equation (3.20) represent, respectively, (1) the total squared fitting error incurred owing to departures of the model predictions from the observations, (2) the penalty error incurred owing to departures of the estimates from the a priori, and (3) the penalty error incurred owing to departures from the defined smoothness feature. Overall,

the minimization of $J(\mathbf{x})$ achieves the objective of improving the agreement between the model and the measurements while ensuring that the solution remains within a reasonable range and degree of smoothness.

The regularization parameters in the calculation of $J(\mathbf{x})$ act as weights to balance the fitting error and the penalty errors. Clearly, a good assignment of $\boldsymbol{\gamma}$ is of crucial importance for the statistical optimal solution. High values of $\boldsymbol{\gamma}_a$ and $\boldsymbol{\gamma}_\Delta$ can lead to over-smoothing of the solution with little improvement to the fitting residuals, while low values minimize the error term at the cost of greatly increasing the parameter penalty terms. Optimal values of $\boldsymbol{\gamma}$ for two-term cost functions can be identified at the corner near the origin of the so-called L-curve [Hansen, 1998]. However, such approach is not appropriate to the multi-term cost function. In this study, we assume equal weights for observational constraint term and combined *a priori* constrain terms in the cost function:

$$\boldsymbol{\gamma}_a = \frac{1}{2}n^{-1}\mathbf{e}, \quad \boldsymbol{\gamma}_\Delta = \frac{1}{2}(n_\Delta - d)^{-1}\mathbf{e}, \quad \boldsymbol{\gamma}_y = \left\langle \frac{1}{4m_k} \right\rangle_{k=1,4} \quad (3.21)$$

Here, d is the order of difference, \mathbf{e} is a vector consisting of n elements of 1, and n_Δ is the number of state elements that are supplied with smoothness constraints. Values for $\boldsymbol{\gamma}_y$ are chosen to control the fitting residuals for observations of four different categories as listed in Table 3.1. Each group comprises the number of m_k observations for k from 1 to 4. The corresponding elements of $\boldsymbol{\gamma}_y$ for the k th group are $\frac{1}{4m_k}$, which means the observation quadratic term is normalized by the observation count of each group.

In principle, solving this inverse problem is tantamount to a pure mathematical minimization procedure. The minimization of $J(\mathbf{x})$ equation (3.20) is performed with an iterative quasi-Newton optimization approach using the L-BFGS-B algorithm [Byrd *et al.*, 1995; Zhu *et al.*, 1994], which offers bounded minimization to ensure the solution stays within a physically reasonable range. The L-BFGS-B algorithm requires knowledge of \mathbf{x}_a and $J(\mathbf{x})$,

as well as the gradient of $J(\mathbf{x})$ with respect to \mathbf{x} , or $\nabla_{\mathbf{x}}J$. By linearizing the forward model $\mathbf{F}(\mathbf{x})$, we can determine $\nabla_{\mathbf{x}}J$ by

$$\nabla_{\mathbf{x}}J(\mathbf{x}) = \boldsymbol{\gamma}_y \mathbf{K}^T \mathbf{S}_y^{-1} [\mathbf{y} - \mathbf{F}(\mathbf{x})] + \boldsymbol{\gamma}_a \mathbf{S}_a^{-1} (\mathbf{x} - \mathbf{x}_a) + \boldsymbol{\gamma}_{\Delta} \boldsymbol{\Omega} \mathbf{x}. \quad (3.22)$$

Here, the Jacobian matrix \mathbf{K} is computed analytically by the UNL-VRTM (section 2.2) through equations (2.15) and (2.16). At each iteration, improved estimates of the state vector are implemented and the forward simulation is recalculated. The convergence criterion to determine the optimal solution is the smallness of the reduction of $J(\mathbf{x})$ and the norm of $\nabla_{\mathbf{x}}J(\mathbf{x})$. The iteration stops when the reduction of $J(\mathbf{x})$ is less than 1% within 10 continuous iterations. Then, the optimal solutions are identified corresponding to the smallest norm of $\nabla_{\mathbf{x}}J(\mathbf{x})$ from these 10 last iterations. In addition, to ensure a physically reasonable solution, we also perform retrieval error analysis, and impose a practical quality control on real measurements.

3.3.4 Characterizing retrieval error

The retrieval without error characterization is of significantly lesser value. Once the retrieval is achieved, the retrieval error can be characterized by the *a posteriori* state, and the error analysis can be performed in terms of a linearization of the problem around the solution $\hat{\mathbf{x}}$. We estimate the retrieval error on each state vector element using the error covariance matrix of the *a posteriori* state:

$$\hat{\mathbf{S}}^{-1} = \hat{\mathbf{K}}^T \mathbf{S}_y^{-1} \hat{\mathbf{K}} + \mathbf{S}_a^{-1} + \boldsymbol{\Omega}. \quad (3.23)$$

where $\hat{\mathbf{K}}$ is the Jacobian matrix of the forward model $\mathbf{F}(\mathbf{x})$ at the solution $\hat{\mathbf{x}}$. It should be noted that the above three-term a posteriori formularized according to the three-term cost

function defined in the equation (3.20). Simply, the retrieval error for each element can be estimated by:

$$\hat{\epsilon}_i = \hat{\mathbf{S}}_{i,i}^{\frac{1}{2}} \quad (3.24)$$

With $\hat{\mathbf{S}}$ applied to equation (3.9), we can also estimate the uncertainty in parameters (such as ω_A and asymmetry factor in this study) that can be fully determined by the parameters in \mathbf{x} but are not themselves directly retrieved.

3.3.5 Quality control of measurements

We apply a suite of quality criteria to ensure (a) a cloud-free condition, (b) that aerosol particles are quasi-homogeneously distributed in the horizontal plane within the scanning region, and (c) the measurements are densely populated and cover a wide range of scattering angles so that they provide sufficient information to retrieve all parameters falling within specified uncertainty levels. More specifically, these criteria are as follows: (i) the number of AOD observations ≥ 2 within a ± 25 -minute centered at the period of a full scan sequence; (ii) sky radiance observations are excluded when the scattering angle is less than 3.2° and DOLP observations are excluded when the scattering angle is smaller than 5° ; (iii) a symmetry check for the almucantar radiances: the difference is less than 5% for the azimuthal angle of 180° and less than 10% elsewhere; and (iv) principal-plane observations are discarded when their second derivatives with respect to the scattering angle are beyond the smoothing threshold. Although most of these criteria follow *Holben et al. [2006]*, we also check the smoothness of the principal-plane radiances and DOLP to identify scans that are contaminated by cloud. We apply the threshold on the second derivative of radiance (or DOLP) with respect to scattering angle in order to restrain local oscillations of radiance (or DOLP) caused by clouds or heterogeneous aerosol plumes. Thus, applying such a threshold can effectively remove sharp kinks and ensure continuous quantities in

the principal-plane scanning sequences. Indeed, this smoothness check shares the same principle to the smoothness constraint presented in the section [3.3.2](#).

3.4 Acknowledgements

We thank Daven Henze, Oleg Dubovik, and Brent Holben for constructive suggestions and useful discussions on the inversion algorithm development. This work is supported by a NASA Earth and Space Science Fellowship and the NASA Radiation Sciences Program and the Glory mission program. Most content in this chapter also appear in two articles submitted to *Journal of Geophysical Research – Atmospheres* [[Xu and Wang, 2015](#); [Xu et al., 2015](#)].

CHAPTER 4

INFORMATION CONTENT ANALYSIS

4.1 Introduction

AERONET collects not only the multi-spectral and multi-angular radiance observations, but also the state of light polarization from various viewing angles over many sites (section 1.1.2). Unfortunately, the potential value of AERONET polarization measurements in retrieving aerosol microphysical parameters has not been fully exploited. Polarization measurements contain valuable information about aerosol microphysical properties [*Mishchenko and Travis, 1997; Cairns et al., 1997*], as the polarization of light is highly sensitive to the aerosol size and refractive index [*Hansen and Travis, 1974*]. Several studies have emphasized the usefulness of the polarimetric observations taken by the ground-based instruments [*Cairns et al., 1997; Boesche et al., 2006; Emde et al., 2010; Zeng et al., 2008*]. *Vermeulen et al. [2000]* presented a two-step method to retrieve aerosol microphysical properties from polarized radiances: first, the single scattering albedo and the natural and polarized phase functions were retrieved from transmission and almucantar radiances and polarization in the principal plane; second, the aerosol PSD and refractive index were then derived. With the current AERONET inversion algorithm, *Dubovik et al. [2006]* conducted a case study using polarization data in a UAE² (Unified Aerosol Experiment-United Arab Emirates) field campaign [*Reid et al., 2008*]. *Li et al. [2009]* extended the inversion algorithm of *Dubovik et al. [2006]* to include multi-spectral polarization and demonstrated improved retrievals in

the real part of the aerosol refractive index for fine particles and the fraction of spherical particles.

However, questions regarding the use of AERONET polarimetric observations for retrieving aerosol microphysical parameters remain unresolved: (1) Practically, do the existing AERONET photo-polarimetric measurements have any potential to improve the retrieval of aerosol information content that we now routinely obtain from radiance measurement only? and (2) Hypothetically, how can future upgrades to AERONET photo-polarimetric measurements and inversion algorithm maximize the retrieval information content of AERONET observations? Answering these two questions is not only relevant to the future AERONET instrumentation design, but also for the ground-based passive polarimetric remote sensing of aerosols in general.

In this chapter, we seek to answer above questions from a theoretical perspective (section 3.2.2) by investigating the available information contained in AERONET measurements with and without the inclusion of polarization data. This purpose of this investigation is to provide the a theoretical foundation to support actual algorithm development for using polarimetric data for aerosol retrievals. The structure of this chapter is as follows. In section 4.2, we describe the experimental design on the aerosol models, error characteristics of *a priori* and AERONET measurements. Section 4.3 presents the results of information content

Table 4.1: The aerosol parameters defined for both fine and coarse aerosol modes^a.

| Mode | $r_{\text{eff}}(\mu\text{m})$ | ν_{eff} | \mathbf{m}_r | \mathbf{m}_i | ω_A |
|--------|-------------------------------|--------------------|---------------------------------|----------------------------------|--------------------|
| Fine | 0.21 (80%) | .25 (80%) | 1.44, 1.44, 1.43, 1.42 (.15) | .009, .011, .012, .011 (.01) | .95, .93, .92, .91 |
| Coarse | 1.90 (80%) | .41 (80%) | 1.56, 1.55, 1.54, 1.54 (.15) | .004, .003, .003, .002 (.005) | .84, .91, .93, .96 |

^aThe complex refractive index $\mathbf{m}_r - \mathbf{m}_i i$, and single scattering albedo ω_A are reported at 440, 675, 870, and 1020 nm. Bracketed values are assumed a priori error in relative for r_{eff} and ν_{eff} and in absolute for \mathbf{m}_r , \mathbf{m}_i , and ω_A .

and error analysis. In section 4.4, we investigate the sensitivity of retrieval uncertainties in aerosol parameters with respect to the aerosol loading and fine/coarse aerosol characteristics. Finally, we summarize in section 4.5 the general findings of this study and implications for practical algorithm development.

4.2 Experimental Design

4.2.1 *a priori* characteristics

The state vector \mathbf{x} comprises 22 (11 pairs) retrieved parameters, namely, the columnar volume concentration V_0 , the effective radius r_{eff} , the effective variance v_{eff} , and the complex refractive index $m_r + m_i i$ at 440, 675, 870, and 1020 nm (section 3.3.1). These 11 pairs of parameters characterizing aerosol properties in the both fine and coarse aerosol modes; each mode follows a lognormal PSD function. Table 4.1 displays aerosol size parameters, refractive indices, and single scattering albedo for each size mode adopted for error and information analysis; also showed in brackets are their associated *a priori* uncertainties. The fine-mode particles correspond to water-soluble aerosols obtained from OPAC database [Hess *et al.*, 1998] with updates by Drury *et al.* [2010], while the coarse-mode is for large spherical particles with refractive index from Patterson *et al.* [1977]; Wagner *et al.* [2012].

In order to include various atmospheric conditions, we simulate three types of aerosols—

Table 4.2: The aerosol scenarios adapted for numerical experiments^a.

| Aerosol type | V_0 | fmf_v | τ_A | fmf_τ | AE | ω_A |
|------------------|-------|----------------|--------------------|--------------------|-----|--------------------|
| Fine-dominated | .15 | .8 | 1.0, .58, .36, .25 | .97, .95, .92, .88 | 1.5 | .95, .93, .92, .91 |
| Well-mixed | .22 | .5 | 1.0, .61, .41, .32 | .90, .83, .74, .65 | 1.3 | .94, .93, .92, .93 |
| Coarse-dominated | .43 | .2 | 1.0, .71, .57, .50 | .69, .55, .42, .32 | .82 | .91, .92, .92, .94 |

^aValues for τ_A , ω_A , and fmf_τ are listed respectively for spectral wavelength of 440, 675, 870, and 1020 nm. The AE is reported between 440 and 870 nm. V_0 is in the unit of $\mu\text{m}^3 \mu\text{m}^{-2}$

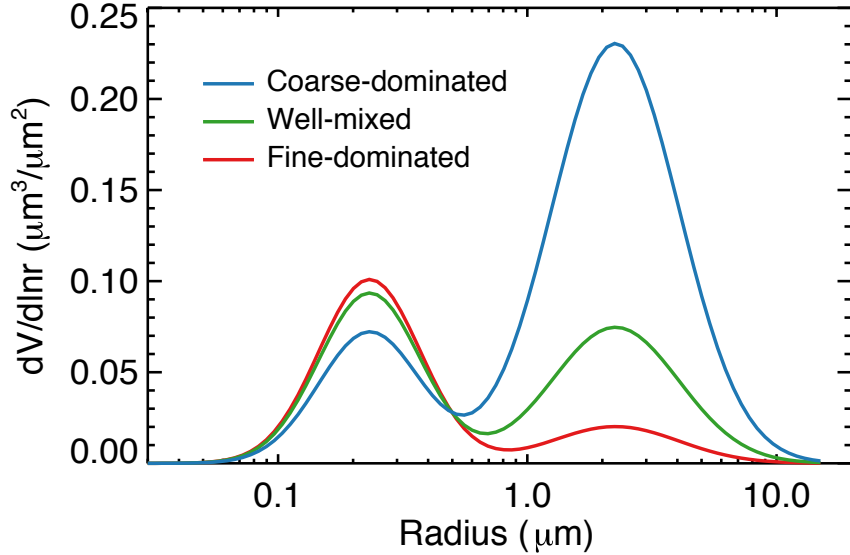


Figure 4.1: Volume size distribution for the aerosol types adopted for the information analysis. Relevant aerosol parameters are summarized in the Tables 4.1 and 4.2.

each with different relative percentage between the coarse and fine modes—(I) fine particles dominated, (II) well mixed, and (III) coarse particles dominated. As listed in Table 4.2 and illustrated in Figure 4.1, fine-mode fractions in terms of volume (fmf_V) are defined as 0.8, 0.5, and 0.2 for these three types, respectively. Aerosol volumes are scaled as necessary to maintain a normalized AOD at 440 nm corresponding to a moderate hazy condition ($\tau_{440} = 1.0$). The spectral aerosol optical depths τ_A , single scattering albedo ω_A , and the Ångström exponent (AE) are calculated and also shown in Table 4.2.

4.2.2 Synthetic observations

As described in section 1.1.2 and Table 1.1, The SunPhotometer equipped at AERONET sites routinely measures direct and diffuse (sky) solar radiances and optionally the mono-band light polarization [Holben et al., 1998]. Recently, multi-spectral polarizations have also been taken with a newer-generation SunPhotometer (CIMEL CE318-DP) at some sites [Li et al., 2009] and the UAE² fields campaign Reid et al. [2008]. Here we focus our study

Table 4.3: List of scenarios of AERONET observations used for information content analysis.

| Scenario | Observations included ^a | Remark |
|----------|---|---|
| I1 | τ_A , and I_{alm} | Observations used in Dubovik00&06 algorithm |
| I2 | τ_A , I_{alm} , and I_{pp} | Scenario I1 plus principal-plane radiances |
| P1 | τ_A , I_{alm} , I_{pp} and $DOLP_{pp}$ | Scenario I2 plus principal-plane polarization |
| P2 | τ_A , I_{alm} , and $DOLP_{alm}$ | Scenario I1 plus almucantar polarization |

^aVariables are for four spectral wavelengths, i.e., 440, 675, 870, and 1020 nm.

on using multi-spectral polarizations for the inversion of aerosol parameters.

In order to investigate the merit of combining various observations in the inversion, we define four different scenarios of observation vectors, i.e., I1, I2, P1, and P2 as summarized in the Table 1. The observation vector in scenario I1 comprises direct sun AODs and solar almucantar radiances (I_{alm}) at 440, 675, 870, and 1020 nm. Scenario I2 includes measurements in scenario A and the total radiances (I_{pp}) at the same four wavelengths observed in the solar principal-plane. Observations in scenario P1 are defined to further include $DOLP_{pp}$ at those four wavelengths. Lastly, scenario P2 observations comprise basic measurements in scenario I1 plus almucantar polarization ($DOLP_{alm}$) at the same wavelengths. The $DOLP_{alm}$ is not routinely measured by any current SunPhotometer, but we include it for a comparative analysis. Measurements defined in scenario I1 represent observations used by the current AERONET operational inversion and thus serves as a control experiment. From scenario I2, we can investigate the synergy of radiances in both the solar almucantar and solar principal-plane. Scans in the solar principal-plane can achieve larger scattering angles and thus may contain additional scattering information. And with scenarios P1 and P2 we will be able to evaluate the potential of adding polarization in the inversion.

We exclude I_{ppl} (Table 1.1) in our analysis because sky radiance in the solar principal plane can also be obtained during the polarization scan (I_{pp}). I_{ppl} and I_{pp} are different in the viewing-angle sequences, but they generally share a similar range of scattering angles. Thus,

one is redundant with the other. We also exclude analysis of monochromatic polarization (at 870 nm), currently measured on many AERONET sites, because single-band polarization measurements contain much less information than multi-band ones and newer generation SunPhotometers with multi-band polarization capacity will be deployed at more AERONET sites.

While not as important as that for estimating the upwelling shortwave radiances, accurately characterizing the surface reflectance and depolarization can minimize the possible error in the simulation of down-welling radiation. For total reflectance, we parameterize the surface BRDF using the reciprocal-Ross-Li kernels expressed in equation (2.13), which are applied in MODIS surface retrieval products [[Wanner et al., 1995](#); [Lucht et al., 2000](#)]. These three kernels represent scatterings respectively from a Lambertian surface, a surface within a dense vegetation canopy, and a surface with larger gaps between objects accounting for self-shadowing. Amplitude factors for these kernels at AERONET bands are chosen from MODIS products to represent Beijing site during February 2011. We also use a BPDF model (equation (2.14)) introduced by [Maignan et al. \[2009\]](#) for the angular polarized radiance, which was based on the Fresnel coefficients of light reflectance from the surface and fitted to the POLDER (POLarization and Directionality of the Earth's Reflectances) observations. Although parameters involving surface reflectance are not included in the state vector for the retrieval, they can significantly affect the radiance simulation. We must consider the inaccuracy of surface reflectance for the forward model error with the approach of equation (3.2). We assume that the amplitude factor for each BRDF kernel have 20% uncertainty. But we ignore the error in the BPDF because BPDF of land surface is usually spectrally invariant and tends to have rather small values [[Nadal and Breon, 1999](#); [Maignan et al., 2009](#)].

4.3 Results

Following the approach stated in section 3.2, we have simulated the AERONET photopolarimetric measurements under various solar zenith angles from 40° to 75° for the three defined aerosol types (Table 4.2). The simulated radiances (I_{alm}) on the solar almucantar plane and the degree of linear polarization (DOLP_{pp}) on the solar principal plane are illustrated in Figure 4.2 for aerosols of type II with solar zenith angle of 55° . These simulations for other aerosol types and other solar zenith angles are of similar pattern. According to Figure 4.2a, I_{alm} decreases as the scattering angle increases, resulting from forward-dominated scattering phase function of aerosol particles. The maximum DOLP_{pp} takes place at the scattering angle of 90° as a result of composite effect of Rayleigh and aerosol scattering, while the smaller DOLP_{pp} values dominates at the small scattering angles because of the predominance of diffracted light (Figure 4.2b). With the synthetic data and relevant error characterizations, we have computed the error-normalized (EN) Jacobian matrix, DFS, and a posteriori error to evaluate the capacity of AERONET measurements in inferring aerosol microphysical properties. Our analysis mainly focuses on the comparison of those quantities between measurements with and without including polarization, so that we can understand the importance of adding polarization for the retrieval.

4.3.1 Error-normalized (EN) Jacobian matrix

We compare the EN Jacobians for the I_{alm} and DOLP_{pp} in both Figure 4.3 and Figure 4.4 to explore the importance of DOLP_{pp} measurements to the retrieval. Distinct patterns of EN Jacobians can be found between the DOLP_{pp} and I_{alm} over the scattering angle. As shown in Figures 4.3a and 4.4a, the radiance at scattering angles less than $\sim 10^\circ$ decreases with increasing fine-mode aerosol loading (e.g. negative $\partial I_{\text{alm}} / \partial V_0$) and increases with

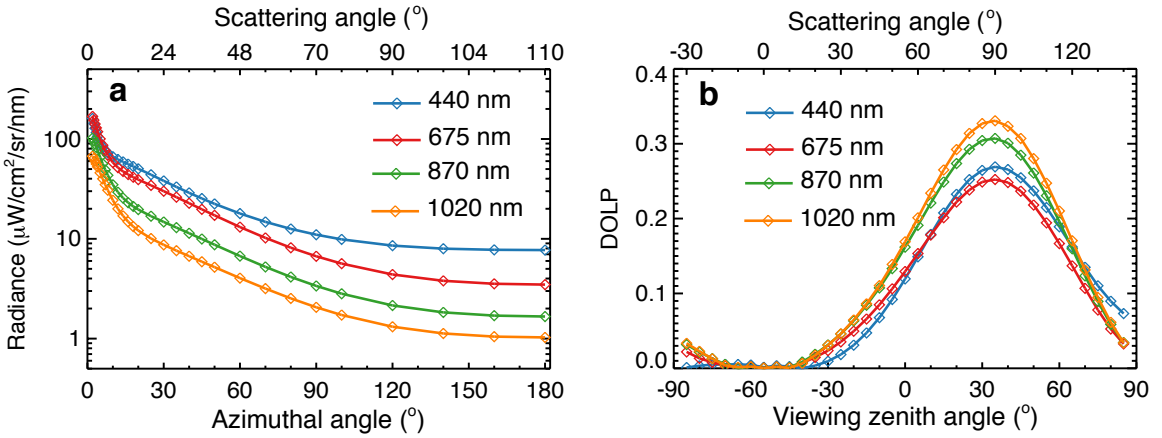


Figure 4.2: (a) Simulated radiances in the solar almucantar plane as a function of azimuth angle. (b) Simulated degree of linear polarization (DOLP) in the solar principal plane as a function of view zenith angle. Simulations are for the well-mixed aerosol type with columnar AOD of 1.0 at 440 nm as shown in the Table 4.2. Solar zenith angle is 55° and top abscissas show corresponding scattering angles.

increasing coarse-mode aerosol loading (e.g. positive $\partial I_{\text{alm}} / \partial V_0$), whereas the sensitivity of the I_{alm} to V_0 at larger scattering angles is more positive in the fine mode and less positive in the coarse mode. This occurs because large particles scatter more radiation than small particles at near-forward scattering angles [van de Hulst, 1981]. In contrast, the $DOLP_{\text{pp}}$ presents profound sensitivity to the V_0 of aerosol in both modes at the scattering angles between 45° and 135° (Figures 4.3f and 4.4f).

Furthermore, the EN Jacobians of I_{alm} and $DOLP_{\text{pp}}$ are also complimentary in terms of their variations on the spectral wavelength. For example, the EN Jacobians for I_{alm} with respect to the fine-mode V_0 express lowest at 440 nm (blue curve in Figure 4.3a), but those for $DOLP_{\text{pp}}$ at 440 nm (blue curve in Figure 4.3f) are largest ones among these four spectral bands. Indeed, variations of these sensitivities with wavelength are mainly determined by the change of size parameter η , which defined as the ratio of the particle size to the applied spectral wavelength, $\eta = 2\pi r_{\text{eff}} / \lambda$. The $DOLP_{\text{pp}}$ in scattering angles near 90° approaches unity under pure Rayleigh scattering regime where $\eta \ll 1$. When the η increases, the value

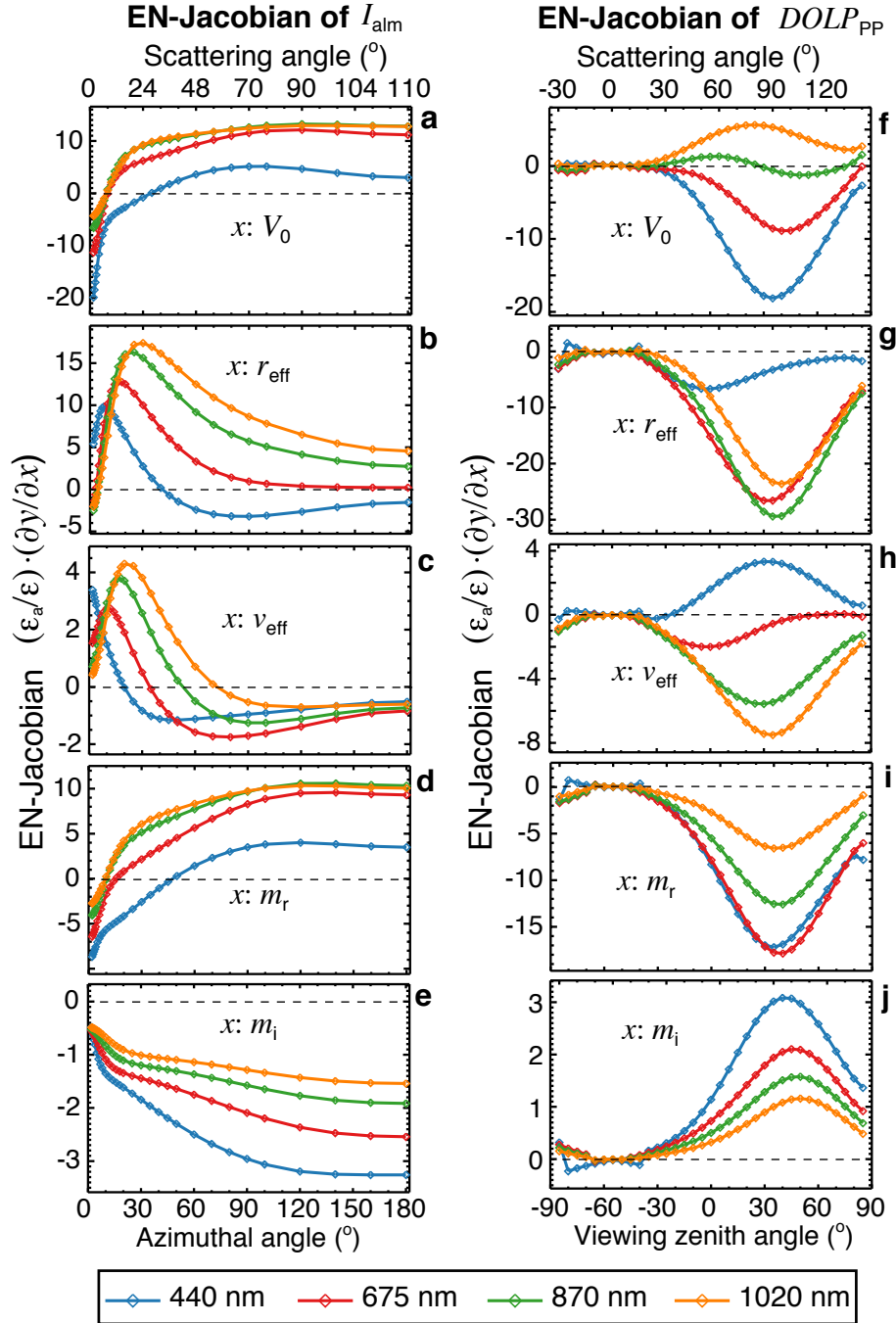


Figure 4.3: Error-normalized Jacobians of almucantar radiances I_{alm} (left column) and degree of linear polarization $DOLP_{\text{pp}}$ (right column) with respect to retrieved aerosol parameters in the *fine* mode: (a, f) V_0 , (b, g) r_{eff} , (c, h) v_{eff} , (d, i) m_r , and (e, j) m_i . Simulations use type-II aerosols with columnar AOD of 1.0 at 440 nm and solar zenith angle of 55° . The top and bottom abscissas are respectively the scattering angle and SunPhotometer scanning geometries.

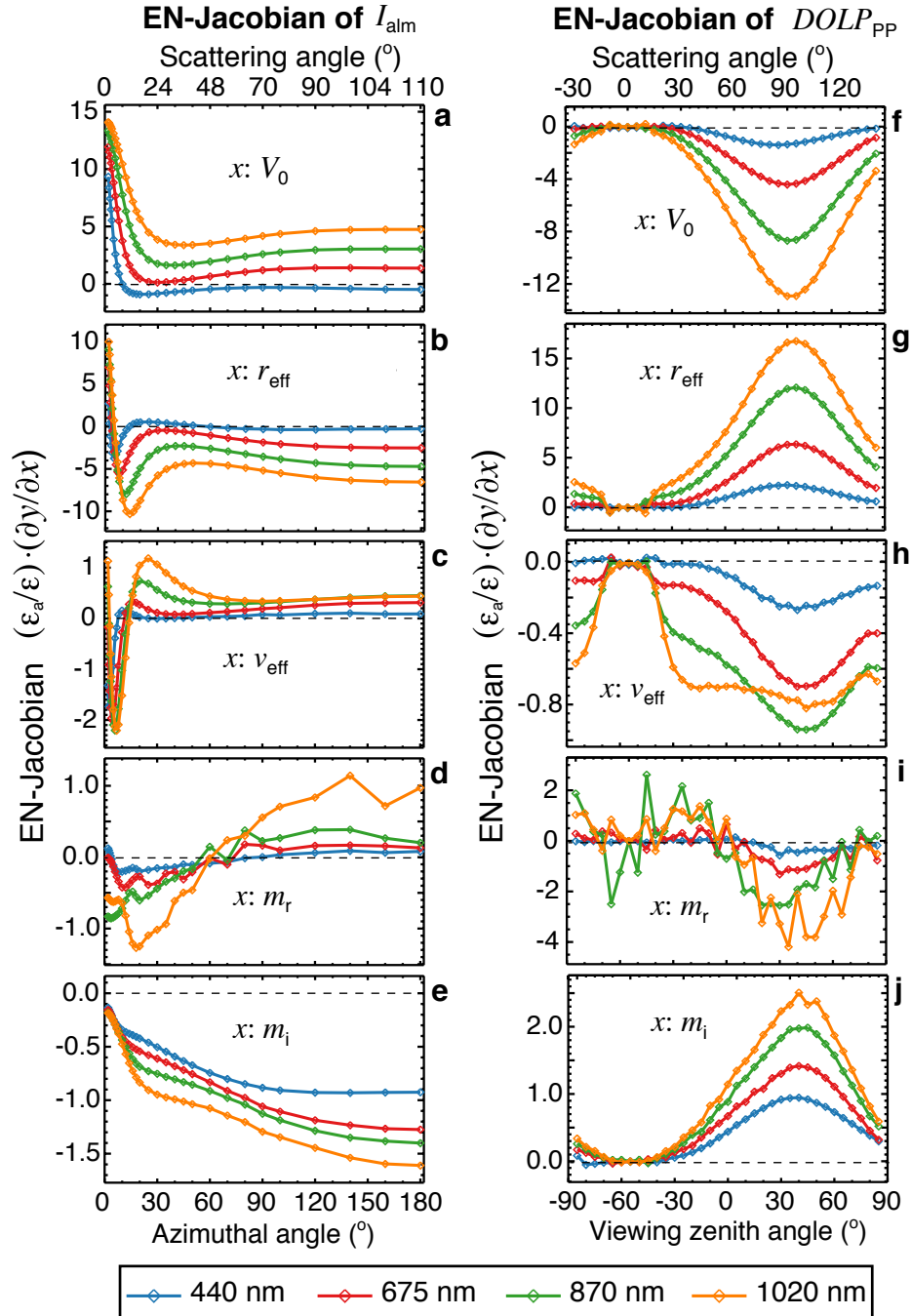


Figure 4.4: Same as Figure 4.3 but for parameters of aerosol in the *coarse* mode.

of $\partial \text{DOLP}_{\text{pp}} / \partial V_0$ decreases and transits into negative at $\eta \sim 2$, reaches negative maxima at $\eta \sim 10$, then increases and slowly transits back to positive when η is as large as ~ 40 [Hansen and Travis, 1974]. The magnitude of the η at these four bands ranges from 3.0 to 1.3 for the fine-mode particles and from 27 to 11 for the coarse-mode particles. Therefore we can understand that: (i) the sensitivity of DOLP_{pp} to the fine-mode V_0 is positive at 1020 nm due to the small size parameter $\eta = 1.3$ (orange curve in Figure 4.3f); (ii) this sensitivity gets weaker at 675 nm to 870 nm and transits to negative at 440 nm as η increases (Figure 4.3f); and (iii) this sensitivity for aerosol in the coarse mode is more negative for longer wavelengths that are corresponding to smaller values of η .

We also note that sensitivity of the I_{alm} to PSD parameters dominates for scattering angles less than $\sim 40^\circ$ (Figures 4.3b-c and 4.4b-c), while its sensitivity to m_r and m_i prevails at larger scattering angles (Figures 4.3d-e and 4.4d-e). In the near-forward scattering angular regions, the dominant scattering effect is the diffraction of light, which essentially depends on the size of particles and is independent of the index of refraction [van de Hulst, 1981; Hansen and Travis, 1974]. The DOLP_{pp} , in contrast, is sensitive to both the aerosol size and the refractive index at scattering angles from 45° to 135° (right columns of the Figures 4.3 and 4.4). Variations of the sensitivity among spectral bands can be explained by the wavelength-dependent size parameters as discussed in the above paragraph.

Overall, the DOLP_{pp} EN Jacobians have similar or larger magnitudes to those of I_{alm} , indicating that the DOLP_{pp} measurements possess equal or larger information for the inversion of these aerosol properties. Adding such complementary DOLP_{pp} measurements to the current radiance-only inversion can potentially increase the retrieval accuracy. The magnitude of EN Jacobian elements varies among retrieved parameters, which leads to the variability of retrieval accuracy. The EN Jacobians with respect to the V_0 and r_{eff} of both modes and the fine-mode v_{eff} and refractive index are larger than those of other parameters. Correspondingly, these parameters are expected to achieve higher accuracy in the retrieval.

While the maxima in EN Jacobians of I_{alm} with respect to the coarse-mode refractive index at 870 and 1020 nm slightly exceed unity (Figure 4.4d-e), larger counterparts for DOLP_{pp} (Figure 4.4i-j) will likely result in improved retrievals. In contrast, magnitudes of EN Jacobian for both I_{alm} and DOLP_{pp} with respect to coarse-mode refractive index at 440 and 675 nm are smaller than unity across the whole angular range. Adding polarization may not improve the retrieval for coarse-mode refractive index at those shorter wavelengths in such aerosol scenario. However, the consideration of spectral dependence of refractive index by using the smoothness constraints will potentially resolve this problem [Dubovik, 2004].

4.3.2 Information content and retrieval error

We calculated the averaging kernel matrix \mathbf{A} , DFS, and *a posteriori* error for retrieved parameters from these four scenarios of observation defined in Table 4.3. Figures 4.5a-c illustrate how the DFS varies with the solar zenith angles for three defined aerosol types. The DFS in the scenario I2 (red curves) ranges from 14 to 15 for the fine-dominated aerosol model, and from 17 to 19 for other two aerosol models, about 2–3 degrees higher than those using AODs and I_{alm} measurements in the scenario I1 (black curves), indicating that sky radiances in the principal plane (I_{pp}) contain additional information. The scenario P1 (green curves), which comprises solar almucantar sky radiances and principal-plane polarimetric radiances at four wavelengths, further increases DFS by 1–2. Observations in the scenario P2 (blue curves)—radiances and polarization in the almucantar plane—yields DFS values slightly below those in the scenarios I2 and P1. Therefore, from Figure 4.5 we conclude that adding measurements in the solar principal plane into the inversion significantly increases the information content for aerosol properties, especially when combining the I_{pp} and DOLP_{pp} . We also note that the DFS increases with solar zenith angle for all cases. Observations in larger solar zenith angle enable a wider range of scattering angles (Figure 4.5d), and thus

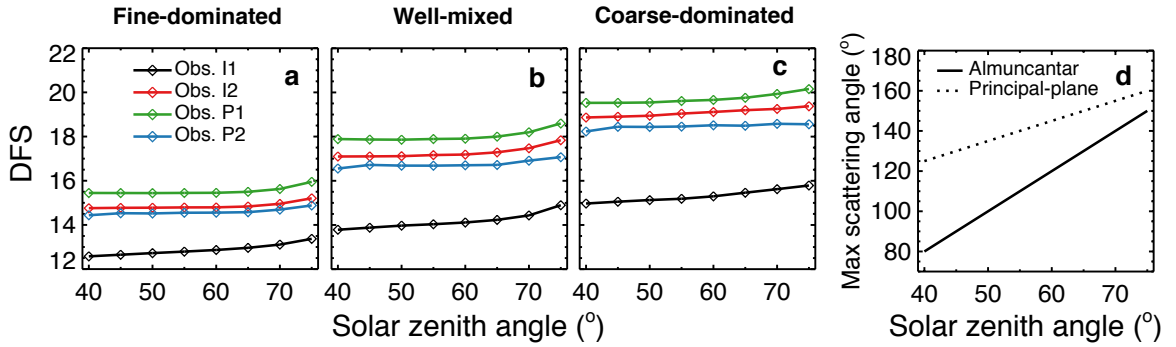


Figure 4.5: Degree of freedom for signal (DFS) as a function of solar zenith angle for retrieving all 22 parameters when using aerosol type of (a) fine-dominated, (b) well-mixed, and (c) coarse-dominated. Four differently colored-curves denote four observation scenarios defined in Table 1. Panel (d) shows the maximum scattering angles that can be reached by the almucantar and the principal-plane scans.

contain more information on the aerosol scattering phase function and in turn on the aerosol microphysical parameters.

We illustrate the DFS components $A_{i,i}$ in Figure 4.6 for the V_0 , r_{eff} and v_{eff} , and in Figure 4.7 and 4.8 for the m_r and m_i , respectively. Also shown in those figures are the a posteriori errors, which are the diagonal elements of $\hat{\mathbf{S}}^{\frac{1}{2}}$. It should be noted that errors for V_0 , r_{eff} , and v_{eff} are in terms of relative uncertainties (%), while errors in the m_r and m_i are absolute quantities. Curves of four different colors in each panel indicate these defined four observation scenarios and are averages for the three aerosol types. Error bars represent one fifth of the standard deviations among the three aerosol types (the use of the one-fifth scale is only for plotting purpose). These error bars thus depict the variability of the DFS component and retrieval error over the fine-mode fraction (fmf_v). Mean retrieval uncertainties averaged over various solar zenith angles are summarized in Table 4.4. We discuss these results for each retrieved parameter in detail as following.

4.3.2.1 Aerosol PSD

Among the 22 elements in the state vector, the V_0 , r_{eff} and v_{eff} describe the aerosol PSD. According to Figure 4.6a-c, observations in the scenario P1 (green curves) always yield the highest DFS components for inferring PSD parameters in both the fine and coarse modes, followed by observations from the scenarios I2 (red) and P2 (blue), and lastly the scenario I1 (black). As a consequence, the *a posterior* errors are found smallest for the scenario P1 and largest for the scenario I1 (Figure 4.6d-e). Retrieval errors in the scenario I1 (black curves) are 5–15% for V_0 , 5–9% for r_{eff} , and 20–30% for v_{eff} , which vary with solar zenith angles. In contrast, retrieval errors in the scenario P1 (green curves) are reduced to ∼2.5%(3%), 1%(3.5%), and 7%(20%) for the fine (coarse) mode. From observations in the scenarios P2 and I2, one can retrieve V_0 , r_{eff} , and v_{eff} of errors lying between the scenarios I1 and P1, though slightly larger in the scenario P2. In addition, higher DFS components and smaller retrieval errors are found for the fine-mode parameters than those for the coarse mode, because radiances and polarization are in particular more sensitive to aerosol parameters in the fine mode as shown in the contrast between the Figures 4.3 and 4.4.

We also note that, in the scenario I1, DFS components for the coarse-mode parameters decrease with increasing solar zenith angle, while no obvious trend can be found for the fine-mode parameters. This can be explained by the low sensitivity of the I_{alm} to the coarse-mode V_0 , r_{eff} , and v_{eff} at large scattering angles as showed in Figure 4.4a-c. Higher sensitivities occur at scattering angles below ∼30°; the increase in SZA results in a smaller number of measurements in the near-forward scattering angular regions, and thus leads to larger retrieval errors. However, these trends turn to be weaker or negligible in other observation scenarios, especially the scenario P1. We can understand this from two aspects. First, observations from principal plane can add additional measurements near the forward scattering region. Second and most importantly, the added polarization measurements in

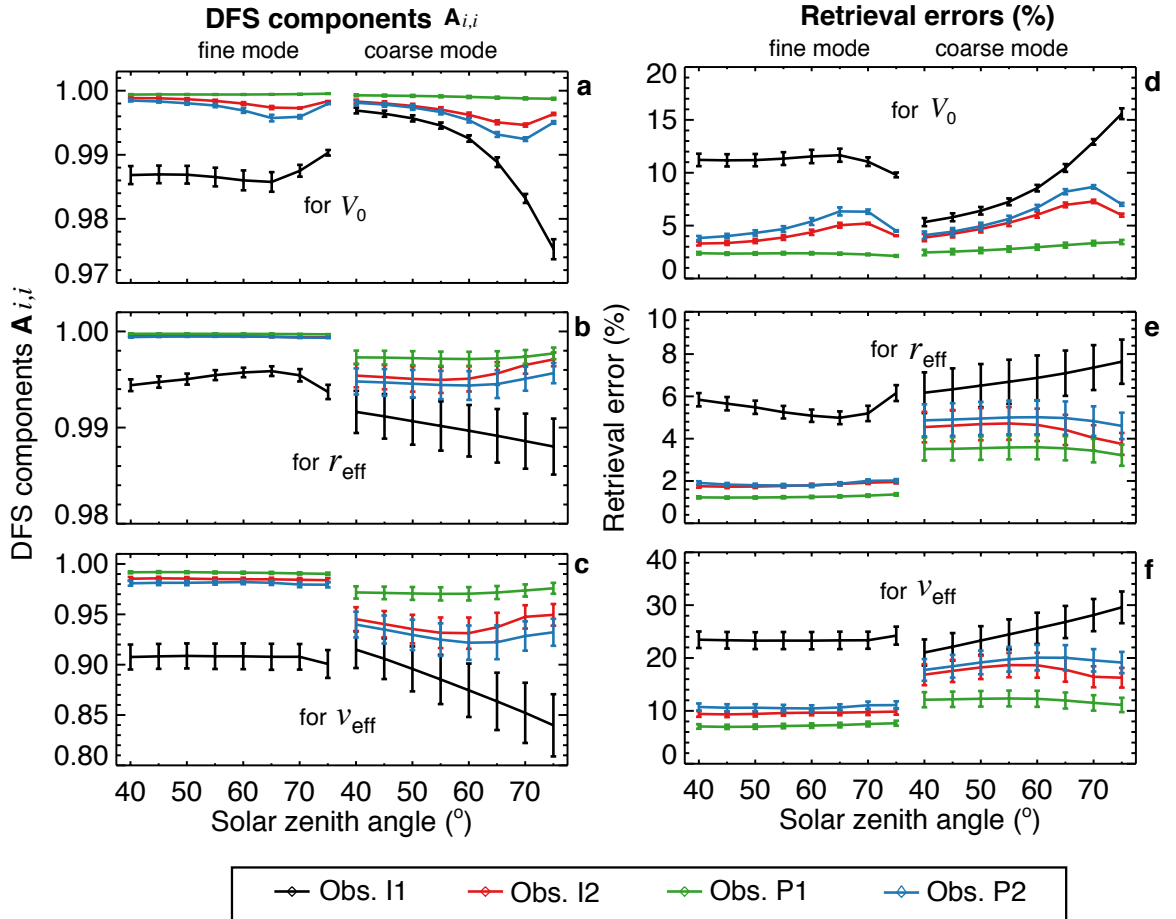


Figure 4.6: DFS components (left column) and retrieval uncertainty (right column) as a function solar zenith angle with different observation scenarios defined in Table 4.3. Quantities are averages for three aerosol types defined in Table 4.2, and error bars represent one fifth of standard deviation. Three rows from top to bottom are respectively for retrieving V_0 , r_{eff} , and ν_{eff} . In each panel, shown in the left is for the fine mode and in the right is for the coarse mode.

the scenarios P1 and P2 contain additional information that is independent of the scattering angle limitation as discussed in the section 4.3.1.

Overall, the increase in DFS components by adding polarization measurements is less than 0.1 for retrieving V_0 , r_{eff} , and ν_{eff} , because radiances alone contain abundant information. The retrieval accuracy in aerosol PSD from observations of all scenarios exceeds the requirements for better quantifying aerosol climate radiative forcing identified

by *Mishchenko et al.* [2004]. Even so, the addition of multi-band DOLP_{pp} measurements to the inversion can still yield up to $\sim 70\%$ retrieval error reduction in the fine-mode and up to $\sim 50\%$ reduction in the coarse-mode aerosol PSD parameters.

4.3.2.2 Refractive indices

As shown in Figure 4.7a-b, different magnitudes prevail in the DFS components for the m_r between fine and coarse modes and among different observation scenarios. For example, DFS components for aerosols in the fine mode exceed 0.8 at all four wavelengths in the scenario I1; while the counterparts in the coarse mode approach 0.5 at 1020 nm and are less than 0.2 for the other three wavelengths. This is due to the weaker sensitivity of almucantar radiances to the coarse-mode m_r (as in Figure 4.4d) comparing to that for aerosol in the fine mode (as in Figure 4.3d). In general, adding the DOLP_{alm}, I_{pp} , or both the I_{pp} and DOLP_{pp} in the inversion increases the DFS components for m_r of aerosols in both the fine and the coarse modes. Particularly, DFS components achieve the most significant rise in the scenario P1 by climbing to 0.95–1.0 in the fine mode and to 0.4–0.8 in the coarse mode. Also shown in Figure 4.7a, an increasing pattern with solar zenith angles is found in the DFS components for the fine-mode aerosol at larger wavelengths because stronger sensitivity occurs in larger scattering angles.

As expected, the retrieval of m_r can be more accurate by adding additional measurements. According to Figure 4.7c-d, the *a posteriori* error in m_r averaged on the four spectral bands is ~ 0.015 (0.065) for aerosols in the fine (coarse) mode from measurements in the scenario I1. In contrast, it is reduced to 0.008 (0.037), 0.005 (0.035), and 0.009 (0.040) in the scenarios I2, P1, and P2, respectively. Retrieval errors in the coarse-mode m_r are larger in shorter spectral wavelengths because of weaker sensitivity to the I_{alm} and DOLP. For instance of the scenario P1, it is about 0.06 at 440 nm, 0.035 at 675 nm, and 0.02 at 870 and 1020 nm.

The DFS components for the m_i are shown in Figure 4.8a–b, and the corresponding

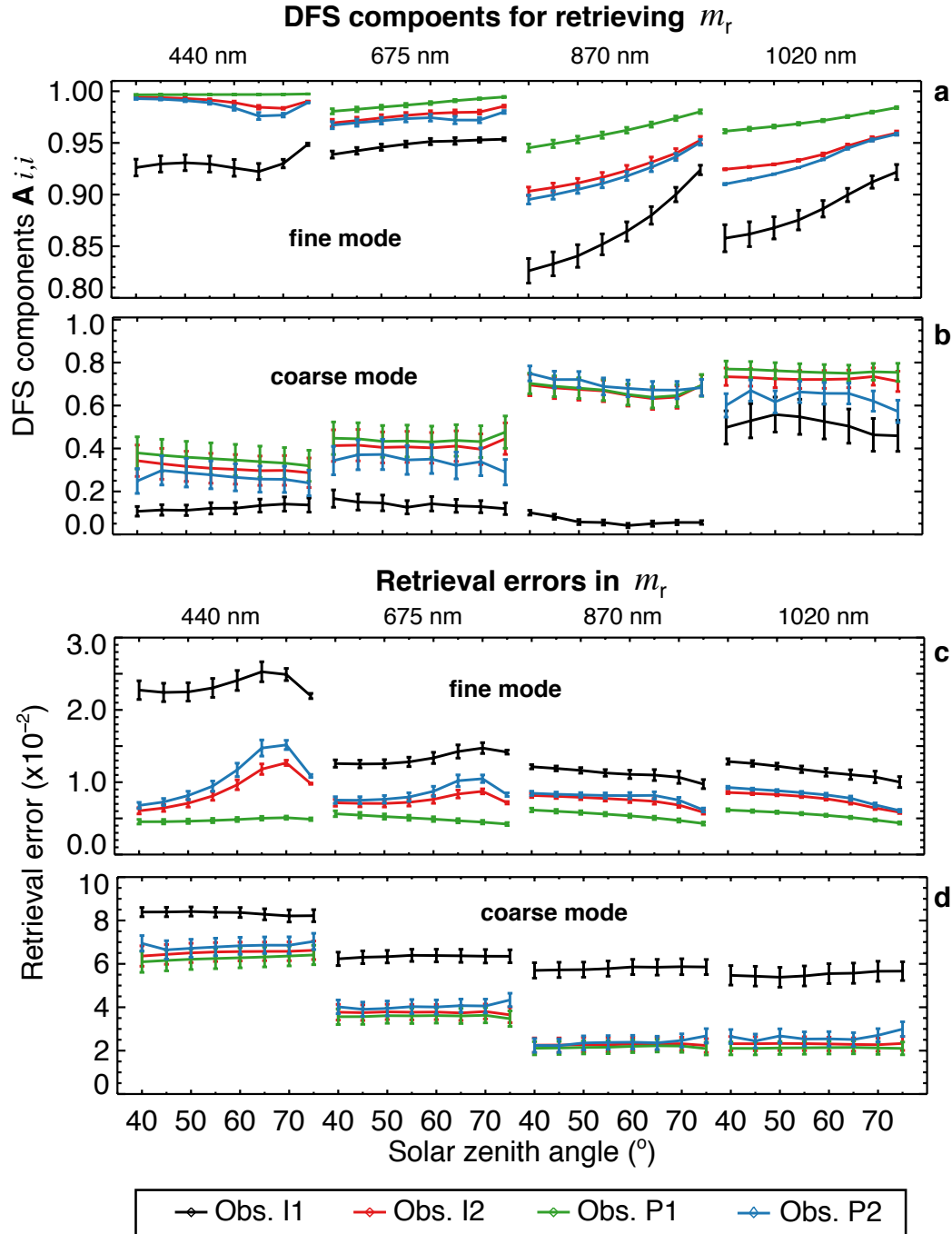


Figure 4.7: Same as Figure 4.6 but for DFS components (a-b) and retrieval uncertainty (c-d) for retrieving real part refractive index m_{real} in four wavelength bands. (a) and (c) are for the fine aerosol mode, while (b) and (d) for the coarse mode.

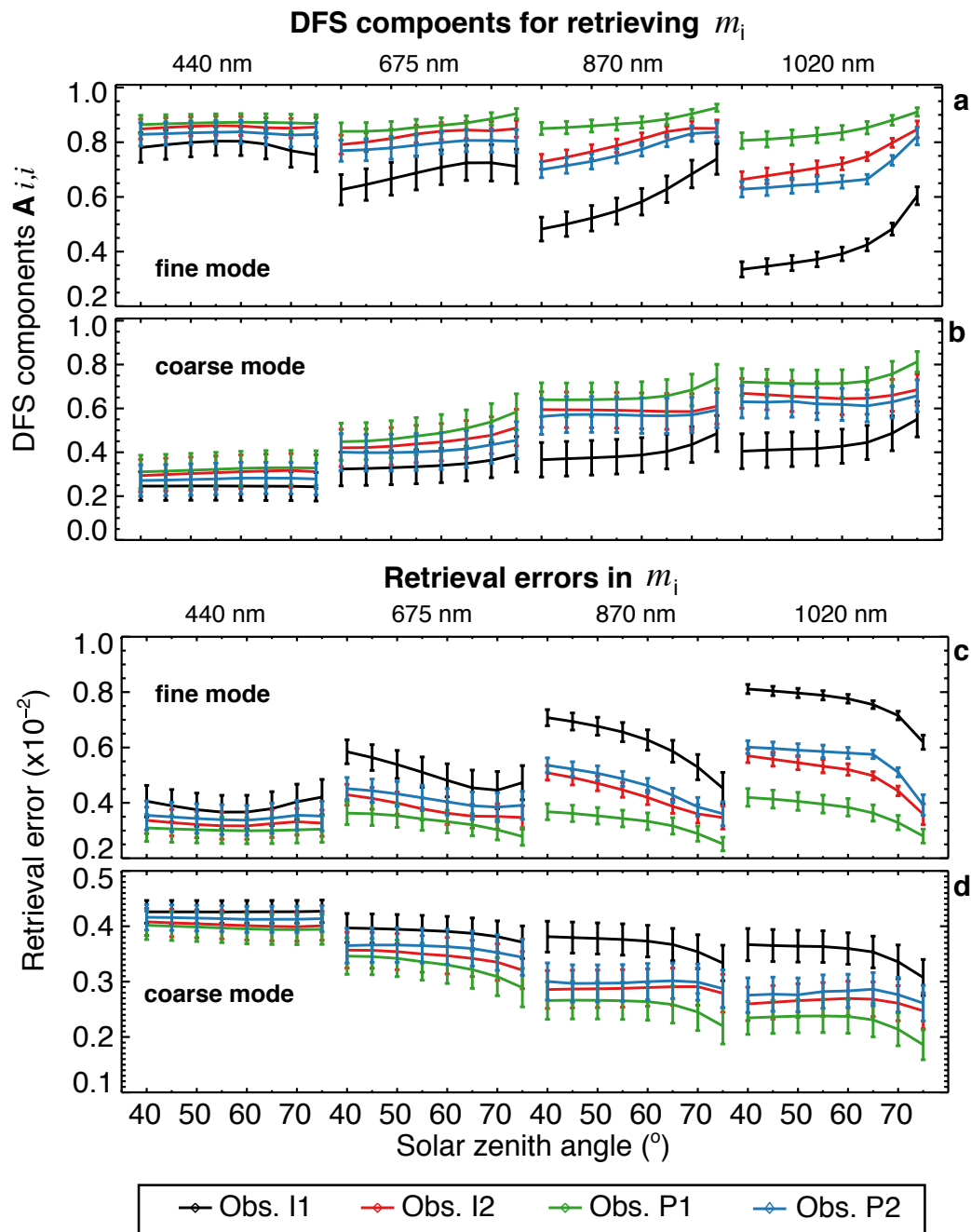


Figure 4.8: Same as Figure 4.7 but for retrieving imaginary part refractive index m_i .

Table 4.4: Error for retrieved and derived parameters among *a priori*, *a posteriori*, and Glory characterization^a.

| Entries | Error in retrieved parameters | | | | | |
|--------------------|-------------------------------|----------------------|----------------------|-----------|-------------|------------|
| | V_0 (%) | r_{eff} (%) | v_{eff} (%) | m_r | m_i | ω_A |
| A priori | 100/100 | 80/80 | 80/80 | .15/.15 | .01/.05 | - |
| Obs. I1 | 11./9.0 | 5.5/6.8 | 23/25 | .015/.065 | .0057/.0038 | .037/.085 |
| Obs. I2 | 4.1/5.5 | 1.8/4.4 | 10/18 | .008/.037 | .0041/.0032 | .024/.073 |
| Obs. P1 | 2.3/2.9 | 1.3/3.5 | 7.2/12 | .005/.035 | .0033/.0030 | .019/.068 |
| Obs. P2 | 4.9/6.2 | 1.9/4.9 | 11/19 | .009/.040 | .0044/.0034 | .026/.076 |
| Glory ^b | - | 10 | 40 | .02 | - | .03 |

^aResults of our work are averaged values for three aerosol types and for solar zenith angles from 40° to 70°.

^bReferred to [Mishchenko et al. \[2004\]](#).

retrieval errors in m_i are displayed in Figure 4.8c–d. Similar to those for the m_i , DFS components for retrieving the m_i are larger in the fine mode and show an increasing pattern with the solar zenith angle. Observations in the scenario P1 always yield largest DFS components and smallest retrieval error for the m_i , followed by the scenarios P2 and I2. Observations in the scenario I1 offer the m_i retrieval with largest error. If averaged on the solar zenith angles and aerosol types, the retrieval error in the m_i is 0.006 (0.004) for aerosol in the fine (coarse) mode in the scenario I1, and can be reduced to 0.003 (0.003) in the scenario P1.

4.3.2.3 Single scattering albedo

Note that the aerosol single scattering albedo ω_A is an intermediate rather than a directly retrieved parameter. The error in ω_A can be estimated from $\hat{\mathbf{S}}$ with equation (3.9). The ω_A for each aerosol mode uniquely depends on the light wavelength and aerosol microphysical parameters including r_{eff} , v_{eff} , and m_r and m_i , although the m_i impacts ω_A most significantly [[Hansen and Travis, 1974](#)]. Required derivatives of ω_A to these parameters in the equation (3.9) can be obtained from the linearized Mie code (section 2.2.2) integrated into the UNL-

VRTM. We calculated uncertainties in the ω_A for each wavelength and each aerosol type, and the averaged values are summarized in Table 4.4. Observations in these four scenarios can retrieve ω_A with the uncertainty of 0.037, 0.024, 0.019, and 0.026 for the fine mode, and 0.085, 0.073, 0.068, and 0.076 for the coarse mode, respectively. Thus, only the fine-mode ω_A retrieval with polarization involved can meet the accuracy requirements (0.03) for accurate climate forcing estimates [[Mishchenko et al., 2004](#)]. We noted that the mean uncertainty in the coarse-mode ω_A exceeds 0.06 in all of these four scenarios, but higher accuracy may be achieved under coarse-dominated conditions as shown in the following section.

4.4 Sensitivity of Retrieval Error to AOD and f_{mf_v}

The performance of retrieval usually varies with aerosol conditions like the aerosol loading and the prevalence of aerosol in either the fine or the coarse modes (e.g., fine-mode volume fraction, f_{mf_v}). As a result, uncertainties in aerosol retrievals can depend much more strongly on the AOD than they do on the properties of an individual aerosol model [[Knobelspiesse et al., 2012](#)]. For the same reason, the inversion of refractive indices and ω_A in the current AERONET algorithm is confined to the condition when the 440-nm AOD is larger than 0.4 [[Dubovik et al., 2000](#); [Holben et al., 2006](#)]. Our analysis above, which focused on three aerosol types by a constant AOD value at 440 nm ($\tau_{A440}=1.0$), is insufficient to represent variable global conditions. At the same time, we also found noticeable variability of the DFS components and a posteriori errors existing among three aerosol types with different f_{mf_v} , especially for the coarse-mode parameters. Thus, it is necessary to investigate how aerosol conditions affect the retrieval error, in order to answer the question: under what aerosol conditions are the AERONET measurements (with and without polarization) capable of yielding retrievals with sufficient accuracy?

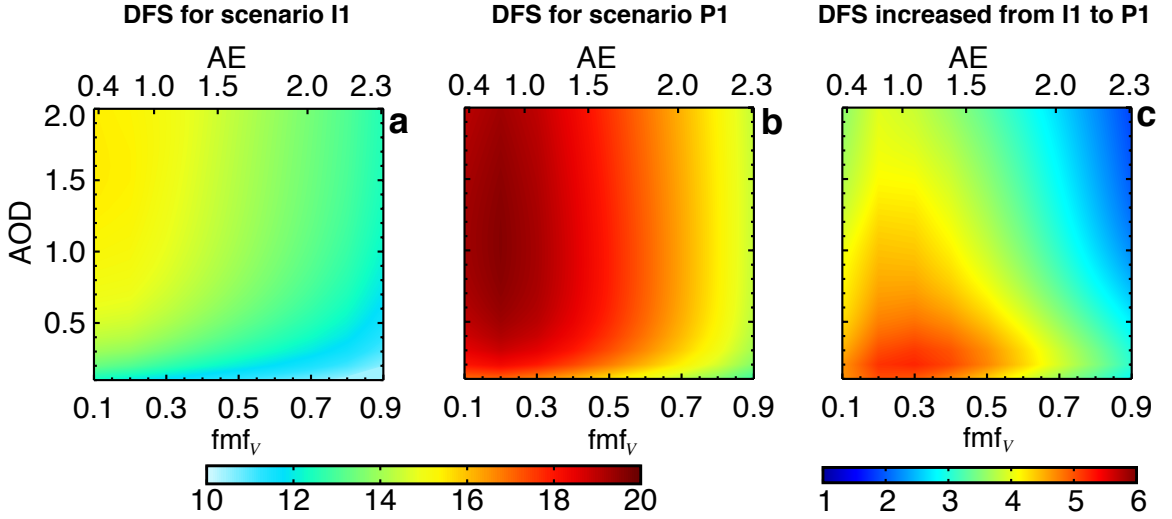


Figure 4.9: Contours of DFS as a function of fmf_v and AOD in scenarios I1 (a) and P1 (b). (c) the difference of DFS between (a) and (b). Simulations are for solar zenith angle of 55° . The top abscissa denotes Ångström exponent (AE).

We expand our analysis for the τ_{A440} ranging from 0.1 to 2.0 and for the fmf_v from 0.1 to 0.9. In practice, the fmf_v is inaccessible prior to inversion. Instead, we use the Ångström exponent (AE) from 870 to 1020 nm together with τ_{A440} to define the aerosol conditions, because the AE in the longer paired wavelength is highly related to the fmf_v [Schuster et al., 2006] and immediately available from the AERONET direct sun measurements. With the aerosol properties defined in the Table 4.3, the fmf_v from 0.1 to 0.9 gives AE values from 0.35 to 2.3. We exclude the scenarios of I2 and P2 in our following analysis, because the scenario P1 demonstrates the most superior performance and is also the focus of our algorithm development.

Figure 4.9a–b display the contours of DFS as a function of the AE (or fmf_v) and τ_{A440} in the scenarios I1 and P1, respectively. We found that the DFS decreases with an increasing AE and fmf_v for the same AOD. This is attributed to the fact that the coarse-mode parameters are more difficult to retrieve than their fine-mode counterparts, restrained by their weaker sensitivities to the I_{alm} and the DOLP_{pp} . Thus, the decrease in the coarse-mode fraction

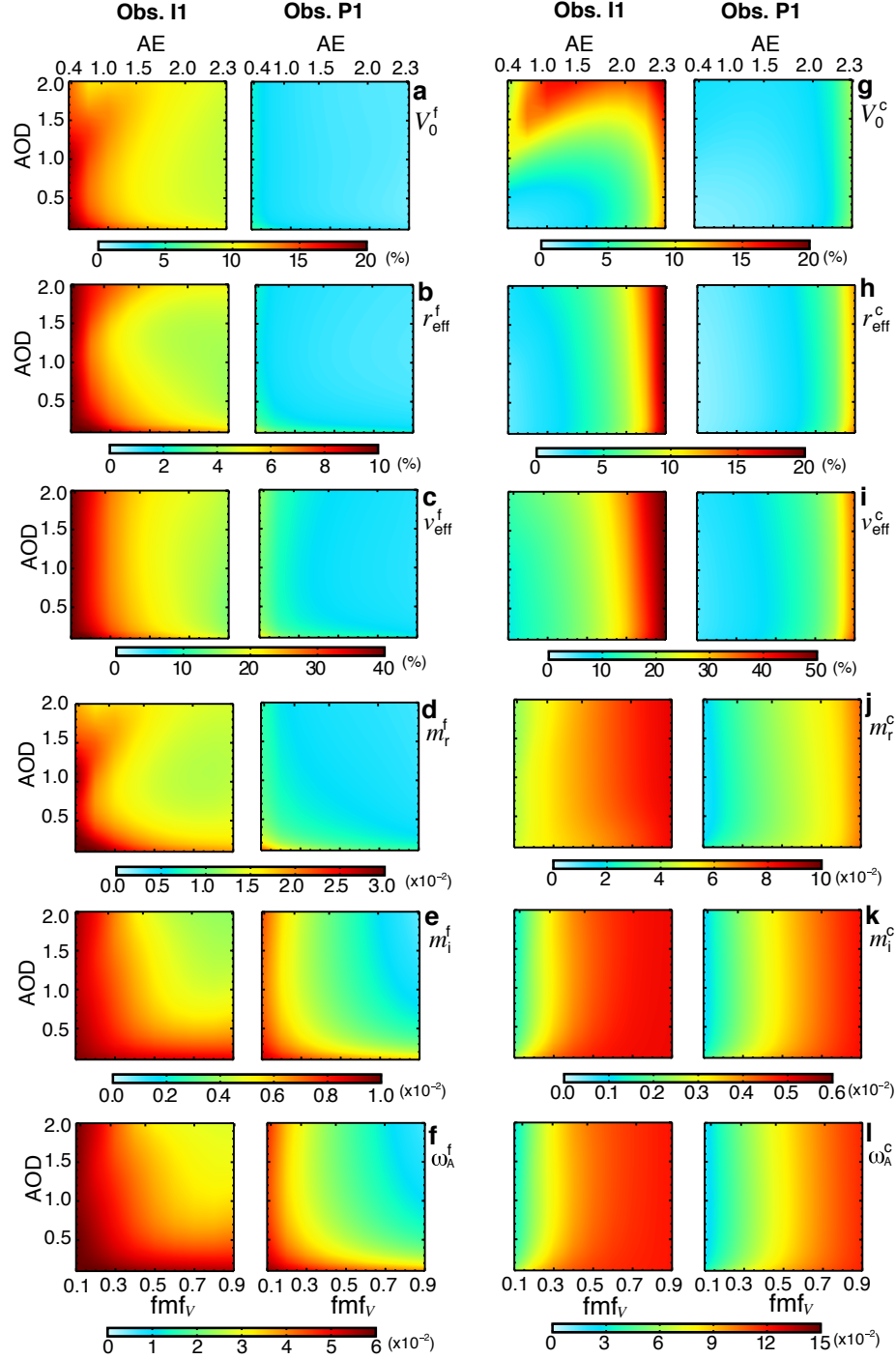


Figure 4.10: Retrieval uncertainties as a function of fmfv (or AE) and AOD for each individual aerosol parameters (V_0 , r_{eff} , v_{eff} , m_r , m_i , and ω_A) in the both *fine* (a-f)and *coarse* (g-l) modes. Two sub-panels in each panel indicate observations in the scenarios I1 and P1, respectively. Simulations are for solar zenith angle of 55° . The x- and y-axis are identical to those in Figure 4.9. Relative uncertainties are shown for V_0 , r_{eff} and v_{eff} , while absolute errors for m_r , m_i , and ω_A . Retrieval errors for m_r , m_i , and ω_A are averaged values over the four spectral bands.

significantly reduces the aerosol information for coarse-mode parameters but retains the information for fine-mode parameters, resulting in decreases in the total DFS. We also notice from Figure 4.9a that the DFS increases with an increasing AOD in the scenario I1. However, AOD change has less impact in the scenario P1 (Figure 4.9b). For example, the DFS values are lower than 14 when $\text{AOD} < 0.4$ in the scenario I1, whereas even larger DFS can be found in the scenario P1 when $\text{AOD} < 0.2$. Therefore, we may expect that the inversion in the scenario P1 will be capable to retrieve aerosol parameters in conditions of lower aerosol loading, and may bring down the $\tau_{\text{A}440}$ threshold of 0.4 from the current AERONET inversion algorithm to retrieve the refractive index and ω_A . Finally, as indicated in Figure 4.9c, the addition of I_{pp} and DOLP_{pp} in the inversion can add 2–5 pieces of useful information. Such improvement occurs in all aerosol conditions but is more dominated when enough coarse particles are present: $\text{fmf}_v < 0.5$ (or $\text{AE} < 1.6$), in which the radiance-only inversion usually yields a large retrieval error for the fine-mode aerosol.

In Figure 4.10, we show the contours of the a posteriori error $\hat{\epsilon}$ in the scenarios I1 and P1 for the individual fine-mode and coarse-mode parameters. Overall, observations in scenarios P1 offer more accurate retrievals for all parameters in both the fine and the coarse aerosol modes. In both scenarios, the $\hat{\epsilon}$ decreases for fine-mode parameters (left column) and increases for coarse-mode parameters (right column) with increasing the AE (or fmf_v) for same $\tau_{\text{A}440}$, indicating that the relative contribution of fine and coarse modes determines the relative information of each mode. Extreme cases are fmf_v of 1 or 0, i.e., the absence of the coarse- or fine-mode aerosols, which certainly will only allow a mono-modal retrieval. Thus, the bi-modal retrieval, especially for refractive indices, requires that aerosols reach certain mixture conditions to contain enough information for both modes. For example in the scenario I1, while the fine-mode r_{eff} can be well retrieved with 5% accuracy when the $\text{fmf}_v > 0.2$ at $\tau_{\text{A}440}$ of 0.5 (Figure 4.10b), the $\text{fmf}_v > 0.3$ is required to ensure the $\hat{\epsilon} < 0.02$ in the fine-mode m_r (Figures 4.10d). Comparing to the change of the fmf_v , the change of

Table 4.5: Required aerosol conditions (τ_{A440} and AE) to achieve anticipated retrieval accuracy $\langle \epsilon \rangle$ for observations in scenario I1 and P1.

| x | $\langle \epsilon \rangle$ | Scenario I1 | | Scenario P1 | |
|--------------------|----------------------------|---------------|-----------------------------|------------------|------|
| | | τ_{A440} | AE | τ_{A440} | AE |
| V_0^f | 10% | >0.3 | >1.5 | ^a All | All |
| V_0^c | 10% | <1.3 | <2.2 | All | All |
| r_{eff}^f | 5% | >0.3 | >1.3 | All | All |
| r_{eff}^c | 10% | All | <2.0 | All | <2.2 |
| v_{eff}^f | 20% | >0.3 | >1.5 | All | All |
| v_{eff}^c | 30% | All | <1.8 | All | <2.2 |
| m_r^f | 0.02 | >0.4 | ^b >1.0 | All | All |
| m_r^c | 0.04 | All | <1.0 | All | <1.8 |
| ω_A^f | 0.04 | >0.6 | >1.5 | >0.2 | >0.7 |
| ω_A^c | 0.08 | >0.2 | <1.1 | All | <1.6 |

^a'All' indicates conditions: $0.1 < \tau_{A440} < 2.0$ and $0.35 < \text{AE} < 2.3$;

^bUnderlined bold indicate conditions that cannot allow bi-modal retrievals.

τ_{A440} has less impact on the $\hat{\epsilon}$ of the PSD parameters; this impact occurs in low aerosol loadings. For example, Figure 4.10f shows that a minimum of ~ 0.4 for τ_{A440} is required in the scenario I1 to guarantee a retrieval error in the fine-mode ω_A less than 0.04 when $\text{fmf}_v = 0.5$.

From the Figure 4.10, we can identify required aerosol conditions in terms of the AE and τ_{A440} in order to achieve certain anticipated accuracy $\langle \epsilon \rangle$, which are summarized in Table 4.5. Clearly, observations with polarization can enable retrievals of equivalent accuracy in a lower aerosol loading. For example, the retrieval accuracy of 10% for the V_0^f and r_{eff}^f and 30% for the v_{eff}^f requires τ_{A440} to be larger than 0.3 for inversion in the scenario I1 (Figure 4.10a–c). In contrast, inversion in the scenario P1 can easily ensure retrievals of the same accuracy when τ_{A440} is 0.1. For the fine-mode m_r retrieval, an accuracy of 0.04 requires $\tau_{A440} > 0.4$ for the inversion I1 but $\tau_{A440} > 0.2$ for the inversion P1 (Figure 4.10d). Moreover, the radiance-only inversion is unable to resolve the bi-modal m_r and ω_A under any circumstance, because $\text{AE} > 1.5$ is necessary for retrieving the fine-mode ω_A (Figure 4.10f),

meanwhile $\text{AE} < 1.1$ is required for its coarse-mode retrieval (Figure 4.10l). This agrees with *Dubovik et al.* [2000] in that the retrieval of refractive indices for both fine and coarse mode is essentially non-unique due to limited information in the AERONET (radiance-only) observations. In contrast, observations in the scenario P1 can allow bi-modal retrievals of the m_i and ω_A when $0.7 < \text{AE} < 1.6$ and $\tau_{A440} > 0.2$ (Figures 4.10f and 4.10l). Therefore, our retrieval algorithm is designed to use observations of scenario P1 to retrieve bi-modal refractive indices when τ_{A440} and AE reach these criteria. In aerosol conditions beyond the criteria, bi-modal PSD along with a mono-modal refractive index will be retrieved by assuming the refractive index is independent of the aerosol mode.

4.5 Summary

In an effort to improve the AERONET inversion by including additional polarization measurements, this chapter examines the potential microphysical aerosol information contained in the AERONET photo-polarimetric observations. We have focused our analysis on how the added polarization measurements impact the retrieval accuracy for the aerosol particle size distribution (PSD), spectral refractive index, and single scattering albedo ω_A . A numerical testbed has been constructed to generate the synthetic AERONET radiance and degree of linear polarization (DOLP) over 440, 675, 870, and 1020 nm. We considered four scenarios of observations to that do or do not include the DOLP for the inversion, i.e., (I1) direct Sun AOD and almucantar sky radiances, (I2) observations in the scenario I1 with additional radiance measurements in the solar principal plane, (P1) observations in the scenario I2 plus polarization measurements in the solar principal plane, and (P2) observations in the scenario I1 plus almucantar polarization. Measurements in the scenario I1 are those used in current AERONET inversion algorithm, and thus represent a control experiment. For each observation scenario, we also considered three aerosol types to represent general aerosol

climatology. The Bayesian statistical approach then was applied to relate information contained in those synthetic data and retrieval errors in aerosol physical parameters to the instrumental as well as the a priori characteristics. Then the error-normalized Jacobian, degree of freedom for signal (DFS), and the a posteriori error in each individual retrieved parameter were presented as function of solar zenith angle for these observation scenarios.

The results show a remarkable increase in information by adding additional polarization and/or radiances into the inversion. Overall, observations in the scenario P1 yield the highest DFS, which is larger than that in the scenario I1 by 2–5 for all defined aerosol types. This can be understood as polarization measurements in the solar principal plane, in comparing with sky radiances in solar almucantar, have complementary sensitivities with respect to retrieved aerosol parameters. Also, measurements in the principal plane allow a wider range of scattering angles and supplies more information on aerosol backscattering. In scenario P2, adding polarization in the solar almucantar offer an increase of ~ 2 pieces of information with DFS values slightly below those in scenarios I2. We also note that the DFS increases with increasing solar zenith angle for all cases, resulting from more information contained in observations of a wider range of scattering angle.

We also analyzed the DFS components and the a posteriori uncertainty for each individual retrieved parameter. As expected, the smallest retrieval errors were always found in the scenario P1: 2.3% (2.9%) for the volume concentration, 1.3% (3.5%) and 7.2% (12%) for the effective radius and effective variance, 0.005 (0.035) for the real part of refractive index, and 0.019 (0.068) for the single scattering albedo in the fine (coarse) mode. These values represent an error reduction from the scenario I1 of 79% (57%), 76% (49%), 69% (52%), 66% (46%), and 49% (20%), respectively. Uncertainties in retrieved parameters averaged among these three aerosol types are summarized in the Table 4.4 for each observation scenario.

Seeking to answer under what conditions the inversions can achieve a mode-resolved

aerosol refractive index and ω_A , we further investigated how the AOD (τ_{A440}) and fine/coarse modal domination (in terms of Ångström exponent, or AE) influence the retrieving accuracy from observations in the scenarios I1 and P1. We found that adding principal-plane polarization measurements can increase the DFS by up to ~ 5 in cases dominated by coarse-mode particles ($fmf_v < 0.5$), in which the radiance-only inversion usually yields larger retrieval uncertainty for fine-mode aerosol. As a consequence, these photo-polarimetric observations can enable accurate retrievals in a lower aerosol loading when the τ_{A440} is 0.1, except for the fine-mode m_r retrieval that requires $\tau_{A440} > 0.2$. The analysis also indicate that the radiance-only inversion is unable to resolve bi-modal m_i and ω_A under any circumstance. However, observations in the scenario P1 can allow bi-modal retrievals of m_i and ω_A when $0.7 < AE < 1.6$. Such criteria can guide us in the practical retrieval algorithm to determine whether a mono-modal or bi-modal retrieval of the aerosol refractive index and ω_A is possible. In aerosol conditions beyond the criteria, bi-modal PSD along with the mode-independent refractive index will be retrieved.

Finally, it should be noted that in our analysis the aerosol particles in each mode are assumed to be poly-disperse homogeneous spheres. Although the linearized T-matrix code has been implemented in our model, the simulation of scattering properties for large non-spherical particles (for example spheroids) still remain computational limitations. Our future efforts will implement non-spherical treatment in order to more realistically represent mineral dust aerosols.

4.6 Acknowledgements

We thank Oleg Dubovik and Brent Holben for their encouragements and in-depth comments to the early version of this manuscript. We would also thank three anonymous reviewers for constructive suggestions. We acknowledge the computational support from the Holland

Computing Center at University of Nebraska. This work is supported by a NASA Earth and Space Science Fellowship and the NASA Radiation Sciences Program and the Glory mission program. This chapter has been submitted as an article to *Journal of Geophysical Research – Atmospheres* [[Xu and Wang, 2015](#)].

CHAPTER 5

CASE DEMONSTRATIONS

5.1 Introduction

As suggested by the information content analysis in Chapter 4, adding polarization data into the AERONET inversion will enable the retrieval of bi-modal refractive index and SSA even for 440-nm AOD as low as 0.2 when the Ångström exponents (AE) is between 0.7 and 1.6. We also found that the uncertainty in the retrieval can be reduced by up to 79% (57%), 76% (49%), 69% (52%), 66% (46%), and 49% (20%) for the fine-mode (coarse-mode) V_0 , r_{eff} , r_{eff} , m_r , and SSA, respectively. In this chapter, our new research algorithm is applied to a suite of photo-polarimetric measurements taken from the new-generation SunPhotometer at the AERONET station of Beijing_RADI. Below I present the selected cases and the *a priori* characterization in section 5.2, and discuss the fitting residuals in section 5.3 and the retrieved results in section 5.4. A contrast analysis is presented in section 5.5 to demonstrate the superiority of the inversion involving polarization.

5.2 Selected Cases and the *a priori* Characterization

We applied our algorithm to the radiance and polarization measured by the CIMEL CE318-DP SunPhotometer (instrument #350) at Beijing_RADI (116.37°E , 40.00°N), which is a joint station of the AERONET and the Sun/sky-radiometer Observation NETwork (SOnet).

The AOD measurements are designated from the field-calibrated level 1.5 products. Measurements of the direct and diffuse radiance as well as DOLP were performed at eight spectral wavelengths, with the measurements at 440, 675, 870, and 1020 nm chosen for the inversion. The sky radiances were calibrated following [Li et al. \[2008\]](#) and are reported as values normalized by the extra-terrestrial solar irradiance. The DOLP were calibrated in the laboratory following [Li et al. \[2010\]](#). Measurement uncertainties were estimated to be 0.01–0.02 for AOD, 3–5% for radiance, and 0.01 for DOLP.

The *a priori* is characterized with the climatology of aerosol properties derived from the version 2.0 AERONET daily inversion products of the same site during 2011–2013. The PSD parameters were analyzed with 299 available daily inversions when the 440-nm AOD is larger than 0.2. The refractive index and SSA were analyzed with 215 inversions when the 440-nm AOD is larger than 0.4. In Figure 5.1, the variables are shown as functions of the fine-mode-fraction in terms of the aerosol volume, or fmf_v . It can be found that the fmf_v from 0.2 to 0.6 accounts for ~70% of occurrences (Figure 5.1a), indicating aerosol over this site is dominated by the mixed fine-coarse aerosols. The AE derived from the 1020-nm and 870-nm AOD pairs is more linearly related to the fmf_v than the 440-nm and 870-nm AE (Figure 5.1b), because AE over the longer-wavelength pairs is more sensitive to the component fraction and less sensitive to the change of component particle size [[Schuster et al., 2006](#)]. From Figure 5.1c–f, we determine the *a priori* (\mathbf{x}_a) based on the corresponding mean values. For refractive index, we pick their mean values when $\text{fmf}_v < 0.2$ for the coarse

Table 5.1: Main characteristics of case studies in this work.

| Case | Date & Time UTC | $\theta_0(^{\circ})$ | τ_{A440} | AE (870/1020nm) | OMI NO_2 (molec/cm ²) | OMI O_3 (DU) | Vapor (cm) |
|------|--------------------|----------------------|---------------|--------------------|---|--------------------------|---------------|
| A | 02/22/2011 04:30 | 50.3–50.6 | 3.46 | 1.57 | 6.3×10^{16} | 356.5 | 0.86 |
| B | 03/17/2013 03:25 | 43.0–42.2 | 2.74 | 1.39 | 4.2×10^{16} | 332.7 | 0.76 |
| C | 03/22/2013 07:23 | 57.0–60.0 | 1.05 | 1.01 | 4.1×10^{16} | 386.7 | 1.01 |

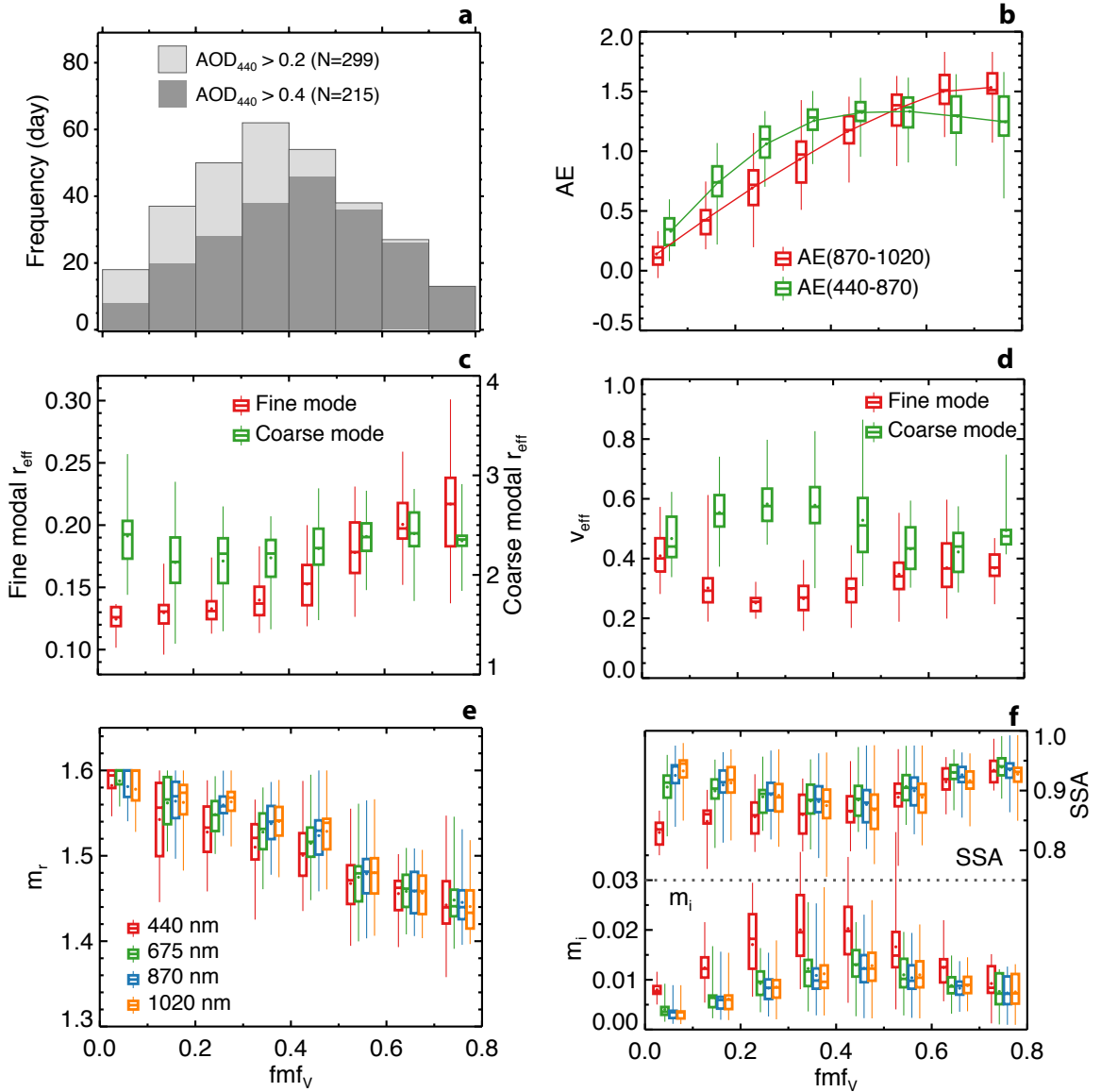


Figure 5.1: Climatology of aerosol properties over the Beijing_RADI site derived from AERONET daily inversion products during 2011–2013. The variables are shown as functions of the fine-mode-fraction in terms of the aerosol volume, or fmf_v . Eight bins are applied for fmf_v from 0 to 0.8 with an increment of 0.1. The six panels are: (a) Histogram of used data; (b) the Ångström exponents (AE) derived from 870 to 1020 nm (red) and from 440 to 870 nm (green) wavelength pairs; (c) the effective radius for aerosols in the fine (red) and coarse (green) mode; (d) the effective variance in the fine (red) and coarse (green) mode; (e) the real part of the refractive index at 440, 675, 870, and 1020 nm; and (f) the imaginary part of the refractive index and aerosol SSA at the same wavelengths.

mode and when $\text{fmf}_v > 0.6$ for the fine mode. The *a priori* error (ε_a) for each parameter is determined by the relevant physical range, and is listed in the last column of Table 5.4. In addition, we found in the Figure 5.1e that the m_r retrievals decrease quasi-linearly with the increasing fmf_v , which indicates the m_r has distinct values between aerosols in the fine and the coarse modes over this site. It is expected that the m_r in the mixed aerosol situations, e.g., $0.3 < \text{fmf}_v < 0.6$, is also expected to have the separated values for fine- and coarse-mode particles.

With the above *a priori* characterization, we performed retrievals for three cases, respectively, on 22 February 2011, 17 March 2013, and 22 March 2013 (hereinafter, cases A, B, and C). A brief characterization of these cases is presented in Table 5.1. Indeed, these cases represent different aerosol mixtures: (A) dominated by fine particles, (B) well-mixed, and (C) dominated by large particles. Moreover, the present algorithm is designed to run with two inversion scenarios: the first includes DOLP, while the second ignores it—hereafter, we label these scenarios type P and I, respectively. An examination of the difference in the fitting results between these two types of inversion would indicate the value of DOLP in improving the retrieval. For all cases, optimal solutions are achieved within less than thirty iterations, and further iterations yield negligible reduction of the cost function.

5.3 Fitting Residuals

The fitting residual characterizes the disagreement between the model and the measurement. The individual sky radiance residual is defined as a relative quantity:

$$e_I = (I_{\text{calc}} - I_{\text{meas}}) / I_{\text{meas}} \quad (5.1)$$

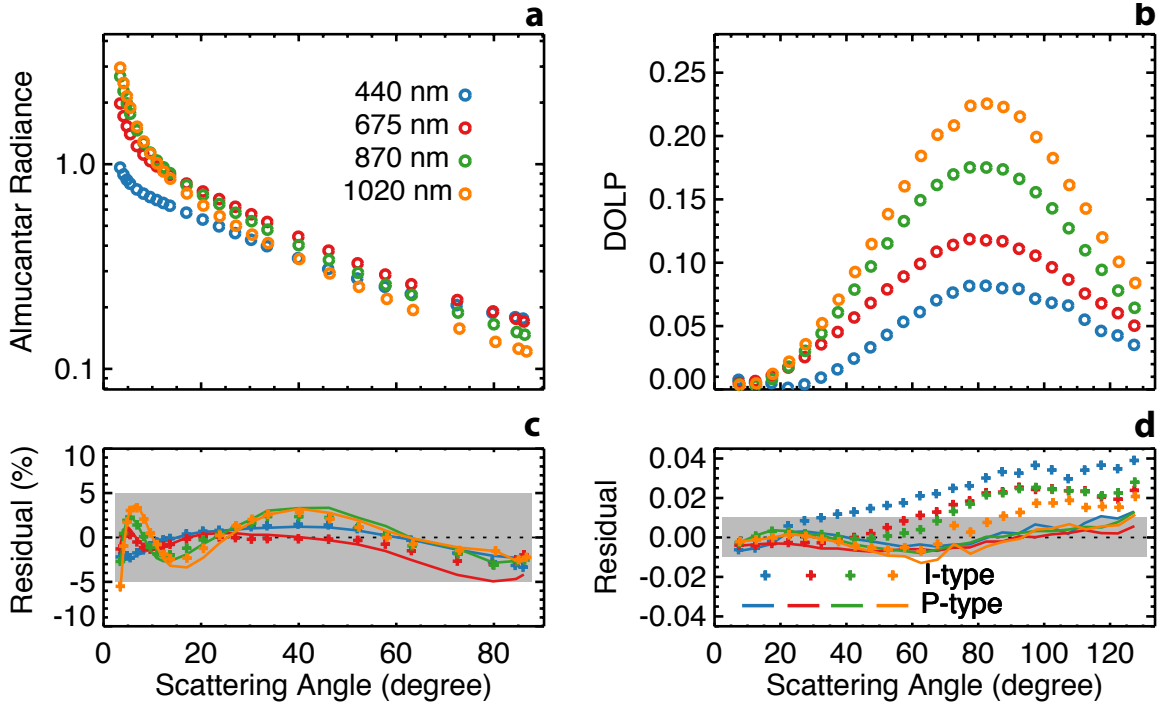


Figure 5.2: a) Measured almucantar normalized radiances. (b) Measured DOLP in the solar principal plane. (c) Fitting residuals for almucantar radiances by the P-type inversion (solid curves) and I-type inversion (crosses). (d) Same as panel (c), but for fitting the residuals of principal-plane DOLP. Four colors indicate different wavelengths: blue for 440 nm, green for 675 nm, red for 870 nm, and orange for 1020 nm. Gray areas in panels c–d indicate the measurement uncertainty.

where I_{calc} and I_{meas} denote the calculated (using the retrieved aerosol parameters) and measured sky radiances, respectively. In contrast, the fitting residuals for AOD and DOLP are defined by:

$$e_{\text{AOD}} = \text{AOD}_{\text{calc}} - \text{AOD}_{\text{meas}}, \quad (5.2)$$

$$e_{\text{DOLP}} = \text{DOLP}_{\text{calc}} - \text{DOLP}_{\text{meas}}. \quad (5.3)$$

The residual errors for AOD, sky radiance, and DLOP are mean values of $|e_{\text{I}}|$, $|e_{\text{AOD}}|$, and $|e_{\text{DOLP}}|$, respectively.

Because similar fitting results are found for these three aerosol types (cases), we illustrate

Table 5.2: Summary of measurement fitting errors.

| Case | Inversion type | AOD residual error | Radiance residual error | DOLP residual error |
|------|----------------|--------------------|-------------------------|---------------------|
| A | I | 0.0005 | 1.68% | 0.008 |
| | P | 0.0010 | 1.78% | 0.005 |
| B | I | 0.0003 | 1.43% | 0.014 |
| | P | 0.0003 | 1.67% | 0.004 |
| C | I | 0.0007 | 2.77% | 0.027 |
| | P | 0.0034 | 3.73% | 0.009 |

in Figure 5.2 the fitting results for sky radiances and DOLP only for the case B. The statistical residual errors are displayed in Table 5.2 for all three cases. We found that retrievals from both types of inversion can well reproduce these AERONET measurements of AOD and sky radiances. Fitting residuals from both types of inversions for individual ALM radiance measurement lie within the experimental uncertainty of 5%, although the fit of radiances from the P-type inversion is slightly deteriorated: residual error is 1.67% for the P-type compared 1.43% for the I-type inversion. However, the DOLP residual error can be much larger for the I-type inversion than that for the P-type inversion: 0.014 versus 0.004. As these fitting results show, without the constraints imposed by polarization, the retrieved aerosol microphysical parameters could result in larger error in polarization simulations, highlighting the necessity to include polarization in the inversion as an additional source of constraint.

5.4 Retrieved Aerosol Properties

Figure 5.3 displays our retrievals from both I-type and P-type inversions for the aerosol volume PSD and complex refractive indices. Also shown are the retrievals from the AERONET Dubovik00&06 inversion. Table 5.3 presents the values of the (P-type inversion) retrieved PSD parameters including V_0 , r_{eff} , ν_{eff} , r_v , and σ_g for both fine and coarse modes, and

corresponding values from the Dubovik00&06 inversion. The PSD in these cases consists of separated fine and coarse aerosol modes. In the cases dominated by fine-mode aerosol (A) and well-mixed aerosol (B), our retrievals agree with the AERONET inversions, though marginal differences are found in the effective radius and standard deviation. In case C dominated by coarse-mode aerosols, our algorithm results in a smaller coarse mode r_{eff} than that from the AERONET algorithm; this may be caused by our assumption of spherical particles, whereas the Dubovik00&06 algorithm considers non-sphericity for coarse particles. We did not find significant differences in the aerosol volumes between our algorithm and the Dubovik00&06 algorithm. As Figure 5.3b–c indicate, fine-mode volume retrieved by the P-type inversion is lower than that retrieved by the I-type inversion; such an overestimation from radiance-only inversion was also found by [Li et al. \[2009\]](#).

In contrast with the Dubovik00&06 algorithm, which retrieves a single refractive index for each spectrum that is independent of aerosol size, our retrieved aerosol refractive indices pertain to the corresponding fine and coarse modes. In order to get a general impression of the agreement between our retrievals and the AERONET inversions, we compute the bulk refractive index that is a weighted average by the particle volume of each mode in our retrieval [e.g., [Wang and Martin, 2007](#)]. According to Figure 5.3d–f, while the bulk value of m_r is in good agreement (differences < 0.03) with that of the Dubovik00&06 retrievals, our retrieval allows for a mode-resolved characterization of aerosol refractive index. For instance, the aerosol m_r has values 1.5–1.6 in the coarse mode, which is larger than that in the fine mode (1.4–1.5). In addition, we found that the P-type inversion usually yields higher values of m_r compared to the I-type inversion; this finding agrees with [Li et al. \[2009\]](#) in that the radiance-only inversion underestimates m_r .

According to Figure 5.3g–i, the bulk m_i retrieved by our algorithm is consistent overall with that from the Dubovik00&06 algorithm, with both retrievals showing similar spectral dependencies. One exception is for case C; m_i at 440 nm is about 0.01 from our algorithm but

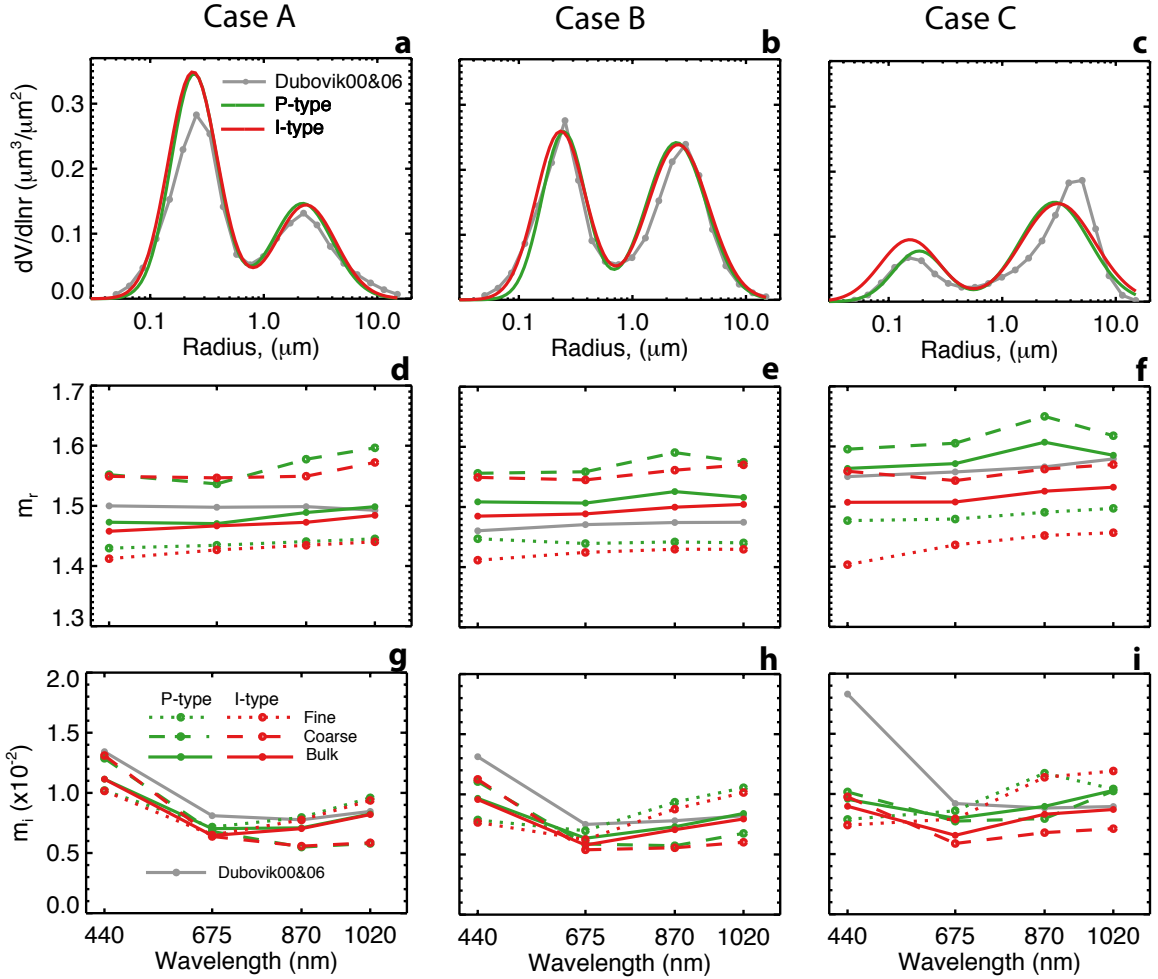


Figure 5.3: Retrieved aerosol volume size distribution (PSD) and refractive index compared with Dubovik00&06 inversions (gray). P-type and I-type inversions are represented by green and red colors, respectively. In panels d–i, the retrievals are shown for aerosols in both fine (dotted) and coarse (dashed) modes, as well as bulk averages (solid). The PSD relevant quantities for panels a–c are summarized in Table 5.3.

is about 0.02 with the Dubovik00&06 algorithm. As expected, our inversion algorithm also offers mode-resolved m_i . We notice in our retrieval that m_i shows an increasing dependence on the spectral wavelength for the fine mode but a decreasing tendency for the coarse mode.

In the forward modeling framework, the aerosol macrophysical optical properties act as intermediate model parameters to link the aerosol microphysical characteristics to the radiation fields. These macrophysical optical parameters include but are not limited to the

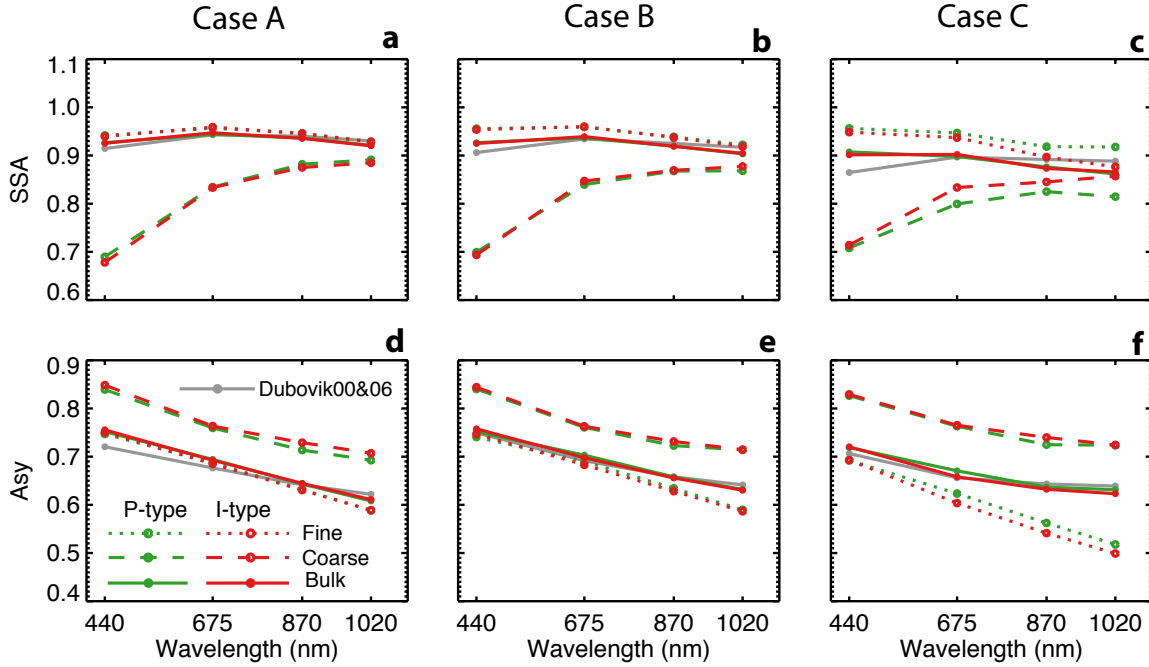


Figure 5.4: Same as Figure 5.3, but for derived aerosol SSA and Asy.

aerosol SSA (ω_A), the scattering phase function, and the asymmetry factor (Asy). These quantities do not appear in the state vector; instead, they can be derived from the retrieved microphysical parameters, and are thus called derived or intermediate parameters. In Figure 5.4, we present ω_A and Asy from our retrieval, and the comparison with their counterparts from the Dubovik00&06 inversion. In our retrieval, bulk values of ω_A and Asy are again calculated by a scatter-weight averaging of the fine and coarse mode values. We found that the bulk ω_A and Asy from our algorithm and the Dubovik00&06 algorithm agree very well. However, our retrieved coarse-mode ω_A varies from 0.7 to 0.9, increasing with wavelength. In contrast, the retrieved fine-mode ω_A runs close to 0.9.

5.5 Improvement over Radiance-Only Retrievals

The above comparisons of retrieval results confirm that both P- and I-type inversions by our algorithm can generate solutions quite consistent with the current Dubovik00&06 algorithm.

Table 5.3: PSD-related parameters retrieved by our P-type inversion, compared with values from the AERONET Dubovik00&06 inversion.

| x | Units | Case A | | Case B | | Case C | |
|--------------------|---------------------------------|--------|---------|--------|---------|--------|---------|
| | | Ours | AERONET | Ours | AERONET | Ours | AERONET |
| V_0^f | $\mu\text{m}^3\mu\text{m}^{-2}$ | 0.41 | 0.36 | 0.29 | 0.31 | 0.10 | 0.09 |
| r_{eff}^f | μm | 0.218 | 0.208 | 0.226 | 0.201 | 0.163 | 0.156 |
| v_{eff}^f | – | 0.25 | 0.32 | 0.22 | 0.32 | 0.31 | 0.33 |
| r_v^f | μm | 0.243 | 0.240 | 0.249 | 0.232 | 0.186 | 0.179 |
| σ_g^f | – | 1.60 | 1.69 | 1.56 | 1.69 | 1.68 | 1.70 |
| V_0^c | $\mu\text{m}^3\mu\text{m}^{-2}$ | 0.22 | 0.21 | 0.37 | 0.32 | 0.27 | 0.26 |
| r_{eff}^c | μm | 1.83 | 2.01 | 2.02 | 2.26 | 2.26 | 2.61 |
| v_{eff}^c | – | 0.44 | 0.53 | 0.45 | 0.38 | 0.65 | 0.50 |
| r_v^c | μm | 2.20 | 2.44 | 2.44 | 2.65 | 2.91 | 3.28 |
| σ_g^c | – | 1.83 | 1.92 | 1.84 | 1.76 | 2.03 | 1.89 |

In order to demonstrate the improvements in the retrieval by including polarization, we compare the retrieval errors between the P-type and I-type inversions in Table 5.4 for individual aerosol parameters. Also compared are the errors in the derived ω_A and Asy. Clearly, the P-type inversion yields lower retrieval errors for all the retrieved and derived parameters; this is confirmed by the theoretical analysis in Chapter 4 of this thesis. The key points from the comparison are:

- (i) Polarization measurements provide important constraints in improving the retrieval of V_0 , r_{eff} , and v_{eff} for both fine and coarse aerosol modes. For these three cases, the errors in the retrieved V_0 with polarization are less than 3% for the fine mode and less than 5% for the coarse mode, representing a significant decrease from their counterparts ($\sim 15\%$ and $\sim 10\%$) in the I-type inversion. Adding polarization can also decrease the error in r_{eff} of both fine and coarse modes from 10–15% for the I-type inversion to 3% and below. Errors in v_{eff} retrieved by the P-type inversion are 9–11% for aerosol in the fine mode and 17–26% in the coarse mode, whereas they can exceed 60% with the I-type inversion.
- (ii) Polarization measurements also provide useful constraints in improving the refractive

Table 5.4: Errors on the retrieved and derived parameters from both types of inversion^a.

| \mathbf{x} | Case A | | Case B | | Case C | | ε_a |
|--------------------|-----------------------|-----------------------|-----------------------|-----------------------|-----------------------|-----------------------|-----------------|
| | $\hat{\varepsilon}_P$ | $\hat{\varepsilon}_I$ | $\hat{\varepsilon}_P$ | $\hat{\varepsilon}_I$ | $\hat{\varepsilon}_P$ | $\hat{\varepsilon}_I$ | |
| V_0^f | 2.1% | 15% | 2.2% | 18% | 3.0% | 25% | 100% |
| r_{eff}^f | 1.3% | 9.2% | 1.3% | 11% | 2.4% | 14% | 80% |
| v_{eff}^f | 9.3% | 33% | 9.3% | 38% | 11% | 33% | 80% |
| m_r^f | 0.005 | 0.020 | 0.006 | 0.023 | 0.009 | 0.035 | 0.14 |
| m_i^f | 0.002 | 0.002 | 0.003 | 0.004 | 0.004 | 0.006 | 0.010 |
| ω_A^f | 0.009 | 0.010 | 0.016 | 0.018 | 0.021 | 0.037 | – |
| Asy ^f | 0.003 | 0.005 | 0.003 | 0.006 | 0.003 | 0.009 | – |
| V_0^c | 4.8% | 14% | 3.2% | 10% | 2.9% | 9.4% | 100% |
| r_{eff}^c | 6.7% | 15% | 3.3% | 7.1% | 1.9% | 6.0% | 80% |
| v_{eff}^c | 26% | 66% | 17% | 48% | 10% | 33% | 80% |
| m_r^c | 0.108 | 0.137 | 0.080 | 0.122 | 0.044 | 0.100 | 0.16 |
| m_i^c | 0.006 | 0.007 | 0.005 | 0.006 | 0.003 | 0.005 | 0.008 |
| ω_A^c | 0.059 | 0.065 | 0.050 | 0.058 | 0.031 | 0.051 | – |
| Asy ^c | 0.024 | 0.036 | 0.018 | 0.028 | 0.012 | 0.025 | – |

^a $\hat{\varepsilon}_P$ and $\hat{\varepsilon}_I$ are retrieval error respectively from the P-type and I-type inversions, ε_a is the a priori error.

index retrievals. The most significant improvement is found in the fine-mode m_r , where the error is lower than 0.01 for the P-type inversion, compared to 0.02–0.04 for the I-type inversion. The error in the coarse-mode m_r from P-type inversion ranges from 0.04 to 0.11, depending on the prevalence of coarse-mode particles. For retrieving m_i , the inclusion of polarization reduces the error by 10–30%, a value also depending on coarse-mode dominance.

(iii) Adding the polarization yields better estimates of the aerosol SSA and Asy for both aerosol modes. From P-type inversion, the errors in the retrieved ω_A are lower than 0.02 for aerosols in the fine mode and 0.06 for aerosols in the coarse mode, representing a 10–40% decrease from the I-type inversion. As expected, errors in the Asy also reveal a 30–50% decrease.

5.6 Summary

In this chapter, we applied the new algorithm to a suite of photo-polarimetric measurements taken from the new-generation SunPhotometer at the Beijing_RADI AERONET station. In order to demonstrate the importance of adding polarization measurements, we performed aerosol retrievals from radiance measurements only (the I-type inversion), in addition to the retrievals using both radiance and polarization measurements (the P-type inversion). We found that, for both types of inversion, the fitting errors for the AOD and sky radiance are much smaller than the calibration uncertainties (0.02 for AOD and 5% for sky radiance). Also, the fitting errors of the degree of linear polarization (DOLP) with the P-type inversion are much smaller than the calibration error (~ 0.01). However, the DOLP fitting errors in the I-type inversion usually exceed 0.01, and even reach 0.04 for many individual measurements in the case dominated by coarse aerosols, which highlights the necessity to include polarization in the inversion as an additional source of constraint.

Our retrieval results are generally consistent with the AERONET inversion products, but we found distinct differences between the values of the refractive index and SSA for the fine- and coarse-mode aerosols. For these three cases selected for our study, we found that the retrieved real part refractive index is about 1.5–1.6 in the coarse mode, which is higher than those for the fine mode, 1.4–1.5. Also, the coarse-mode aerosols are more absorbing than the fine-mode ones.

We also compared the retrieval error for each retrieved parameters between the I-type and P-type inversions. A comparison analysis indicates that the retrieval error can be reduced by at least 50% in PSD parameters, by 10–30% in the refractive index components, and by 10–40% in the aerosol SSA. These error reductions depend on the fine/coarse-mode fraction, specifics of instrumentation, and aerosol properties. These improvements in the P-type inversion are consistent with the theoretical analysis in Chapter 4 of this thesis.

The promising results in this study are obtained from the initial development and preliminary applications of a new algorithm targeted for the retrieval of aerosol properties from new-generation AERONET measurements. Future developments will include, but not be limited to, the treatment of non-spherical large aerosol particles like mineral dust, and the consideration of tri-modal aerosols for special situations. While the bi-lognormal PSD can well represent the aerosol size spectrum in most cases, future research efforts will include the implementation of tri-modal aerosol mixtures in situations of cloud formation [Eck *et al.*, 2012] or volcanic aerosols [Eck *et al.*, 2010]. Moreover, extensive retrievals for a longer period of time will also be performed over sites where CE318-DP SunPhotometer instruments have been installed (i.e., Beijing_RADI and Lille).

5.7 Acknowledgements

We thank Li Li for providing the AERONET radiance and polarization measurements over Beijing_RADI site. We acknowledge the computational support from the Holland Computing Center at University of Nebraska. This work is supported by a NASA Earth and Space Science Fellowship and the NASA Radiation Sciences Program and the Glory mission program. This chapter has been submitted as an article to *Journal of Geophysical Research – Atmospheres* [Xu *et al.*, 2015].

CHAPTER 6

CONCLUSIONS AND OUTLOOK

6.1 Conclusions

Aerosols have been recognized as major components of the Earth's climate system, influencing the radiative budget, clouds, and precipitation processes. An accurate assessment of these effects requires realistic representation of the aerosol loading and distribution across the globe, as well as the characteristics of the aerosol particle size distribution and chemical composition (refractive index).

The objective of this thesis is to contribute an improved research algorithm retrieving aerosol microphysical properties from AERONET measurements of light radiance and polarization, with emphasis on elucidating the potentially important role of polarization measurements. As outlined in section 1.2, specific investigations towards this research goal are: the development of an retrieval algorithm that integrates a rigorous radiative transfer model (Chapter 2) and statistical optimized inversion (Chapter 3), the examination of potential aerosol information contained in the AERONET polarizaton measurements (Chapter 4), and the application of our designed inversion algorithm to the real AERONET measurements (Chapter 5). Below, I briefly summarize the contributions of this thesis by these three investigations.

6.1.1 UNL-VRTM and new AERONET inversion algorithm

The UNified Linearized Vector Radiative Transfer Model, or UNL-VRTM integrates the linearized codes computing vector radiative transfer (VLIDORT) and scattering of spherical (LMIE) and non-spherical (LTMATRIX) particles, hyper-spectral treatment for air molecular scattering and gaseous absorption, and models describing bidirectional surface reflectance and polarization (BRDF/BPDF). As shown in Chapter 2, the direct coupling of these components by UNL-VRTM allows it not only able to compute the four Stokes parameters and degree of linear polarization (DOLP) with high accuracy and high spectral resolution, but also to simultaneously and analytically generate sensitivities of these Stokes parameters with respect to aerosol parameters of both the fine and coarse modes. By inclusion of HITRAN and other molecular spectroscopy data for atmospheric trace gases, the UNL-VRTM is also able to perform line-by-line calculation of gas absorption, thus providing another opportunity for the future study of the effect of absorbing gases (such as SO₂, NO₂, O₃, and water vapor) on the aerosol retrieval. Although the UNL-VRTM is used to simulate the AERONET measurements in this work, the module-based structure of UNL-VRTM allows a broad application to the remote sensing observations from other platforms.

In Chapter 3, I have presented a new algorithm to retrieve both fine- and coarse-mode aerosol properties from multi-spectral and multi-angular solar polarimetric radiation fields measured by AERONET including additional spectra of polarization observations. The retrieval algorithm uses UNL-VRTM and incorporates the statistical optimized inversion to retrieve aerosol parameters pertaining to a bi-lognormal particle size distribution (PSD), including the aerosol volume concentration, effective radius and variance, and complex indices of refraction. While the new algorithm has heritage from the existing AERONET inversion algorithm in using multiple a priori constraints, it is different from the existing AERONET algorithm in that: (a) a bi-modal lognormal PSD (instead of 22 size bins) is

assumed; (b) the spectral refractive indices are retrievable for both fine and coarse modes. The mode-separated aerosol microphysical and optical retrievals can benefit the analysis for aerosol chemical compositions and climate radiative impacts study of aerosol, and most importantly, can thereby facilitate the evaluation of atmospheric chemistry models and the validation of aerosol products from satellite sensors with polarization capability.

6.1.2 Potential information contained in AERONET polarization

In Chapter 4, I have examined the potential microphysical aerosol information contained in the AERONET photo-polarimetric observations. The analysis focused on how the added polarization measurements impact on the retrieval accuracy the in aerosol particle size distribution, spectral refractive index, and single scattering albedo. We used the UNL-VRTM to generate the synthetic AERONET spectral radiance and DOLP, as well as their sensitivities with respect to these aerosol properties. Then, we quantify the aerosol infomation content in various observation scenarios in terms of degree of freedom for signal (DFS) and *a posteriori* error.

The results show a remarkable increase in information by adding additional polarization and/or radiances into the inversion: an overall increase of 2–5 of DFS comparing with radiance-only measurements. Correspondingly, smallest retrieval errors are found in the added-polarization scenario: 2.3% (2.9%) for the fine-mode (coarse-mode) aerosol volume concentration, 1.3% (3.5%) for the effective radius, 7.2% (12%) for the effective variance, 0.005 (0.035) for the real part refractive index, and 0.019 (0.068) for the single scattering albedo. These errors represent a reduction from their counterparts in the radiance-only scenario of 79% (57%), 76% (49%), 69% (52%), 66% (46%), and 49% (20%), respectively.

We have further investigated those retrieval errors over a variety of aerosol loading and fine/coarse-mode prevalence (section 4.4), which indicates that the combined use of radiance

and polarization observations can yield the retrieval of refractive index and single scattering albedo for both fine and coarse aerosol modes, when AOD at 440 nm is larger than 0.2 and 870/1020-nm Ångström exponent ranges between 0.7 and 1.6.

6.1.3 Application to real retrieval

In Chapter 5, we have applied our new AERONET inversion algorithm to a suite of real cases over Beijing_RADI site. We found that our retrievals are overall consistent with AERONET operational inversions, but can offer mode-resolved refractive index and SSA with acceptable accuracy for the aerosol composed by spherical particles. Along with the retrieval using both radiance and polarization, we also performed radiance-only retrieval to demonstrate the improvements by adding polarization in the inversion. Contrast analysis indicates that with polarization, retrieval error can be reduced by over 50% in PSD parameters, 10–30% in the refractive index, and 10–40% in SSA, which is consistent with theoretical analysis presented in Chapter 4.

6.2 Outlook and Future Work

The promising results in this study are obtained from the initial development and preliminary applications of a new algorithm targeted for the retrieval of aerosol properties from new-generation AERONET measurements. Future developments will include, but not be limited to, the treatment of non-spherical large aerosol particles like mineral dust, and the consideration of tri-modal aerosols for special situations. Another interesting research topic is to investigate the chemical composition from the multi-spectral and multi-angular photo-polarimetric measurements. Below, I list particularly promising directions for future investigations.

1. Implement the consideration of non-spherical dust. Conclusions of this work are based on consideration of spherical aerosol particles. However, the studies by *Dubovik et al.* [2006] and *Deuzé et al.* [1993, 2001] revealed serious limitation of polarimetric retrieval of the properties for coarse, especially non-spherical aerosols. Therefore, treatment of non-spherical optical scattering properties is necessary to improve our understanding on how polarization can benefit the retrieval for dust aerosols.
2. While the bi-lognormal PSD can well represent the aerosol size spectrum in most cases, future research efforts will include the implementation of tri-modal aerosol mixtures in situations of cloud formation [*Eck et al.*, 2012] or volcanic aerosols [*Eck et al.*, 2010].
3. Explore the potential use of multi-spectral and multi-angular photo-polarimetric measurements for the retrieval of aerosol chemical composition. This will benefit the source identification of species-specified aerosols.
4. Last but not least, extensive retrievals for a longer period are on-going over sites where CE318-DP SunPhotometer instruments have been installed (i.e., Beijing_RADI and Lille). Such long-term retrievals will provide more robust resources for studying the aerosol climatology.

APPENDIX A

DERIVATIONS OF TRANSFORMATION VECTOR Π

This appendix presents the derivations of equations (2.19) and (2.21) and the expressions in Table 2.1 and Table 2.2. It should be noted that all optical parameters are functions of wavelength and defined for each atmospheric layer, but we omit indicating symbols for wavelength and air layer for simplicity.

Let x be an aerosol microphysical parameter. The aerosol extinction and scattering optical thickness (τ_A and δ_A), single scattering albedo (ω_A), and Greek coefficient matrix (\mathbf{B}_A^j) are functions of x . However, the gaseous absorption and Rayleigh scattering parameters are independent of x .

First, we transform equation (2.18) as below:

$$\phi_x = \frac{x}{\tau} \frac{\partial \tau}{\partial x} = \frac{x}{\tau} \frac{\partial(\tau_G + \tau_R + \tau_A)}{\partial x} = \frac{1}{\tau} x \frac{\partial \tau_A}{\partial x} \quad (\text{A.1})$$

$$\begin{aligned} \varphi_x &= \frac{x}{\omega} \frac{\partial \omega}{\partial x} = \frac{x}{\omega} \frac{[(\delta_A + \tau_G)]}{\partial x} \\ &= \frac{x}{\omega \tau^2} \left[\tau \frac{\partial(\delta_A + \tau_R)}{\partial x} - (\delta_A + \tau_R) \frac{\partial \tau}{\partial x} \right] \\ &= \frac{x}{\omega \tau} \frac{\partial \delta_A}{\partial x} - (\delta_A + \tau_R) \frac{x}{\omega \tau^2} \frac{\partial \tau_A}{\partial x} \\ &= \frac{x}{\delta_A + \tau_R} \frac{\partial \delta_A}{\partial x} - \frac{1}{\tau} \frac{\partial \tau_A}{\partial x} \\ &= \frac{x}{\delta_A + \tau_R} \frac{\partial \delta_A}{\partial x} - \phi_x \end{aligned} \quad (\text{A.2})$$

$$\begin{aligned}
\Psi_x^j &= \frac{x}{\mathbf{B}^j} \frac{\partial \mathbf{B}^j}{\partial x} = \frac{x}{\mathbf{B}^j} \frac{\partial [(\tau_R \mathbf{B}_R^j + \delta_A \mathbf{B}_A^j) / (\delta_A + \tau_R)]}{\partial x} \\
&= \frac{x}{\mathbf{B}^j} \frac{1}{(\delta_A + \tau_R)^2} \left[(\delta_A + \tau_R) \frac{\partial (\delta_A \mathbf{B}_A^j)}{\partial x} - (\tau_R \mathbf{B}_R^j + \delta_A \mathbf{B}_A^j) \frac{\partial \delta_A}{\partial x} \right] \\
&= \frac{x}{\mathbf{B}^j} \frac{1}{\delta_A + \tau_R} \left[\frac{\partial (\delta_A \mathbf{B}_A^j)}{\partial x} - \mathbf{B}^j \frac{\partial \delta_A}{\partial x} \right] \\
&= \frac{1}{(\delta_A + \tau_R) \mathbf{B}^j} \left[\delta_A x \frac{\mathbf{B}_A^j}{\partial x} + (\mathbf{B}_A^j - \mathbf{B}^j) x \frac{\partial \delta_A}{\partial x} \right]
\end{aligned} \tag{A.3}$$

These expressions are linear combinations of ϕ'_x , φ'_x , and $\Psi_x'^j$ (as defined by equation (2.20)), where

$$\left[\phi'_x, \varphi'_x, \langle \Psi_x'^j \rangle_{j=1,J} \right]^T = \left[x \frac{\partial \tau_A}{\partial x}, x \frac{\partial \delta_A}{\partial x}, \left\langle x \frac{\partial \mathbf{B}_A^j}{\partial x} \right\rangle_{j=1,J} \right]^T \tag{A.4}$$

We then can write above equations (A.1)–(A.3) into vector formulism (as equation (2.19)):

$$\left[\phi_x, \varphi_x, \langle \Psi_x^j \rangle_{j=1,J} \right]^T = \boldsymbol{\Pi} \left[\phi'_x, \varphi'_x, \langle \Psi_x'^j \rangle_{j=1,J} \right]^T \tag{A.5}$$

where $\boldsymbol{\Pi}$ is a matrix comprising the relevant coefficients, as noted in equation (2.21). Equations (A.5) and (2.21) then act as a universal formulation for preparing linearized inputs of optical property for VLIDORT. Computation of $\left[\phi_x, \varphi_x, \langle \Psi_x^j \rangle_{j=1,J} \right]$ can then be achieved by the calculation of $\left[\phi'_x, \varphi'_x, \langle \Psi_x'^j \rangle_{j=1,J} \right]$ for a given parameter x .

Let us first consider the derivation of $\left[\phi'_x, \varphi'_x, \langle \Psi_x'^j \rangle_{j=1,J} \right]$ for certain aerosol optical properties in a given atmospheric layer, i.e., τ_A , ω_A , and β_A^k , where β_A^k indicates one of the elements in the k th aerosol scattering Greek matrix \mathbf{B}_A^k .

For $x = \tau_A$, we have

$$\phi'_x = \tau_A \frac{\partial \tau_A}{\partial \tau_A} = \tau_A \quad (\text{A.6})$$

$$\varphi'_x = \tau_A \frac{\partial \delta_A}{\partial \tau_A} = \tau_A \omega_A \quad (\text{A.7})$$

$$\Psi'^j_x = \tau_A \frac{\partial \mathbf{B}_A^j}{\partial \tau_A} = \mathbf{0} \quad (\text{A.8})$$

For $x = \omega_A$, we have

$$\phi'_x = \omega_A \frac{\partial \tau_A}{\partial \omega_A} = 0 \quad (\text{A.9})$$

$$\varphi'_x = \omega_A \frac{\partial \delta_A}{\partial \omega_A} = \omega_A \tau_A \quad (\text{A.10})$$

$$\Psi'^j_x = \omega_A \frac{\partial \mathbf{B}_A^j}{\partial \omega_A} = \mathbf{0} \quad (\text{A.11})$$

For $x = \beta_A^k$, we have

$$\phi'_x = \beta_A^k \frac{\partial \tau_A}{\partial \beta_A^k} = 0 \quad (\text{A.12})$$

$$\varphi'_x = \beta_A^k \frac{\partial \delta_A}{\partial \beta_A^k} = 0 \quad (\text{A.13})$$

$$\Psi'^j_x = \beta_A^k \frac{\partial \mathbf{B}_A^j}{\partial \beta_A^k} = \begin{cases} \frac{\delta_A \beta_A^k}{\beta_A^k} & \text{if } j = k \\ 0 & \text{if } j \neq k \end{cases} \quad (\text{A.14})$$

Expressions in Table 2.1 are then derived by substituting equations (A.6)–(A.14) into equation (A.5).

The UNL-VRTM integrates the VLIDORT with linearized Mie/T-matrix codes, and this combination allows us to generate Stokes vectors and associated analytical Jacobians with respect to aerosol microphysical parameters for two aerosol modes. Thus, we must supply the

$\left[\phi'_x, \varphi'_x, \langle \Psi'_x^j \rangle_{j=1,J} \right]$ quantities for all such parameters. We give an example here, assuming that the aerosols are bimodal, with two lognormal size distributions described by geometric standard deviations (σ_g^f and σ_g^c), geometric median radii (r_g^f and r_g^c), and non-sphericity parameters (ε^f and ε^c) for the fine and coarse modes. We note that ε is available only when non-spherical particles are assumed (T-matrix code is applied). Complex refractive indices are $m_r^f - m_i^f i$ and $m_r^c - m_i^c i$. Given these microphysical properties, the linearized Mie/T-matrix codes will compute for each mode the scattering and extinction efficiencies (Q_{sca} and Q_{ext}), the set of expansion coefficients (\mathbf{B}_A^j) of scattering phase matrix, as well as the derivatives of these quantities with respect to these microphysical properties. For a wide size range of aerosol particles, which enable about 100% accumulated value for the bi-lognormal probability function, the optical thickness for aerosol extinction and scattering and the associated Greek matrix coefficients within for one atmospheric layer can be calculated through

$$\tau_A = \tau_A^f + \tau_A^c = \frac{3V_0^f Q_{\text{ext}}^f}{4r_{\text{eff}}^f} + \frac{3V_0^c Q_{\text{ext}}^c}{4r_{\text{eff}}^c} \quad (\text{A.15})$$

$$\delta_A = \delta_A^f + \delta_A^c = \frac{3V_0^f Q_{\text{sca}}^f}{4r_{\text{eff}}^f} + \frac{3V_0^c Q_{\text{sca}}^c}{4r_{\text{eff}}^c} \quad (\text{A.16})$$

$$\mathbf{B}_A^j = \frac{\delta_A^f \mathbf{B}_A^{fj} + \delta_A^c \mathbf{B}_A^{cj}}{\delta_A^f + \delta_A^c} \quad (\text{A.17})$$

We can compute vector $\left[\phi'_x, \varphi'_x, \langle \Psi'_x^j \rangle_{j=1,J} \right]$ for a given parameter by differentiating above equations (A.15)–(A.17). For $x = V_0^f$ as an example:

$$\phi'_x = V_0^f \frac{\partial \tau_A}{\partial V_0^f} = V_0^f \frac{3Q_{\text{ext}}^f}{4r_{\text{eff}}^f} = \tau_A^f \quad (\text{A.18})$$

$$\varphi'_x = V_0^f \frac{\partial \delta_A}{\partial V_0^f} = V_0^f \frac{3Q_{\text{sca}}^f}{4r_{\text{eff}}^f} = \delta_A^f \quad (\text{A.19})$$

$$\Psi'_x = V_0^f \frac{\partial \mathbf{B}_A^j}{\partial V_0^f} = \frac{\delta_A^f}{\delta_A} (\mathbf{B}_A^{fj} - \mathbf{B}_A^j) \quad (\text{A.20})$$

And similarly for $x = r_g^f$, we have

$$\phi'_x = \tau_A^f \left(\frac{r_g^f}{Q_{\text{ext}}^f} \frac{\partial Q_{\text{ext}}^f}{\partial r_g^f} - \frac{r_g^f}{r_{\text{eff}}^f} \frac{\partial r_{\text{eff}}^f}{\partial r_g^f} \right) \quad (\text{A.21})$$

$$\varphi'_x = \delta_A^f \left(\frac{r_g^f}{Q_{\text{sca}}^f} \frac{\partial Q_{\text{sca}}^f}{\partial r_g^f} - \frac{r_g^f}{r_{\text{eff}}^f} \frac{\partial r_{\text{eff}}^f}{\partial r_g^f} \right) \quad (\text{A.22})$$

$$\Psi'_x = \frac{\varphi'_x}{\delta_A} (\mathbf{B}_A^{f,j} - \mathbf{B}_A^j) + r_g^f \frac{\partial \mathbf{B}_A^{sj}}{\partial r_g^f} \quad (\text{A.23})$$

In a similar fashion, we can obtain the vector $\left[\phi'_x, \varphi'_x, \langle \Psi'_x \rangle_{j=1,J} \right]$ for other fine-mode aerosol parameters including τ_A^f , ω_A^f , V_0^f , m_r^f , m_i^f , r_g^f , σ_g^f , and ε^f (as listed in Table 2.2). For coarse-mode aerosol parameters, the derivations are the same with superscript ‘s’ replaced by ‘c’.

We have implemented various aerosol-loading vertical profiles into the testbed, including uniform, exponential-decreasing, and quasi-Gaussian profile shapes. For the uniform profile, aerosols are assumed evenly distributed with height. The layer AOD for the exponential-decreasing profile follows form

$$\int_{+\infty}^z \tau_A(z) dz = \tau_{a0} \exp\left(-\frac{z}{H}\right) \quad (\text{A.24})$$

where τ_{a0} is the columnar AOD, and H is a scale height parameter. The quasi-Gaussian profile is derived from a generalized distribution function [Spurr and Christi, 2014]

$$\tau_A(z) = K \frac{\exp(-\gamma|z - z_{\text{peak}}|)}{[1 + \exp(-\gamma|z - z_{\text{peak}}|)]^2} \quad (\text{A.25})$$

where K is a constant related to τ_{a0} , γ is related to half-width constant, and z_{peak} is the height

having peak loading. Derivatives of layer aerosol optical thickness with respect to these profile parameters (H , γ , and z_{peak}) are also included in order to calculate Jacobians of Stokes vector to these parameters, and the vectors $\left[\phi'_x, \varphi'_x, \langle \Psi'_x^j \rangle_{j=1,J} \right]$ for these derivatives are also shown in Table 2.2.

APPENDIX B

OPTIMIZING SPECIES-SPECIFIED AEROSOL EMISSIONS FROM SATELLITE MEASURED RADIANCES

B.1 Introduction

Tropospheric aerosols play an important role in the Earth's energy budget and hydrological cycle by directly scattering or absorbing solar radiation (direct effect) and indirectly altering the cloud microphysical properties and lifetime through serving as cloud condensation nuclei (indirect effect) [Haywood and Boucher, 2000]. The Intergovernmental Panel on Climate Change [IPCC, 2007] reported direct and indirect aerosol radiative forcing as -0.5 and -0.7 Wm^{-2} , respectively, both with uncertainty of about 100%. Such large uncertainties are attributed not only to a diversity of representations of aerosol microphysical and optical properties across models [Schulz et al., 2006], but also to the uncertainty in the emissions of aerosol particles and aerosol precursors (hereafter aerosol emissions) from both natural and anthropogenic sources. Differences in global aerosol emission estimates, ranging from 22% to over 200% depending on the species, were found among various global chemistry transport models (CTMs) [Textor et al., 2006], highlighting the need to further improve the quantifications of aerosol emissions. At regional scales, the emission inventories have much larger uncertainty [Streets et al., 2003] and often don't resolve the seasonal or monthly variations, making it difficult to model regional climate, air quality and visibility. In addition,

accurate and timely knowledge of aerosol sources is required for use of air quality models for studying impacts of aerosols on human health [[Pope et al., 2009](#)].

Current estimates of aerosol emissions are largely based on the “bottom-up” method that integrates diverse information such as fuel consumption in various industries and corresponding measurements of emission rates for different species [[Streets et al., 2003](#)], economic growth, and the statistics of land use and fire-burned areas [[van der Werf et al., 2006](#)]. While significant progress has been made [[Streets et al., 2006](#)], the “bottom-up” approach has a number of limitations. First, the emission inventory usually has a temporal lag of at least 2 to 3 years, as time is needed to aggregate information from different sources and format them into the emission inventories that are suitable for use in climate models. Second, the temporal resolution of the current emission inventory is usually on monthly to annual scale, which is not sufficient to characterize the daily or diurnal variation of emissions; the aerosol impact on radiative transfer and the variation of cloud properties, however, is often strongly dependent on the time of the day [[Wang et al., 2006](#)]. Third, the spatial resolutions of the bottom-up emission inventories are usually limited by the availability of the ground-based observations, which often lack the spatial coverage for estimating emission in a uniformly fine resolution for regional modeling of aerosol transport. Finally, bottom-up emission inventories may miss important emission sources that are not well documented including emissions from wild fires, volcanic eruptions, and agricultural activities. All these limitations are amplified over the East Asia region because the economic growth in China is so rapid that information needed for bottom-up approach cannot be timely and reliably documented.

To complement information from bottom-up emissions, remote sensing is increasingly used to better quantify aerosol distributions. The satellite observations and/or products can provide information important for the bottom-up estimate of emissions. Examples include the fire products from MODIS, ASTER, and AVHRR sensors that are widely used

for characterizing the biomass burning emissions [*Borrego et al.*, 2008; *van der Werf et al.*, 2006, 2010; *Reid et al.*, 2009]. Alternatively, the satellite observed tracer abundance could be used to constrain bottom-up estimates of aerosol emissions through the inverse modeling; such method is referred to as a ‘top-down’ constraint. Although satellite-based aerosol retrievals have less precision than in situ measurements, studies have shown that they are able to quantify the atmospheric aerosol loading and temporal variations with good agreement and expected accuracy to the ground-based observations [*Levy et al.*, 2010; *Remer et al.*, 2005]. Furthermore, the satellite-based aerosol data, in contrast to the ground-based ones, have much higher temporal resolution across the globe. For instance, the MODIS sensor, aboard on NASA’s both Terra and Aqua satellites, has a surface footprint size of about 1 km at nadir and needs only 1 to 2 days to achieve global coverage. In addition, the joint retrieval of aerosols from diverse satellite sensors enhances the accuracy of satellite aerosol products [*Sinyuk et al.*, 2008], the potential of which have also been shown in the air quality monitoring [*Liu et al.*, 2005; *Wang et al.*, 2010].

Different top-down techniques have been developed to optimally estimate the emissions from satellite observations, which include but are not limited to the following: (a) the use of a scaling factor that is the ratio of observed tracer abundances to the CTM simulated counterparts [*Lee et al.* [2011]; *Martin et al.* [2003a]; *Wang et al.* [2006]]; (b) the use of the local sensitivity of change of tracer concentration to the change of emission [*Lamsal et al.*, 2011; *Walker et al.*, 2010]; (c) the analytical Bayesian inversion method [e.g., *Heald et al.*, 2004]; (d) the adjoint of CTM [e.g., *Muller and Stavrakou*, 2005; *Henze et al.*, 2007, 2009; *Dubovik et al.*, 2008; *Kopacz et al.*, 2009, 2010; *Wang et al.*, 2012]. The first two methods are similar; both assume a linear relationship between model simulated aerosol abundances and emissions. The analytical method is exact but computationally expensive and thus can only constrain emission in the domain-wise or over coarse spatial resolution [*Kopacz et al.*, 2009]. In contrast to the first three approaches, the adjoint approach is designed for

exploiting the high-density of observations to constrain emission with high resolution, as it is able to efficiently calculate gradients of the overall mismatch between observations and model estimates with respect to large sets of parameters (i.e., emissions resolved at each grid box) [Henze *et al.*, 2007].

Several studies have successfully analyzed sources of trace gases using the top-down methods, including CO sources from MOPITT sensor over the Asia [Heald *et al.*, 2004; Kopacz *et al.*, 2009] and over the globe [e.g., Stavrakou and Müller, 2006; Kopacz *et al.*, 2010], CO₂ surface flux from the TES sensor [Nassar *et al.*, 2011], NOx emissions from space-based column NO₂ by several satellite sensors [Lamsal *et al.*, 2011; Lin *et al.*, 2010; Martin *et al.*, 2003a; Muller and Stavrakou, 2005], and SO₂ from SCIAMACHY and OMI sensors [Lee *et al.*, 2011], etc. However, not all emissions of trace gases can be fully constrained with their satellite-based counterpart products, because some trace gases (e.g., SO₂) can react with other gases (e.g., NH₃), to form either liquid or solid aerosols (e.g., (NH₄)₂SO₄). As a result, using measurements of trace gases alone can only provide partial constraints on the emission of the corresponding trace gases.

Ultimately, combined use of measurements of both trace gases and aerosols should provide stronger constraint (than each individual measurement alone) for the emission of aerosols and their precursors including trace gases. Unlike a given trace gas, aerosol has complex chemical composition. Aerosol optical depth (AOD), the only parameter that current satellite remote sensing can provide and is well validated, contains little information on aerosol composition. Consequently, assumption of aerosol composition is often made when using AOD to constrain aerosol models. Examples from previous studies have focused on assimilation of AOD to constrain model AOD [Wang *et al.*, 2004; Zhang *et al.*, 2008; Benedetti *et al.*, 2009], or to estimate PM_{2.5} concentrations [van Donkelaar *et al.*, 2008]. While valuable for forecasts or estimating distribution of aerosols, these studies do not provide direct constraints on aerosol sources. In terms of constraining sources, a recent

study by [Dubovik *et al.*, 2008] constrained aerosol primary sources in single-fine and single-coarse modes respectively from MODIS retrieved fine and coarse mode $0.55\text{ }\mu\text{m}$ AOD by inverting the GOCART aerosol transport model. To overcome the inconsistency of aerosol single scattering properties between CTM and aerosol retrieval algorithm that may compromise the use of satellite AOD to quantitatively invert aerosol emissions, Weaver *et al.* [2007] suggested directly assimilating the satellite observed radiance (such as from MODIS) to improve the CTM (GOCART model) simulation of aerosols. Improved retrieval of AOD and improved estimate of surface PM concentration were also obtained by Drury *et al.* [2008] over the U.S. and Wang *et al.* [2010] over China, when the GEOS-Chem simulated aerosol single scattering properties is used in the retrieval, allowing MODIS radiance to directly constrain the GEOS-Chem columnar mass of aerosols. Built upon this progress, we [Wang *et al.*, 2012] further used MODIS radiance to constrain dust emissions over the East Asia.

In this study, we present a new attempt for the top-down estimate of aerosol emissions through integration of the satellite observation of reflectance and GEOS-Chem Adjoint model. The technique is applied to improve estimates of mineral dust and anthropogenic SO_2 , NH_3 , NOx , BC and OC emissions over China for April 2008, during which ground-based PM_{10} (particulate matter with aerodynamic diameter of $10\text{ }\mu\text{m}$ or less) data is available from a joint China-U.S. dust field experiment [Huang *et al.*, 2010]. This study differs from the past work in that: (i) satellite reflectance (in essence radiance) is used to constrain the emission estimates of aerosol particle and precursors, which eliminates the discrepancy of aerosol optical properties between model simulated and satellite retrieved AOD; (ii) we use a suite of aerosol and gas measurements from satellite sensors and ground-based instruments to independently evaluate our results, and test our hypothesis that temporal variation of AOD at different locations, as characterized by satellite observations, can be a strong constraint for species-specific source estimates if they are combined with the model-based knowledge of

the dominant aerosol sources and the source-receptor relationship at corresponding locations; and (iii) combination of (i) and (ii) will provide the basis and a necessary step forward for future research to simultaneously use both gas and AOD measurements to constrain speciated aerosol emissions.

We present the general structure of our inversion methodology in section B.2, in which we describe the observation constraints and the inversion strategies. The top-down constraints on aerosol emissions over China for the period of April 2008 are presented in section B.3, and evaluated by independent observation acquired from various platforms in section B.4. Interpretation and implications of the results are discussed in section B.5, and section B.6 summarizes this work.

B.2 Observational Constraints and Inversion

Methodology

As shown in Figure B.1, the top-down inversion approach in this study integrates the MODIS radiance/reflectance with the GEOS-Chem (section B.2.1) and its adjoint model (section B.2.2) to optimize aerosol emissions. First, similar to *Wang et al.* [2010], we retrieve the atmospheric aerosol mass and AOD through fitting the calculated radiance based on GEOS-Chem aerosol composition and single optical properties to the MODIS cloud-free radiances (section B.2.3). Second, the retrieved AOD (hereafter retrieved MODIS AOD) from the first step is used as an observational constraint to optimize the aerosol emissions by inverting the GEOS-Chem chemical transport model. The approach aims to improve aerosol emission estimates that ultimately will yield better agreement between model simulated and satellite-observed reflectances. Since the aerosol single scattering properties are exactly the same between the retrieval algorithm and GEOS-Chem (as done in the first step), the

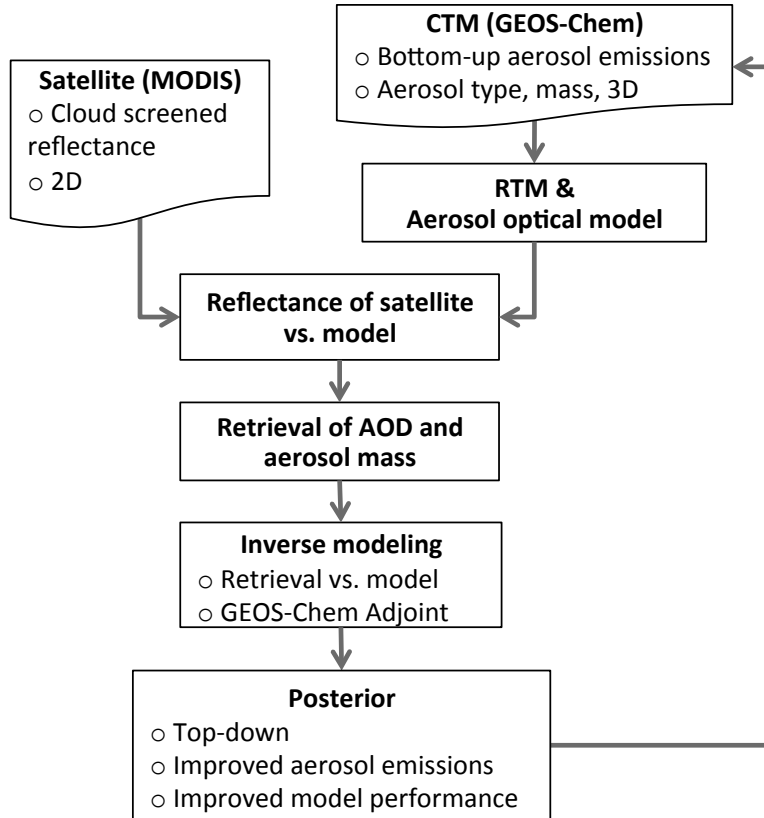


Figure B.1: Flowchart of the proposed top-down inversion framework [Xu *et al.*, 2013].

top-down inversion scheme essentially uses the MODIS radiances (in the form of retrieved AOD) to scale the GEOS-Chem aerosol mass, which in turn are used to optimally adjust the aerosol emissions. The approach here is first demonstrated through a pseudo-observation experiment (section B.2.5) before it is applied to real observations (Section B.3).

B.2.1 GEOS-Chem model

GEOS-Chem [Bey *et al.*, 2001] (www.geos-chem.org) is a global three-dimensional tropospheric chemical transport model driven by assimilated meteorological observations from the Goddard Earth Observing System (GEOS) of the NASA Global Modeling and Assimilation Office. The aerosol simulation in GEOS-Chem includes state-of-science representations of

the major aerosol components: sulfate (SO_4), nitrate (NO_3), ammonium (NH_4), BC, and OC in both hydrophilic and hydrophobic modes, mineral dust in four size bins, and sea salt aerosols in both accumulation and coarse modes. The model couples aerosol and gas-phase chemistry through nitrate and ammonium partitioning, sulfur chemistry, secondary organic aerosol formation, and uptake of acidic gases by sea salt and dust [Park *et al.*, 2004]. Aerosol is removed by dry and wet deposition. Dry deposition in GEOS-Chem follows a resistance-in-series scheme [Wesely, 1989] and accounts for gravitational settling [Seinfeld and Pandis, 2006] and turbulent mixing of particles to the surface. Aerosols are also removed through wet scavenging in convective updrafts as well as the first-order rainout and washout.

GEOS-Chem uses many databases for anthropogenic emissions [van Donkelaar *et al.*, 2008] and biomass burning emissions [van der Werf *et al.*, 2010]. In the current study, the annually anthropogenic emissions of SO_2 and NOx are from INTEX-B EI with the base year of 2006 [Zhang *et al.*, 2009b]. The monthly anthropogenic and biofuel emissions of NH_3 use the TRACE-P EI with the base year of 2000 [Streets *et al.*, 2003]. The monthly anthropogenic fossil fuel and biofuel OC/BC emissions are from Bond EI with base year of 2000 [Bond *et al.*, 2007]. The monthly biomass burning emission for SO_2 , NH_3 , NOx , OC, and BC use GFED2 EI with the base year of 2007 [van der Werf *et al.*, 2010]. The mineral dust entrainment and deposition (DEAD) scheme [Zender *et al.*, 2003a] that was modified to combine with the GOCART topographic source function [Ginoux *et al.*, 2001; Fairlie *et al.*, 2007] is used to simulate the prior emitted dust fluxes (hereafter the modified DEAD scheme). We run version 8-02-01 of GEOS-Chem for the full chemistry simulation during the period of April 2008 with $2^\circ \times 2.5^\circ$ horizontal resolution and 47 vertical levels.

AOD at wavelength λ in each layer is calculated from the sum of AODs of each component i assuming external mixing:

$$\tau_\lambda = \sum_{i=1}^n \frac{3M_i Q_{\text{ext}i}}{4\rho_i r_{\text{eff}i}} = \sum_{i=1}^n M_i \beta_{\text{eff}i} \quad (\text{B.1})$$

where n is the number of aerosol components, M_i is aerosol mass concentration of component i , $Q_{\text{ext}i}$ is extinction efficiency factor at wavelength λ calculated with Mie theory, ρ_i is aerosol mass density, $r_{\text{eff}i}$ is particle effective radius, and $\beta_{\text{eff}i} = \frac{3Q_{\text{ext}i}}{4\rho_ir_{\text{eff}i}}$ is the mass extinction efficiency. We account for the hygroscopicity of aerosol particles, as all parameters in the above equation are functions of relative humidity for hydrophilic aerosol components. We use the updated aerosol size distribution and refractive index from [Drury et al. \[2010\]](#) and [Wang et al. \[2010\]](#) to calculate $Q_{\text{ext}i}$ and $r_{\text{eff}i}$ in a Mie code.

B.2.2 GEOS-Chem adjoint modeling

The adjoint of the GEOS-Chem model was developed specifically for inverse modeling of aerosol (or their precursors) and gas emissions [[Henze et al., 2007, 2009](#)], and it is continuously improved and maintained by the GEOS-Chem Adjoint and Data Assimilation Working Group and its users (http://wiki.seas.harvard.edu/geos-chem/index.php/GEOS-Chem_Adjoint). The strength of the adjoint model is its ability to efficiently calculate model sensitivities with respect to large sets of model parameters, such as aerosol emissions at each grid box. These sensitivities can serve as the gradients needed for inverse modeling of aerosol emissions. Recent studies have used the GEOS-Chem adjoint with satellite observations to constrain sources of species such as CO [[Kopacz et al., 2009, 2010; Jiang et al., 2011](#)], CH₄ [[Wecht et al., 2012](#)], and O₃ [[Parrington et al., 2012](#)] to diagnose source regions for long-range transport [[Henze et al., 2009; Kopacz et al., 2011](#)], and to provide guidance on future geostationary observations of surface air quality [[Zoogman et al., 2011](#)].

In the GEOS-Chem inverse modeling framework, aerosol emissions are adjusted using a vector of control parameters σ that are the logarithm of emission scaling factors for aerosol emissions: $\sigma = \ln(\mathbf{E}/\mathbf{E}_a)$, where \mathbf{E} and \mathbf{E}_a are updated and prior aerosol emission vectors,

respectively. The model response function J , or cost function, is formulated following the four-dimensional variational (4D-Var) technique:

$$J(\boldsymbol{\sigma}) = \frac{1}{2} \sum_{\mathbf{c} \in \Omega} [\mathbf{c}(\boldsymbol{\sigma}) - \mathbf{c}_{\text{obs}}]^T \mathbf{S}_{\text{obs}}^{-1} [\mathbf{c}(\boldsymbol{\sigma}) - \mathbf{c}_{\text{obs}}] + \gamma \frac{1}{2} [\boldsymbol{\sigma} - \boldsymbol{\sigma}_a]^T \mathbf{S}_a^{-1} [\boldsymbol{\sigma} - \boldsymbol{\sigma}_a] \quad (\text{B.2})$$

where \mathbf{c} is the vector of simulated aerosol concentration in four-dimensional spatial and temporal observation space Ω , \mathbf{c}_{obs} is the vector of observed aerosol concentration, \mathbf{S}_{obs} is the observation error covariance matrix for \mathbf{c}_{obs} , γ is a regularization parameter, $\boldsymbol{\sigma}_a$ is prior control parameters, and \mathbf{S}_a is the error covariance matrix of $\boldsymbol{\sigma}_a$. Overall, the cost function is a measure of specific model response, the minimum value of which balances the objectives of minimizing model mismatch of the observations while ensuring the specified prior emissions remain within approximate range described by \mathbf{S}_a . The optimization seeks the optimal $\boldsymbol{\sigma}$ that minimizes the cost function J iteratively through a numerical quasi-Newton algorithm, the L-BFGS-B algorithm [[Byrd et al., 1995](#)], which requires the supplement of the cost function and its gradient with respect to the emission scaling factors calculated with GEOS-Chem adjoint model.

B.2.3 Constraints from Satellite Radiances

The observational constraints in this study are MODIS reflectances from both Terra and Aqua satellites, from which four-dimensional mass concentrations of six aerosol species (namely, sulfate (SO_4), nitrate (NO_3), ammonium (NH_4), black carbon (BC), organic carbon (OC), and mineral dust) have been derived with the GEOS-Chem model using the retrieval algorithm presented by [Wang et al. \[2010\]](#). Key to this algorithm are: (a) a database of time-dependent local 0.65 and 2.1 μm surface reflectance ratio that are derived from samples of the MODIS dark-pixel reflectance data in low AOD conditions (i.e. dynamic lower envelope method), (b) an assumption that the simulated CTM aerosol is unbiased

in composition and vertical distribution shape but possibly largely biased in total mass or optical depth, and (c) a linearized radiative transfer model (VLIDORT [Spurr, 2006]) that computes the top-of-atmosphere (TOA) reflectance and its Jacobian sensitivity to the column AOD using the GEOS-Chem single aerosol optical properties and the solar-earth-sensor geometries of the coincident MODIS scene. With above (a), (b), and (c), Wang *et al.* [2010] retrieved two unknowns (i.e., AOD at 0.65 μm and surface reflectance at 2.13 μm) from two MODIS observed quantities (i.e., 0.65 and 2.13 μm TOA reflectance) by seeking the minimum differences between GEOS-Chem and MODIS reflectance. Based on (b), mass concentrations of individual aerosol species at each MODIS overpassed grid cell are updated by applying the AOD scaling factors (ratios of retrieved AOD to GEOS-Chem AOD at 0.65 μm) and are used as observational constraints for optimizing aerosol emissions.

Figures B.2a and B.2b show the two-month averages of the 0.65- μm AOD retrieved using the approach by Wang *et al.* [2010] and the MODIS collection 5 products. Although sharing similar pattern of spatial distributions, their retrieved AOD is quantitatively smaller and are in better agreement with the AERONET AODs (figure B.2c–d). According to the evaluation of the retrieved AOD against these AERONET AODs, we found the uncertainty is generally less than 20%, which we subsequently use to quantify the observation error in the inverse modeling optimization.

GEOS-Chem simulated aerosol composition over Asia is shown by multiple studies to have large underestimation in BC, and equivalent or larger underestimation of OC mass and overestimation of sulfate aerosol mass [Heald *et al.*, 2005; Fu *et al.*, 2012], which suggests that the mass fraction of highly absorbing (BC) and highly scattering (OC and sulfate) fine mode aerosols may have far less biases (as compared to the relative bias in OC mass only). Consequently, no significant biases are assumed for: (a) the GEOS-Chem simulated fraction of coarse mode (dust) aerosol mass, and (b) the GEOS-Chem simulated aerosol single scattering albedo. While (b) is important to ensure an unbiased retrieval of AOD,

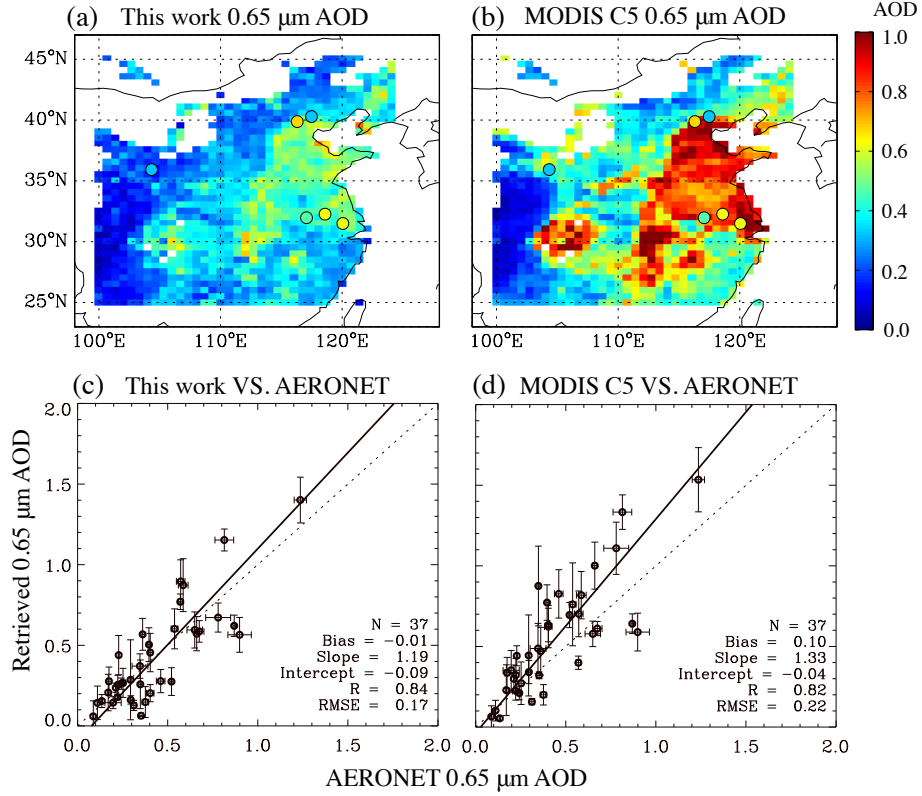


Figure B.2: The $0.65\text{ }\mu\text{m}$ AOD retrieved by [Wang *et al.*, 2010] compared with the MODIS operational collection 5 AOD products. (a) and (b) are their two-month averages for the period of April–May, 2008. The correspondong two-month averages of $0.65\text{-}\mu\text{m}$ AOD collected at size AERONET sites are color-coded as circles. (c) and (d) are their scatterplot against AOD observed from AERONET sites indicated on the above map. [Figure adopted from Wang *et al.*, 2010].

(a) supports that the GEOS-Chem simulated dust AOD fraction is likely unbiased, both of which support the use of AOD scale factors derived from MODIS for constraining emission of coarse-mode dust and fine-mode aerosols. Admittedly, any model bias in modeled AOT fraction for each individual species can lead to a corresponding bias (of the same sign) in the adjoint modeling results for individual emission. Quantification of such bias is not possible for the present study owing to the lack of aerosol composition data in China.

B.2.4 Selection of emissions for optimization

The inversion scheme and the MODIS-based constraints, as described in the preceding sections, are combined to constrain the aerosol emissions over the Eastern Asia for the period of April 2008. The modeled emission parameters that most significantly influence the discrepancy between simulation and observations are selected and spatially constrained. Specifically, those model parameters (or control parameters) represent six emitted tracers, as listed in Table B.2, which include emissions of SO₂, NH₃, and NOx, BC, and OC from anthropogenic sources, and mineral dust. Bottom-up inventories (and an online mobilization scheme for dust) are used as *a priori* estimates, corresponding magnitudes and geographic distributions of which are shown in Table B.2 and Figure B.6, respectively. The temporal extent of the optimization window is selected to be reconcilable with the temporal variability of the bottom-up emission. We set optimization window of a month for those trace gases and carbonaceous emission tracers; while dust emission tracers are constrained daily in a separate optimization run following approach by [Wang et al. \[2012\]](#). Both optimizations assimilate hourly observations during the adjoint simulation.

The 4D-Var technique in the optimization requires background error covariance statistics for each control parameter. We specify the priori error for those emission tracers based on characterized spatial and temporal averaged uncertainties for those inventories [[Zhang et al., 2009b](#); [Bond et al., 2007](#); [Zender et al., 2003a](#)], but with larger values to reflect the possibly large local aerosol emission uncertainties in the bottom-up inventories. The uncertainty for SO₂ emission estimate is believed to be smaller than those for NH₃ and NOx, while uncertainties of other tracers could be even larger [[Textor et al., 2006](#); [Zhang et al., 2009b](#)]. Therefore, we set relative error of 50% for SO₂, 100% for NH₃ and NOx, 200% for BC, OC, and dust sources. Lacking information to fully construct a physically representative prior error covariance matrix, a regularization parameter γ is introduced in the cost function

to balance the contribution of model error and source error, with a value (here $\gamma = 1000$) selected using the L-curve technique [Hansen, 1998]. Moreover, in order to test the impact of those specified uncertainties on the optimization, we run a case with an arbitrary prior error of 100% for all emission tracers, and present the results in Table B.3.

B.2.5 Sensitivity test with pseudo AOD observations

We first conduct a pseudo experiment to assess: (1) the concept that temporal variations and geophysical location of AOD, when interpreted with GEOS-Chem model, can yield information about change regarding aerosol composition and emissions, and (2) the sensitivity of the inversion results to the assumption that GEOS-Chem simulated relative composition or single scattering albedo of aerosol is unbiased. The experiment has three steps: (a) GEOS-Chem simulation with standard bottom-up EIs are first conducted to obtain prior aerosol composition and $0.65 \mu\text{m}$ AOD for the period from April 5 to 11 of 2008; (b) Pseudo-observations of AOD are created by perturbing the following emissions (relative to bottom-up EIs) in GEOS-Chem: +20% for SO_2 , NH_3 , and NOx , -40% for dust, and zero for BC and OC (Table B.1); (c) These pseudo-observations of AOD in the dark surface region (red box in Figure B.3a), twice per day, respectively at the Terra and Aqua overpass daytime, are subsequently used as truth to constrain emissions using the GEOS-Chem adjoint-based inversion.

The degree to which the inversion can correct for species-specific errors in the emissions is assessed in these sensitivity tests by comparing the optimized aerosol emissions from (c) can then be evaluated against the truth, or the perturbed emissions in (b). Figure B.3 shows the distribution of relative changes in posterior emissions from the 6th iteration with respect to the prior bottom-up emissions for each species; the overall changes over the China are shown in Table B.1. By the 6th iteration, the cost function reduced by 50%; further

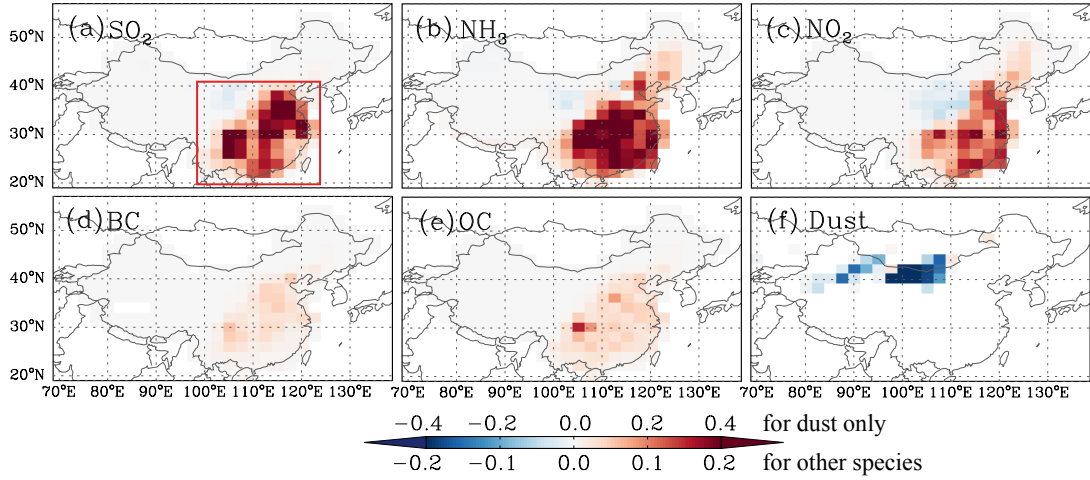


Figure B.3: Relative changes in posterior aerosol emissions from *a priori* in the pseudo-observation experiment. Six panels are respectively for anthropogenic emissions of SO_2 , NH_3 , NO_x , BC , and OC , and mineral dust from both natural and anthropogenic sources. The red box in panel (a) indicates the region where AOD observations are selected. [Figure adopted from [Xu et al., 2013](#)]

iterations yielded negligible additional decreases. The posterior emissions for SO_2 and NH_3 , which increased by 14% from the prior, are close to the “truth” (20%). NO_x emissions were increased by 8%, a smaller change than SO_2 and NH_3 . Dust emissions reduced by 26% percent in the inversion, approaching the true values of -40% . BC and OC emissions were increased by 2% and 3%, which are close to the truth of 0.

Overall, this sensitivity study demonstrates that the inversion is capable of resolving the sign, spatial distribution, and the bulk of the true perturbations for the emissions of each species. Meanwhile, we also note that the adjoint inversion could transfer (somewhat marginal) errors from one tracer to another, such as increases in BC and OC emission as a result of significant underestimations in the prior SO_2 , NH_3 , and NO_x emissions, reflecting errors due to assumptions related to unbiased GEOS-Chem aerosol composition. We can also assume that similar aliasing would occur in attempts to distinguish the impacts of co-located precursor emissions of scattering particles (e.g., SO_2 and NO_x from power plants),

Table B.1: Prior, posterior, and perturbed aerosol emissions over China in the pseudo experiment.

| Tracer | E_{prior} (Gg/Month) | $E_{\text{posterior}}$ (Gg/Month) | $E_{\text{posterior}}/E_{\text{prior}}$ (%) | $E_{\text{perturbed}}/E_{\text{prior}}$ (%) |
|-----------------|----------------------------------|--------------------------------------|--|--|
| SO ₂ | 520.8 | 592.0 | 113.7 | 120 |
| NH ₃ | 219.3 | 249.2 | 113.7 | 120 |
| NOx | 338.8 | 365.3 | 107.8 | 120 |
| BC | 23.3 | 23.8 | 102.3 | 100 |
| OC | 39.7 | 41.1 | 103.4 | 100 |
| Dust | 2301 | 1697 | 73.7 | 60 |

although additional tests would be necessary to assess whether or not differences in the timescales (and thus transported length scales) over which these emissions impact AOD would allow their sources to be separated. Long-range transport of dust appears to have less influence on the inversion because: (a) except dust, there are little (other) emissions in dust source regions; (b) a sudden increase of AOD in downwind regions can be interpreted by GEOS-Chem due to the dust transport, and this increase can be used by GEOS-Chem adjoint as constraint to optimize the dust emission.

B.3 Inversion Results

With the feasibility of the approach demonstrated in section B.2.5, we apply the approach to MODIS radiance data in April 2008. The emissions that result from each iteration during the optimization enable GEOS-Chem to produce a different set of AOD values that converge to the observational constraints. Figure B.4a shows the geographic distribution of GEOS-Chem AOD at 0.65 μm , simulated with prior aerosol emissions, averaged coincidentally with retrieved daily MODIS AOD (Figure B.4c) during April 2008. While the prior model simulation captures the overall spatial pattern of AOD with larger values over eastern China, it has a slight underestimation over the southwestern China but an overwhelming

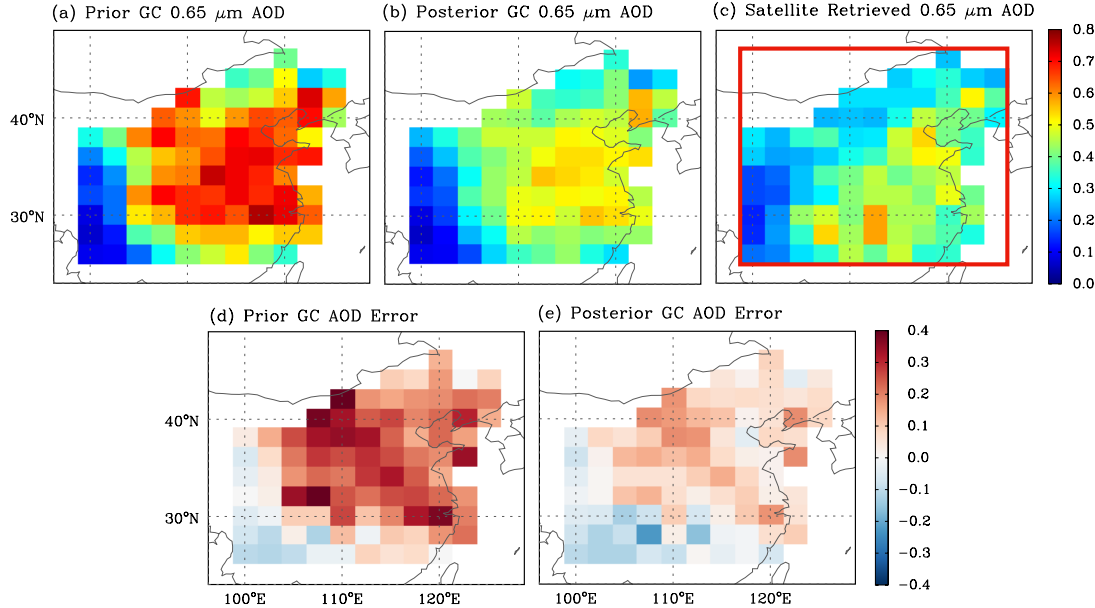


Figure B.4: Comparison of the prior (a) and posterior (b) GEOS-Chem (GC) simulation of 0.65 μm AOD with the AOD at the same wavelength retrieved from MODIS reflectance using GEOS-Chem aerosol optical properties (c) averaged for the period of April 2008. Satellite retrievals with 10 km by 10 km at nadir are aggregated to GEOS-Chem grid cells; and the model AOD are sampled coincidentally with those retrievals. Panel (d) and (e) respectively show the difference of prior and posterior simulated from the satellite retrieved AODs. The red box in panel (c) indicates the region where AOD observations are selected. [Figure adopted from [Xu et al., 2013](#)]

overestimation elsewhere, when compared to the retrieved AOD from MODIS radiance (Figure B.4d). The optimization is expected to adjust aerosol emissions to reduce those differences. Following the experiment design described in section B.2.4, we find that after 6 iterations of the GEOS-Chem forward and adjoint runs, the cost function is reduced by about 60%, and further iterations yield negligible reductions in the cost function. Therefore, the aerosol emissions adjusted from the 6th iteration are selected as the final optimal results. As shown in Figure B.4b and B.4e, the posterior GEOS-Chem AOD that are simulated with the optimized aerosol emissions are in much better agreement with their counterparts retrieved from MODIS reflectance, which is also reflected by the cost function reduction and confirms the effectiveness of the adjustment in top-down emissions.

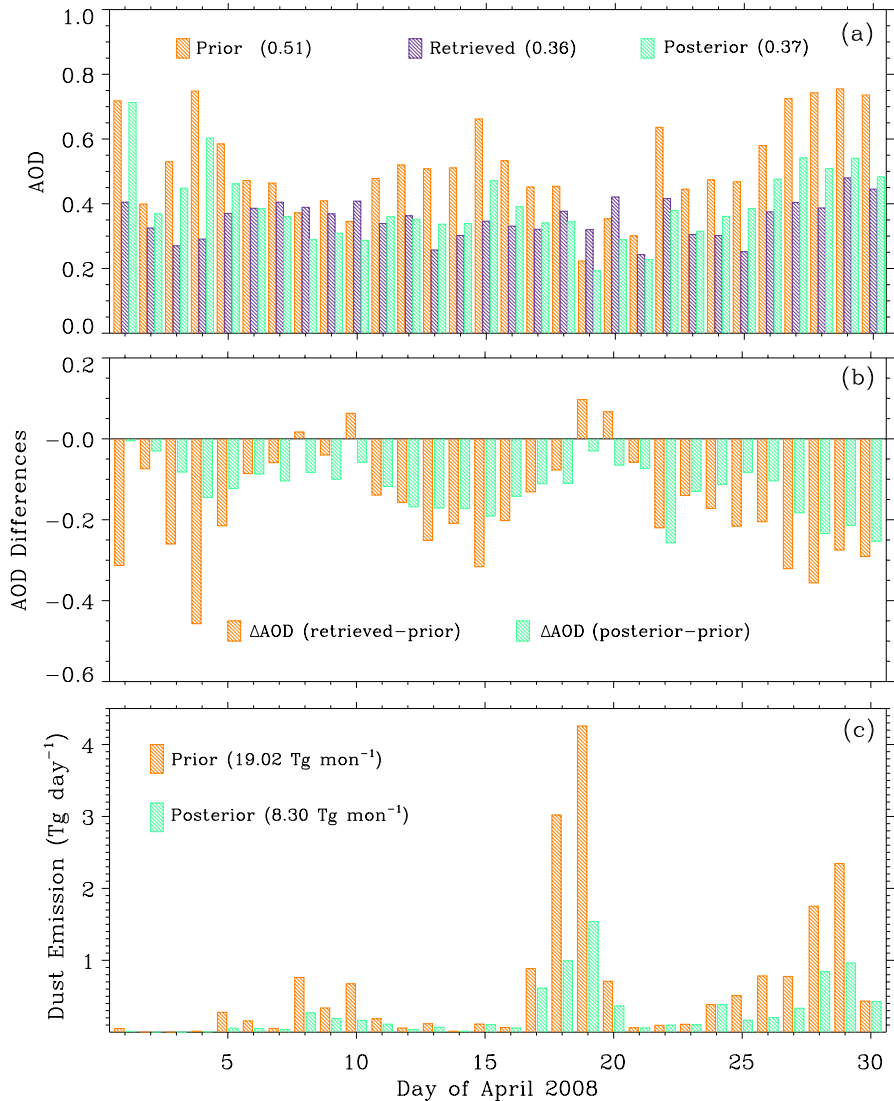


Figure B.5: (a) Time series of the spatially averaged daily MODIS AOD retrievals (purple) for April 2008 over the Eastern China, compared by the prior (orange) and posterior (green) spatial averaged daily GEOS-Chem AOD that are sampled in the MODIS AOD temporal-spatial space. (b) Time series of the expected daily AOD adjustments (orange) that are the differences between MODIS AOD and the prior GEOS-Chem AOD and their real adjustments (green) that are the differences of posterior from prior GEOS-Chem AOD. (c) Time series of the prior (orange) and posterior (green) daily dust emissions over China for April 2008. [Figure adopted from [Xu et al., 2013](#)]

Table B.2: List of prior and posterior aerosol emissions in China during April 2008.

| Tracer | Bottom-Up | | | | | Top-Down | | |
|-----------------|--|------------------------------|-----------|--------------|------------------------|------------------------|--|-------------------|
| | E_{prior} (TgMon $^{-1}$) | <i>a priori</i> error (%) | Inventory | Base year | Temporal resolution | Optimization window | $E_{\text{posterior}}$ (TgMon $^{-1}$) | ΔE (%) |
| SO ₂ | 2.60 | 50 | INTEX-B | 2006 | Annual | Monthly | 1.73 | -33.5 |
| NH ₃ | 1.10 | 100 | INTEX-B | 2000 | Annual | Monthly | 0.72 | -34.5 |
| NOx | 1.69 | 100 | INTEX-B | 2006 | Monthly | Monthly | 1.38 | -18.8 |
| BC | 0.11 | 200 | Bond07 | 2000 | Monthly | Monthly | 0.10 | -9.1 |
| OC | 0.21 | 200 | Bond07 | 2000 | Monthly | Monthly | 0.18 | -15.0 |
| Dust | 19.02 | 200 | DEAD | Online | Hourly | Daily | 8.30 | -56.4 |

The convergence of the model simulation to the MODIS AOD retrievals is also indicated in the AOD daily variability. Figure B.5a shows the daily variations of the AOD spatially averaged for available MODIS retrievals (purple) over the eastern China areas within the red box in Figure B.4c, and the coincidental GEOS-Chem simulation prior and posterior to the aerosol emission optimization (orange and green, respectively). The prior model produce overestimated AODs for most days during the month. After top-down adjustments to the aerosol emissions, such overestimation of the AOD is reduced in total over the course of the month. As shown in Figure B.5b, the real changes of the modeled daily AOD during the optimization (green bars), or equivalently, the differences of the posterior from the prior are consistent with the expected changes, i.e., the differences of the MODIS retrievals from the prior model simulation. It is noted that the posterior AODs has larger departure from the observation than the prior on a few days. This reflects that monthly-scaled emissions are not perfectly capturing the daily variation of emission.

Emissions of SO₂, NH₃, NOx, BC, and OC from anthropogenic sources are optimized monthly and rescaled over each individual 2° by 2.5° grid cell of China for the month of April 2008. The prior and posterior (optimized) emissions of these tracers are respectively shown in left and middle columns of Figure B.6, in which the relative changes of these emissions in the optimization are also included in the right column. Overall, the optimization yields an overwhelming reduction for all emission tracers, even though some local increases

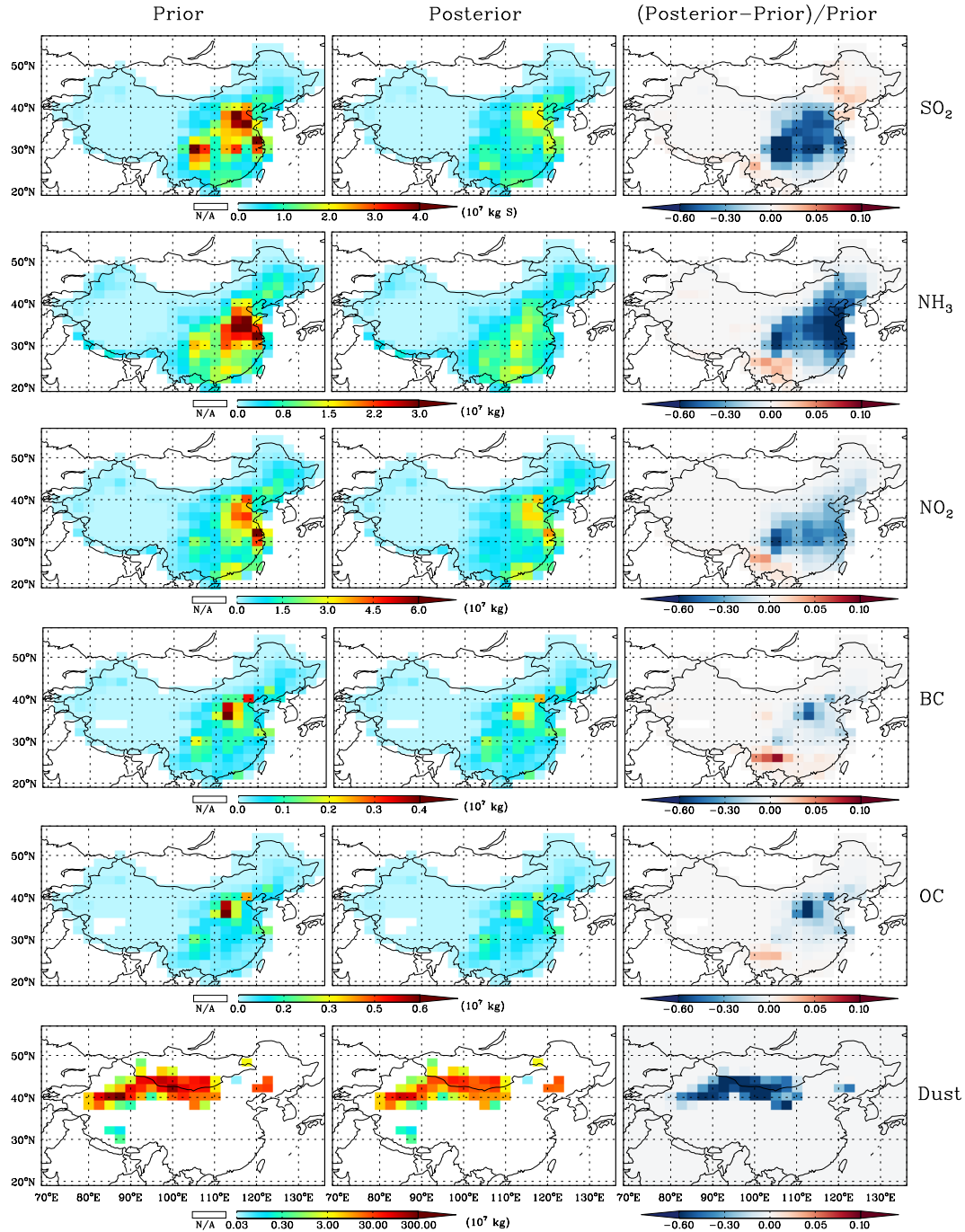


Figure B.6: The prior (or bottom-up based, left column), optimized (or top-down constrained, middle column) aerosol emissions over China for the period of April 2008, and their relative differences (right column). Six rows from top to bottom are respectively for anthropogenic emissions of SO_2 , NH_3 , NO_x , BC, and OC, and mineral dust from both natural and anthropogenic sources. [Figure adopted from Xu et al., 2013]

are found. As expected, such adjustment in the constrained aerosol emissions is consistent with the changes in GEOS-Chem AOD before and after optimization, as aerosol loadings usually positively respond to the aerosol emissions. Quantitatively, anthropogenic emissions over China continent for the study period are changed by -33.5% for SO_2 from 1.302 to 0.866 Tg, -34.5% for NH_3 from 1.096 to 0.718 Tg, -18.8% for NOx from 1.694 to 1.375 Tg, -9.1% for BC from 0.11 to 0.10 Tg, and -15.0% for OC from 0.205 to 0.175 Tg (see Table B.2). The largest reduction occurs sharply in the central regions of the Eastern China, corresponding to the region where the largest AOD are adjusted to the MODIS retrievals. Small increases of emitted anthropogenic sources of gases and carbonaceous particles are found over the southwestern China, which can be explained as the response for the underestimation of AOD in the model simulation over these regions (Figure B.4a, d).

The mineral dust emissions from both anthropogenic and natural sources are optimized daily. The adjoint has no leverage to increase the dust emissions over grid cells having zero dust emission in the priori estimate identified by the modified DEAD scheme. Thus, the posteriori dust source region remains un-shifted as shown in Figure B.6 (bottom panels), which is reasonable because the expansion or shrinkage of desert regions is unlikely to extend beyond the grid size (2° by 2.5°) of this study [Zender *et al.*, 2003a; Fairlie *et al.*, 2007]. The total amount of the optimized dust emissions for April 2008 over China is 8.3 Tg, reduced by 56.4% from the modified DEAD module simulation of 19.02 Tg. Such reduction indicates an overestimation in the prior emissions of dust, especially over Gobi deserts that are located in the Northwestern China and the southern Mongolia. Wang *et al.* [2012] presented a similar result, but only for a dust event that occurred in the later portion of our study time period. Figure B.5c illustrates the time series of the prior and optimized daily total dust emission. Two sharp peaks of the dust emissions indicate the occurrences of strong dust storms after April 15. Such large temporal variation in the daily scale requires the optimization of dust emission on the daily basis.

Table B.3: Test of the sensitivity of optimization with respect to prescribed a priori error.

| Tracer | Case 1 | | Case 2 | |
|-----------------|------------------------------|-------------------|------------------------------|-------------------|
| | <i>a priori</i> error (%) | ΔE (%) | <i>a priori</i> error (%) | ΔE (%) |
| SO ₂ | 50 | -33.5 | 100 | -33.7 |
| NH ₃ | 100 | -34.5 | 100 | -34.4 |
| NOx | 100 | -18.8 | 100 | -18.8 |
| BC | 200 | -9.1 | 100 | -9.1 |
| OC | 200 | -15.0 | 100 | -15.0 |

An additional case with specified error of 100% for all the anthropogenic emission tracers is conducted to examine the sensitivity of those specified error to the optimization. Table B.3 shows the relative change in optimized emissions for two different scenarios. Less than 0.5% of difference in the optimized emissions is found, which means the uncertainty in a priori emission could have much smaller impact on the optimization than the observational constraints.

B.4 Results Evaluations

Because direct measurements of the aerosol emissions are few over China, we assess the optimized sources by comparing the GEOS-Chem posterior simulated aerosol mass concentrations and AOD with the independent observations from various sources. The evaluation datasets include: (1) AERONET AOD observations [Holben *et al.*, 1998] over nine sites; (2) Level 3 MISR daily AOD products [Kahn *et al.*, 2005; Martonchik *et al.*, 2009]; (3) Level 3 SO₂ [Krotkov *et al.*, 2006; Lee *et al.*, 2009] and Level 2 NO₂ [Bucsela *et al.*, 2006] retrievals from the Ozone Monitoring Instrument (OMI); (4) surface mass concentration of sulfate-nitrate-ammonium (SNA) aerosol particles over Qingdao, China; and (5) surface PM₁₀ over two sites close to dust source region [Ge *et al.*, 2010].

B.4.1 Comparison with AERONET AOD

We first evaluate the prior and posterior GEOS-Chem 0.55 μm AOD against the AERONET AOD at 0.55 μm that are interpolated from AODs at 0.44 and 0.67 μm based on the Angstrom exponent. Three-hour averaged values of available AERONET AOD, centered by the model output time are used to compare with the model AOD over the grid cells locating the AERONET sites. The scatterplots shown in Figure B.7 are the comparisons for nine stations over China, South Korea, and Japan representing different aerosol types. The first three stations, i.e., (a) Zhangye, (b) SACOL, and (c) Jingtai, which are located over rural regions in the south boundary of Gobi deserts and have little influence from anthropogenic emissions, are representative sites for dust aerosol [Ge *et al.*, 2010]. The next three sites, (d) Beijing, (e) Xinglong, and (f) Heifei, are located in anthropogenic source regions. The last three sites, (g) Noto, (h) Shirahama, and (i) Gwangju_K, are located over Japan and South Korea, the downwind regions of China emissions. Those last six stations are affected not only by the local anthropogenic emissions but also by the long-range transported aerosols from the upwind regions. Indeed, those three categories of stations are respectively located in the upwind, central, and downwind of regions having the observational constraints.

The prior GEOS-Chem simulation (shown in the red scatter panels) overestimates the AERONET AOD for all the sites except Beijing. The negative bias of model AOD at Beijing is likely owing to the model coarse resolution, which fails to resolve heavy local urban pollution. The geographic area of urban Beijing is about 1300 km^2 (<http://en.wikipedia.org/wiki/Beijing>), less than 3% of the area of a GEOS-Chem grid cell. Thus, the local pollution signal is smeared in the model grid box. Moreover, Beijing and Xinglong are in the same model grid cell, but AERONET AOD over Xinglong is much smaller than that over Beijing site (as later shown as circles on the maps of Figure B.8a-c). As Beijing site is difficult to represent in the GEOS-Chem at 2° by 2.5° resolution, we

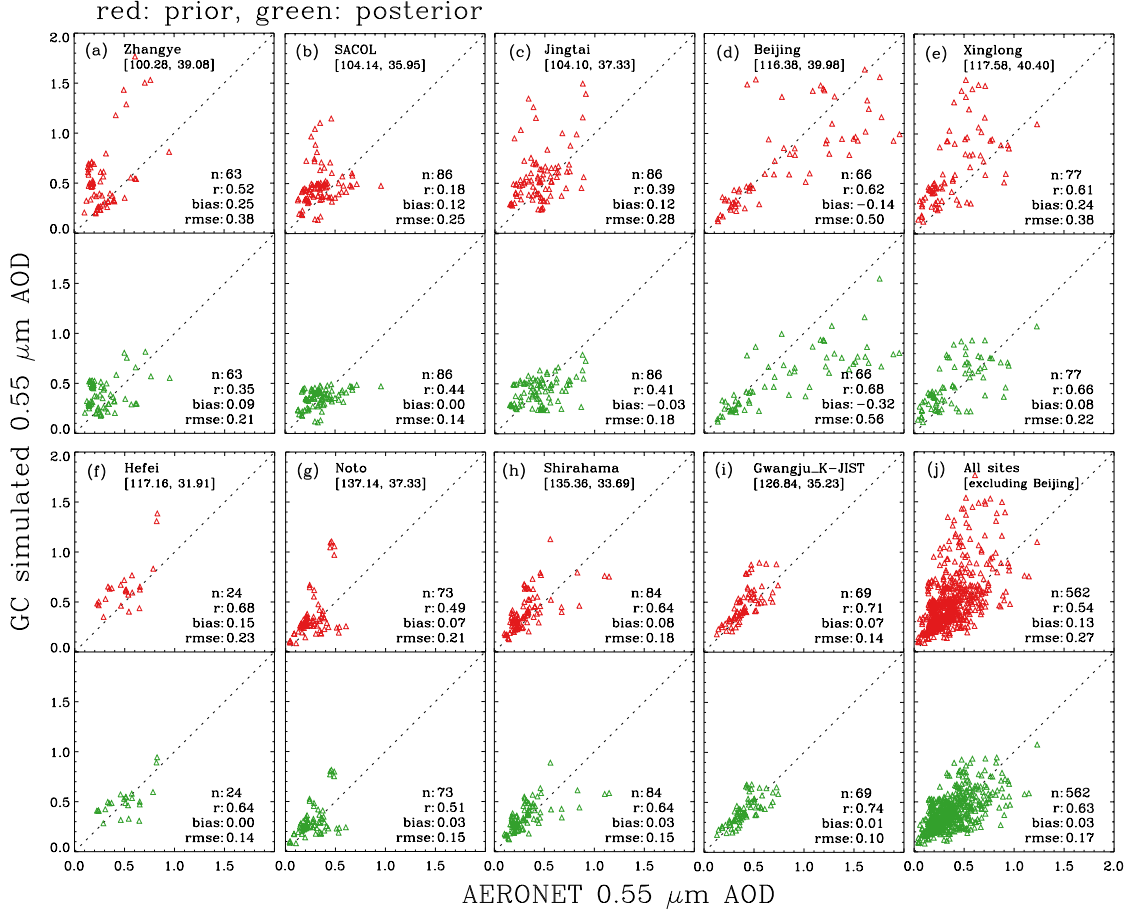


Figure B.7: (a – i) Scatterplots of GEOS-Chem AOD versus AERONET AOD at $0.55 \mu\text{m}$ prior (red scatters) and posterior (green scatters) to the aerosol emission optimization over nine stations. AERONET AODs are 3-hour averages following the GEOS-Chem output frequency. (j) The overall comparison for eight AERONET sites excluding Beijing. Also shown are the number of valid sampled pairs (n), correlation coefficients (R), bias, and root-mean-square-error (rmse).

exclude Beijing site in our further analysis. GEOS-Chem AOD from the posterior aerosol emissions are in more agreement with the AERONET AOD (shown in the green scatter panels), as indicated by reduced bias and root-mean-square-error (rmse) over all the other sites and increased correlation coefficients (R) for most sites. The overall comparison (Figure B.7j) shows the correlation coefficient increases from 0.54 to 0.63, and the bias (rmse) declines from 0.13 (0.27) to 0.03 (0.07).

B.4.2 Comparison with MISR AOD

We re-grid the Level 3 daily MISR 0.55 μm AOD from the 0.5° by 0.5° resolution to GEOS-Chem 2° by 2.5° grid cells and take monthly average for April 2008, the geographic distribution of which are shown in Figure B.8c. High AOD values are found over the eastern China and the northwestern desert regions, which are associated to the anthropogenic pollution primarily from the industry and wind-blown mineral dust, respectively. The monthly sun-photometer AOD values at the same wavelength show good agreements with the MISR AOD over all the AERONET sites except Beijing where the significant local urban pollution exists.

The monthly averages of prior and posterior GEOS-Chem 0.55 μm AOD mapped in Figure B.8a–b are sampled coincidentally to the MISR AOD. A comparison with the MISR AOD shows GEOS-Chem simulation with prior aerosol emissions overestimates AOD over both the desert and industrial regions. The posterior simulation is slightly more in agreement with MISR AOD. To facilitate the comparison of model with MISR AOD, we also include, as Figure B.8d, the scatterplots of the AOD for each GEOS-Chem grid cell with values larger than 0.2 by considering the larger retrieval uncertainty in the low AOD conditions [Kahn et al., 2005, 2010]. While the correlation coefficients remain about the same, both absolute bias and rmse are reduced about 30%.

B.4.3 Comparisons with OMI columnar SO_2 and NO_2

The improvement in the optimized aerosol emissions is also exhibited in the comparison of simulated trace gases to the satellite retrievals from OMI. The GEOS-Chem SO_2 simulations are assessed with OMI Level 3 daily products of planetary boundary layer (PBL) SO_2 column gridded with 0.25° by 0.25° resolution. We average the OMI SO_2 columnar retrievals into GEOS-Chem 2° by 2.5° grid cells and take the monthly average for comparison, which are

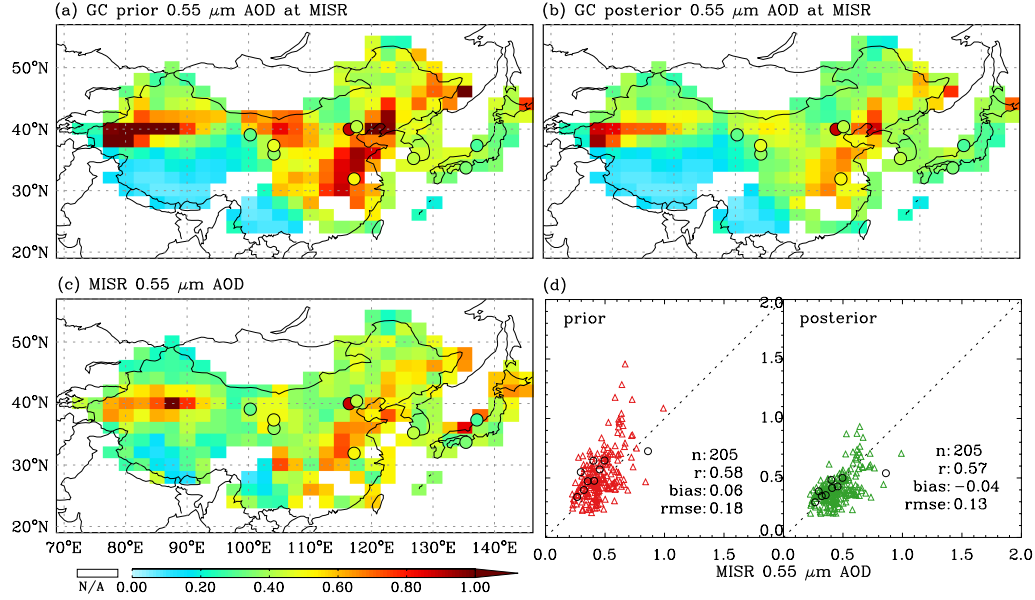


Figure B.8: Comparison of the prior and posterior GEOS-Chem simulation of $0.55 \mu\text{m}$ AOD with the level 3 MISR $0.55 \mu\text{m}$ AOD for the period April 2008. (a) The prior GEOS-Chem $0.55 \mu\text{m}$ AOD that are sampled coincidentally with MISR AODs for the period of April 2008. Also overlaid circles are the monthly AOD averages at $0.55 \mu\text{m}$ observed from the nine AEORNET sites shown in Figure B.7. (b) Same as (a) but for the monthly average of posterior GEOS-Chem AOD. (c) Monthly average of the Level 3 daily MISR $0.55 \mu\text{m}$ AOD. (d) Scatter plot the GEOS-Chem AOD versus the MISR AOD before (red scatters) and after optimization (green scatters), in which each point indicates an AOD pair over a model grid cell with value over 0.2. Also shown are the statistics including number of sampled pairs (n), correlation coefficient (R), bias and root-mean-square-error (rmse). Comparisons of the monthly GEOS-Chem AOD versus AERONET AOD are also included as the black circles; each circle indicates an AOD pair over an individual site. [Figure adopted from [Xu et al., 2013](#)]

shown in Figure B.9c. Figure B.9a and B.9b show model prior and posterior SO_2 column that are coincidentally sampled with OMI retrievals. Figure B.9d illustrates the quantitative analysis for OMI SO_2 retrievals larger than $1.0 \times 10^{16} \text{ molec cm}^{-2}$. With the optimized emission estimates, the bias and RMSE are reduced from 0.81 and 0.61 to -0.28 and 0.38 ($\times 10^{16} \text{ molec cm}^{-2}$), respectively, along with an increase of correlation coefficient from 0.68 to 0.73.

We evaluate the model simulation of NO_2 with OMI Level 2 products of NO_2 tropo-

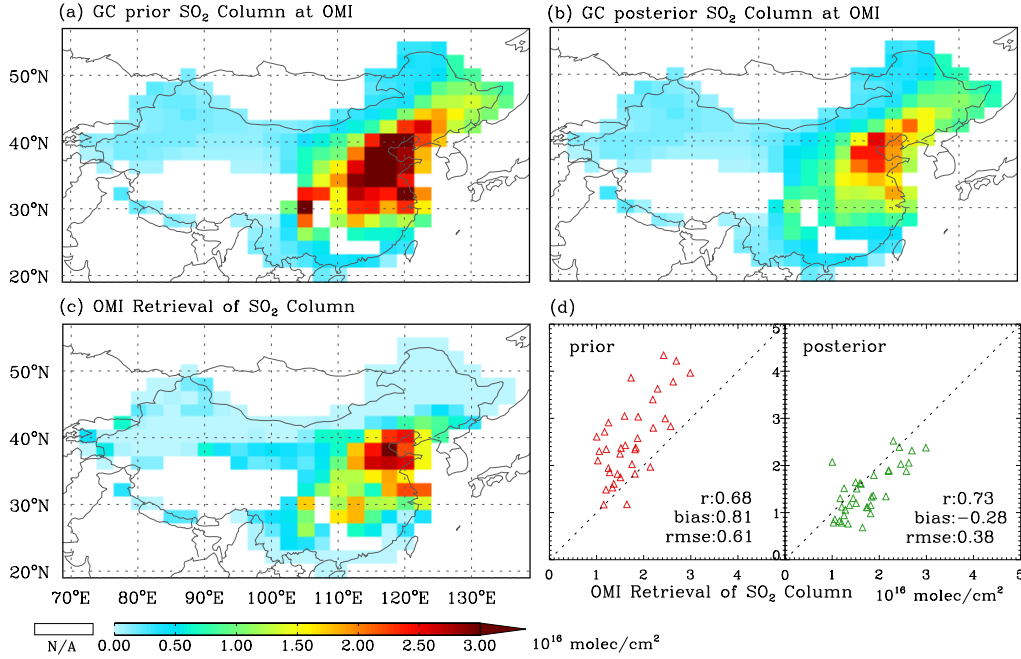


Figure B.9: Same as figure B.8 but for comparison of the GEOS-Chem SO₂ simulation with OMI column SO₂ retrievals for the period of April 2008. The OMI planetary boundary layer (PBL) column SO₂ from the Level 3 daily products with 0.25° by 0.25° resolutions are aggregated into GEOS-Chem grid cells.

spheric column over 0.25° by 0.25° grid cells. Recent studies suggested that the uncertainty in OMI NO₂ tropospheric column retrievals is about 40% with an about 15% positive systematical bias [Boersma *et al.*, 2008; Celarier *et al.*, 2008]. Following Lin *et al.* [2010], we apply a factor of 0.85 to OMI NO₂ retrievals in our comparison to correct the bias. Figure B.10 shows the comparison of GEOS-Chem NO₂ columns with re-gridded OMI NO₂ retrievals. Similarly, we also perform the quantitative analysis, as in Figure B.10d, for OMI NO₂ column retrievals larger than 3.0×10^{15} molec cm⁻². While the correlation coefficient remains about the same, the bias (RMSE) is reduced from 1.50 (1.65) to 0.03 (1.51) (units: 10^{15} molec cm⁻²) after constraining aerosol emissions.

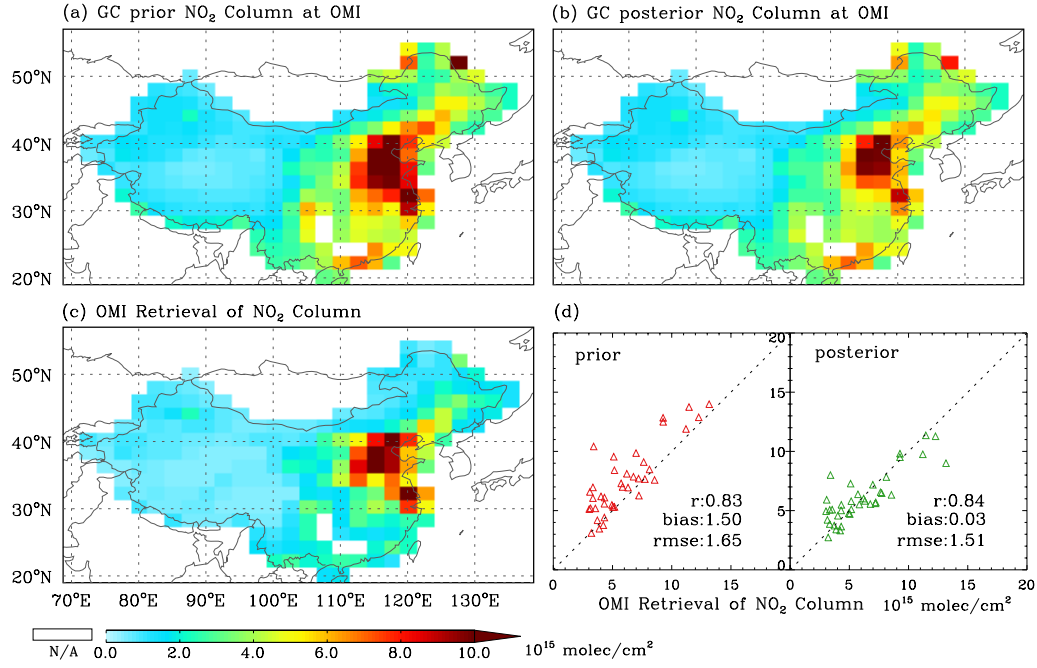


Figure B.10: Same figure B.8 but for comparison of the GEOS-Chem NO₂ simulation with OMI column NO₂ retrievals for the period of April 2008. The OMI tropospheric column NO₂ from Level 2 daily products with 0.25° by 0.25° resolutions are aggregated into GEOS-Chem grid cells.

B.4.4 Comparisons with near-surface aerosol mass concentrations

The accuracy of the sulfate-nitrate-ammonium (SNA) aerosol simulation is in part determined by the representation of the emissions of SO₂ and NOx and NH₃, and hence GEOS-Chem simulations with constrained emissions should provide overall an improved simulation of SNA. Figure B.11 shows the comparison of daily near-surface SNA mass concentration from the prior and posterior GEOS-Chem simulations with measurements over Qingdao (120.34° E, 36.06° N), China. The error bars for the GEOS-Chem curves indicate the diurnal standard deviation. An overestimation in the prior model surface SNA simulations is found when comparing with observed counterparts, which shows a bias of $14.28 \mu\text{g m}^{-3}$, RMSE of $21.84 \mu\text{g m}^{-3}$, and correlation coefficient of 0.46. Such bias is significantly reduced to $0.34 \mu\text{g m}^{-3}$ in the simulation with top-down constrained emissions,

along with a 50% decrease in RMSE and a 28% increase in correlation coefficient.

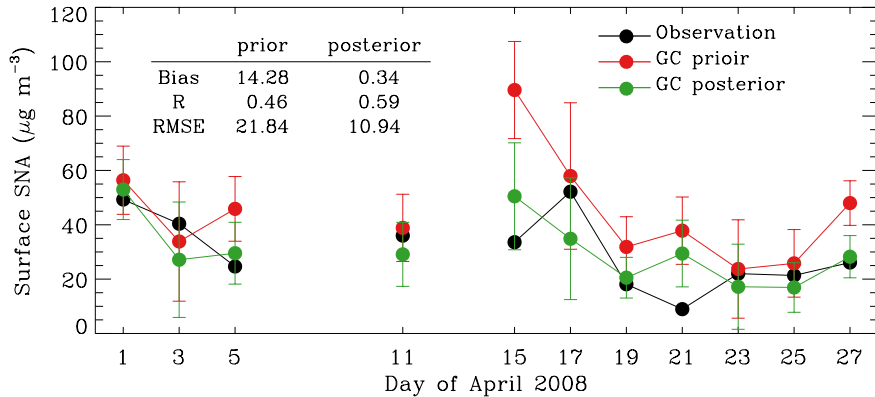


Figure B.11: Comparison of the GEOS-Chem surface mass concentration of sulfate-nitrate-ammonium (SNA) aerosols with ground-based observations over Qingdao (120.34° E, 36.06° N), China. Discontinuity in time series is due to missing or quality filtered observations.

The mass concentration over or near the dust source regions where the anthropogenic emissions are small is most sensitive to the dust mass loading, and thus can be an indicator of the dust emissions in the first order. Figure B.12 shows the prior and posterior GEOS-Chem surface PM₁₀ mass concentration compared with the ground-based measurements from the 2008 China-U.S. joint field experiment [Ge et al., 2010; Huang et al., 2010] over two the AERONET sites in Figure B.7a-b, i.e., Zhangye (100.28° E, 39.08° N) and SACOL (204.14° E, 35.95° N), which are located on the downwind boundaries of the Gobi deserts. Based on the availability of the measurements data, comparisons are for the period of 15–30 April 2008. The measured surface PM₁₀ shows a strong daily variation. A strong dust event during 18–20 April can be found over both stations with PM₁₀ exceeding $400 \mu\text{g m}^{-3}$. Two additional dust events with PM₁₀ over $400 \mu\text{g m}^{-3}$ occurred during 24–26 and 29–30 April. The prior simulation generally captures the daily variation pattern but significantly overestimates the surface PM₁₀ for those dust events; prior simulated PM₁₀ reaches up to around $3000 \mu\text{g m}^{-3}$ over Zhangye and $1000 \mu\text{g m}^{-3}$ over SACOL for the

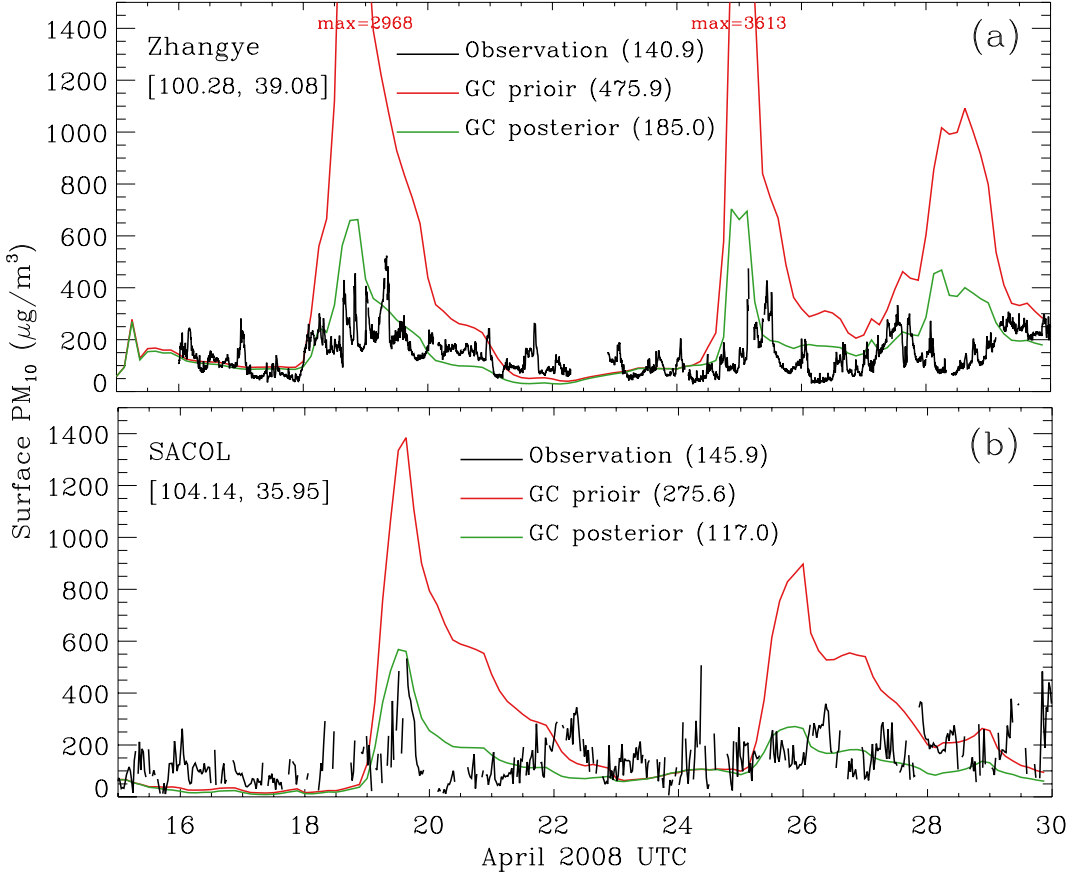


Figure B.12: Time serial plot of the GEOS-Chem simulated surface PM_{10} concentrations by prior (red) and posterior (red) aerosol emissions compared with the *in situ* measured PM_{10} (black) over Zhangye (a) and SACOL (b) stations for 15 – 30 April 2008; also shown are the average values over same the period. Discontinuity in time series is due to missing or quality filtered observations.

dust events during 18–20 and 24–26 April 2008. The two-week averages show the prior simulation overestimates PM_{10} a factor of 2 over Zhangye and a factor of 1 over SACOL in the magnitude. After optimization, the relative biases in the PM_{10} simulation are reduced to about 25%. Moreover, the comparison of the time series of the PM_{10} also shows that the model value with top-down emissions has much better agreement with the measurements in terms of temporal variation.

B.4.5 Evaluation summary

A summary of evaluations of the prior and posterior model simulations is illustrated in Figure B.13 using a Taylor diagram [Taylor, 2001]. Taylor diagram provides a statistical summary of the model performance in terms of correlation coefficients (R), centralized root-mean-square difference (RMSD), and ratio of standard deviations between model and observations (or normalized standard deviation, NSD). The latter two quantities reflect how well model captures the temporal or/and spatial variation of observations. In the Taylor diagram, cosine of polar angles represents R, and radius (dotted-contour) indicates NSD. Thus, the reference point (black circle) where R and NSD are unity represents observations, and the distance (dashed-contour) of certain point from which indicates the RMSD. Considering that the Taylor diagram itself is not able to show the statistical bias, we use different colors for each data points to indicate their respective relative biases. The data points labeled from 1 to 6 indicate comparisons between model and observations of (1) AERONET AOD at $0.55\text{ }\mu\text{m}$, (2) MISR $0.55\text{ }\mu\text{m}$ AOD, (3) OMI retrievals of SO_2 Column, (4) OMI retrievals of NO_2 Column, (5) surface concentration of SNA over Qingdao, and (6) surface concentration of PM_{10} over Zhangye and SACOL, respectively. Square and circles represent the evaluations for prior and posterior GEOS-Chem simulations, respectively.

It should be noted that the NSD between prior GEOS-Chem simulated and measured surface PM_{10} during the China-U.S. joint field campaign is about 6.5 (and R of 0.45) that are significantly beyond the range of this Taylor diagram. Consequently, the square point of number 6 is not shown in the diagram. It is clear from the Taylor diagram that the circular points (posterior simulation) are generally closer than the square points (prior simulation) to the reference point and to the unity curve of NSD, and have remarkably decreased bias. Evaluations with all those independent observations indicate a notable improvement in the model simulation, reflecting a better estimate of aerosol emissions.

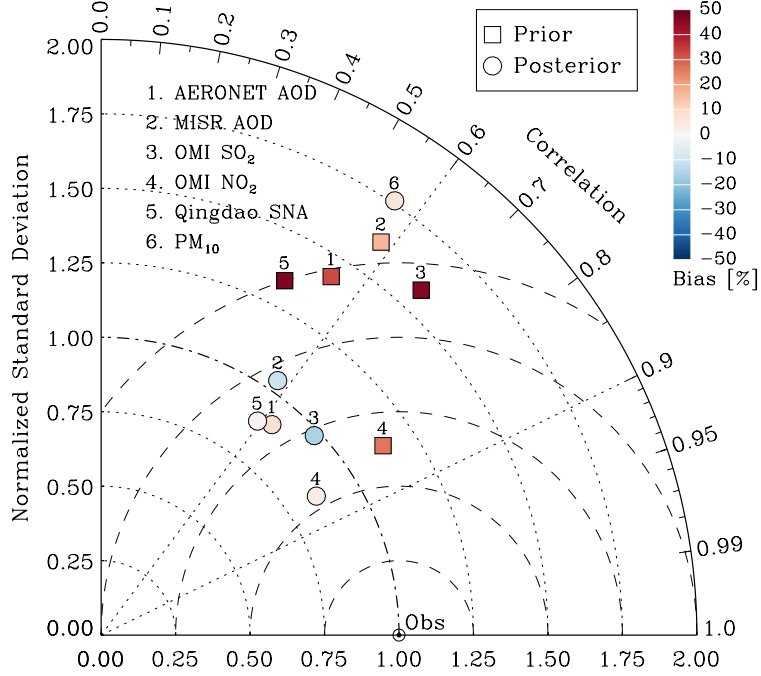


Figure B.13: Taylor diagram for the model evaluations before (squares) and after (circles) optimization when comparing against (1) AERONET AOD at $0.55\text{ }\mu\text{m}$, (2) MISR $0.55\text{ }\mu\text{m}$ AOD, (3) OMI column SO₂, (4) OMI column NO₂, (5) surface SNA concentrations at Qingdao site, and (6) surface PM₁₀ concentrations measured at Zhangye and SACOL sites. The color coded on each point indicates the relative bias. It should be noted that the ratio of standard deviations and correlation coefficient between prior GEOS-Chem simulated and measured surface PM₁₀ over Zhangye and SACOL are 6.5 and 0.45, which makes the point number 6 for the prior simulation far beyond the range of this Taylor diagram.

B.5 Implications of Results

Interpretation of our inversion results can be from two different perspectives. First, if assuming that bottom-up anthropogenic emissions are the best estimates for their base years (mostly 2006), the reduction in the top-down emissions over China for April 2008 may indicate a decrease of emissions for April from 2006 to 2008. This conjecture is supported by the finding of significant decrease of AOD from 2006 to 2008 over the eastern China, shown both in the MODIS and MISR Level 3 gridded products (Figure B.14), if we assume

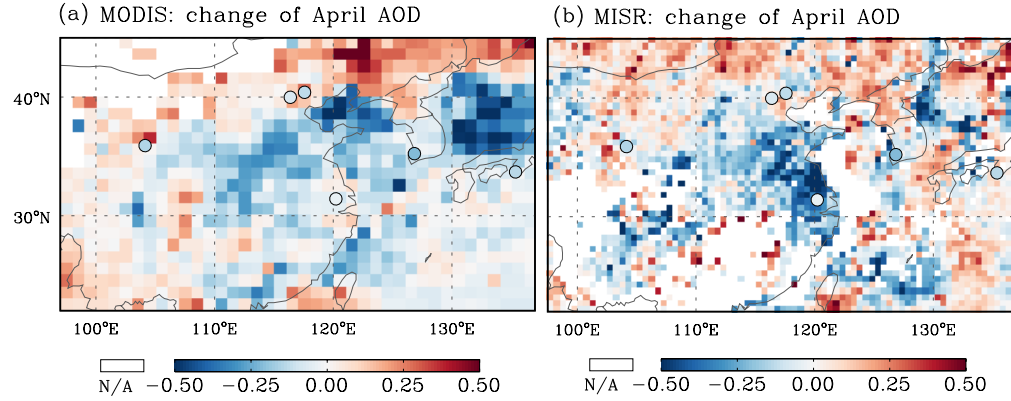


Figure B.14: Change of April monthly $0.55\text{ }\mu\text{m}$ AOD from 2006 to 2008 from MODIS (a) and MISR (b) Level 3 daily products. [Figure adopted from [Xu et al., 2013](#)]

that the impact on AOD of meteorological differences between the two years is smaller than the differences in emissions. Furthermore, a slight increase of AOD over the Southeastern China (Figure B.14) is also found to be consistent to the increase in the top-down emission estimates (Figure B.6). In contrast to the first interpretation, the second one is that the difference of actual emissions between 2008 and their base year (2006) are smaller than the magnitude of adjustments in the optimization, and hence our results imply that the priori bottom-up emissions might be artificially overestimated. We further elucidate those two points below with a literature survey (data are summarized in Table B.4).

B.5.1 SO₂

The INTEX-B inventory by [Zhang et al. \[2009b\]](#) reported an annual production of 31.02 Tg from anthropogenic sources over China. A decrease trend of China SO₂ emissions from 2006 to 2008 has been found based on bottom-up estimates by [Lu et al. \[2010\]](#) from 33.2 to 31.3 ($\sim 5.8\%$ decrease) Tg yr⁻¹ and by China [Ministry of Environmental Protection \[2009\]](#) (hereafter referred to MEP-2008) from 25.9 to 23.2 Tg yr⁻¹ ($\sim 10.4\%$ decrease). With OMI SO₂ retrievals, [Lu et al. \[2010\]](#) found the dramatic reduction of SO₂ emissions

over the northern China for the same period. Similar to this study, *Lu et al.* [2010] also presented that the reductions is more significant over the Eastern China. They attribute some reduction to the widespread installation of flue-gas desulfurization devices in power plants, which is enforced by the China government since 2006. Evidences for the reduction trend of SO₂ emission also include the reduction of SO₂ column from 2006 observed by both SCIAMACHY and OMI satellite sensors [*Lu et al.*, 2011]. With the same SCIAMACHY and OMI SO₂ retrievals, *Lee et al.* [2011] obtained top-down estimates of China SO₂ emissions, which are lower by 50% for SCIAMACHY and 30% for OMI than the INTEX-B inventory. Thus, the reduction of 33.5% in the top-down China SO₂ emissions of this work can be interpreted by the joint contribution of a decrease trend and a possible overestimation in INTEX-B bottom-up inventory.

B.5.2 NH₃

The NH₃ emissions over China have not changed much since 2000, as confirmed by the REAS inventory [*Ohara et al.*, 2007]. Our study shows an overall decrease of 34.5% in the optimized from the TRACE-P 2000 inventory [*Streets et al.*, 2003], which may indicate an overestimation in the TRACE-P inventory. As shown in Table B.4, the total amount of the constrained NH₃ emission (0.72 Tg Mon⁻¹) for April 2008 is quite close to a recent bottom-up estimates (0.71 Tg Mon⁻¹) by *Huang et al.* [2012]. *Huang et al.* [2012] also pointed out that the TRACE-P 2000 inventory significantly overestimates the NH₃ emission by applying an overestimated emission factor across the whole country.

B.5.3 NOx

Lin et al. [2010] constrained Chinese anthropogenic emissions of NOx in July 2008 with tropospheric NO₂ retrievals from GOME-2 and OMI instruments. They found the top-down

Table B.4: Comparisons for annually (Tg yr^{-1}) and/or for April only (Tg Mon^{-1}) estimates of Chinese aerosol emissions during 2006 and 2008.

| Tracer | Emission inventories | 2006 | | 2006 | |
|---------------|---|--------|-------|---------------------|-------|
| | | Annual | April | Annual ^a | April |
| SO_2 | INTEX-B [<i>Zhang et al., 2009b</i>] | 31.02 | 2.37 | - | - |
| | China MEP-2008 | 25.89 | - | 23.21 | - |
| | <i>Lu et al. [2010]</i> | 33.2 | - | 31.3 | - |
| | This work | - | 2.60 | 22.69 | 1.73 |
| NH_3 | TRACE-P [<i>Streets et al., 2003</i>] | 13.6 | 1.10 | - | - |
| | <i>Huang et al. [2012]</i> | 9.8 | 0.71 | - | - |
| | This work | - | 1.10 | 8.91 | 0.72 |
| NOx | INTEX-B [<i>Zhang et al., 2009b</i>] | 20.83 | 1.63 | - | - |
| | <i>Lin et al. [2010]</i> | - | - | 22.34 | - |
| | This work | - | 1.69 | 17.60 | 1.38 |
| BC | INTEX-B [<i>Zhang et al., 2009b</i>] | 1.81 | 0.12 | - | - |
| | <i>Qin and Xie [2012]</i> | 1.55 | - | 1.61 | - |
| | <i>Lu et al. [2011]</i> | 1.63 | - | 1.68 | - |
| | <i>Zhao et al. [2013]</i> | 1.60 | - | 1.60 | - |
| | This work | - | 0.11 | 1.51 | 0.10 |
| OC | INTEX-B [<i>Zhang et al., 2009b</i>] | 3.22 | 0.19 | - | - |
| | <i>Lu et al. [2011]</i> | 3.42 | - | 3.37 | - |
| | <i>Zhao et al. [2013]</i> | 2.90 | - | 2.80 | - |
| | This work | - | 0.21 | 2.92 | 0.18 |

^aOur annual top-down estimates (Tg yr^{-1}) are based on the monthly variation of the INTEXT-B inventory.

emissions are (10–15%) lower than the *a priori* near Beijing (in agreement with results from *Mijling et al. [2009]*), in the northeastern provinces and along the east coast; yet they exceed the *a priori* over many inland regions. Overall, they presented a best top-down estimate of annual NOx production is 6.8 Tg N, or 22.34 Tg NO₂, which is slightly higher than the *a priori*. While the change in NOx emission over China remains controversy, the 18.8% difference of posterior NOx emissions from the bottom-up still lies in the 31% uncertainty of the inventory [*Zhang et al., 2009b*]. We argue bottom-up NOx estimate from INTEX-B inventory could have a possible overestimation.

B.5.4 BC and OC

Major emitting sectors of BC and OC are coal and biofuel combustion by industry, residential, and transportation activities. The trend of BC and OC emissions in China during recent years are controlled by the balance between decrease in emission factor which is pertain to improved technology and increase in coal and fuel consumptions. According to MEP-2008 [*Ministry of Environmental Protection, 2009*], the annual smoke emission in China decreased by about 17.2% from 2006 to 2008. While BC and OC emissions estimated by *Lu et al.* [2011] and *Zhao et al.* [2013] remain almost same between 2006 and 2008, *Qin and Xie* [2012] reported a 3.8% increase. The top-down BC emission is 0.10 Tg mon^{-1} (or 1.509 Tg yr^{-1} based on the monthly variation in INTEX-B inventory), which is smaller than that in INTEX-B, but close to estimates of 1.61 Tg yr^{-1} by *Qin and Xie* [2012] and 1.68 Tg yr^{-1} by *Lu et al.* [2011]. In terms of China OC emission estimates for 2008, *Lu et al.* [2011] suggested a slightly larger value (3.37 Tg yr^{-1}) while *Zhao et al.* [2013] indicated a smaller value (2.8 Tg yr^{-1}) than INTEX-B (3.22 Tg yr^{-1}). Our OC emission estimate (0.18 Tg mon^{-1} or 2.92 Tg yr^{-1}) is within their reported range. It is noted that the uncertainty for OC emissions is reported to be very large: 258% in INTEX-B [*Zhang et al., 2009b*], -43% to 80% by *Lu et al.* [2011], and -42% to 114% by *Zhao et al.* [2013].

B.5.5 Mineral dust

The ~50% reduction in the posterior dust emission estimates suggests the use of DEAD mobilization scheme with GOCART source function possibly tends to produce a systematic positive bias over the Taklimakan and Gobi deserts regions over the northwestern China, even it works reasonably for the United States [*Fairlie et al., 2007*]. Similar results have been also found in top-down dust emission estimates by MODIS aerosol retrievals [*Wang et al., 2012*], and constrained dust emissions by surface PM measurements [*Ku and Park, 2011*].

Such overestimation by the dust mobilization scheme is also reflected through comparison GEOS-Chem AOD (as in Figure B.7) and surface PM₁₀ concentration (as in Figure B.12) with *in situ* measurements near the dust source regions.

B.6 Summary

This study presents a two-stage inversion scheme to explore the capacity of using satellite radiance for inversion of species-specific aerosol emissions. Firstly, we prepare the observational constraints of AOD using an advanced aerosol retrieval algorithm, which integrates the GEOS-Chem aerosol optical properties to the MODIS observed radiance [Wang *et al.*, 2010]. Secondly, the adjoint of the GEOS-Chem chemical transport model is applied to statistically optimize aerosol emission estimates using these AOD retrievals. Thus, the MODIS radiances are essentially used to optimize the estimates of the emitted aerosol tracers and precursors.

We illustrate our concept first with an idealized numerical experiment, and subsequently demonstrate the feasibility and practicability of the proposed scheme by applying it to optimize aerosol emission inventories over China during April 2008. Emissions of SO₂, NH₃, NOx, BC and OC from anthropogenic sources, which significantly influence the aerosol simulation, are selected to be constrained at a spatial resolution of 2° by 2.5° and a monthly temporal resolution. Mineral dust production from combined natural and disturbed sources are optimized at the same spatial resolution but with a daily temporal resolution. Independent observations from both satellite remote sensing and ground-based observations are used to assess the inversion results through their comparisons with relevant GEOS-Chem simulations using prior and posterior emission estimates.

The inversion yields posterior best estimates of 1.73 Tg for SO₂, 0.72 Tg for NH₃, 1.38 Tg for NOx, 0.10 Tg for BC, and 0.18 for OC from anthropogenic sources, and

8.3 Tg for combined natural and disturbed mineral dust. These show notable decreases from their counterparts in the bottom-up inventories in amount (or percentage decrease): 0.87 Tg (33.5%) for SO₂, 0.38 Tg (34.5%) for NH₃, 0.32 Tg (18.8%) for NO_x, 0.01 Tg (9.1%) for BC, and 0.03 Tg (15.0%) for OC. The total amount of the mineral dust emission is reduced by 56.4% from 19.02 Tg simulated by the DEAD mobilization module. The distribution of emission scaling factors exhibits strong spatial variation for those anthropogenic-emitted tracers and considerable temporal variation for mineral dust. The use of top-down constrained emissions remarkably reduces the discrepancy between GEOS-Chem simulation and observational AOD constraints, in both spatial and temporal variation features.

Resulting posterior estimates of emissions are evaluated with independent AOD observations from surface sites (AERONET) and satellite (MISR), SO₂ and NO₂ column retrievals from satellite (OMI), and surface SNA and PM₁₀ concentrations from ground-based measurements. While the prior simulation over China generally shows overestimation, the use of posterior emissions significantly enhances the consistency between simulations and those independent observations. The statistical analysis of those comprehensive comparisons summarized in the Taylor diagram shows an overall reduced bias and root-mean-square difference along with increased correlation coefficient, further confirming the improvements in the posterior simulation and the effectiveness of the presented top-down scheme.

We attribute the differences between prior and posterior aerosol emissions to the change of emitted amount from the base year of those bottom-up inventories to the study period and/or the under/over-estimations in those inventories. Through comparisons with emissions over China reported by recent studies, we find that our inversion results are consistent with following finding:

- Anthropogenic SO₂ emissions over China has been decreased by 5–10% from 2006

to 2008;

- Anthropogenic BC/OC emissions may be slightly reduced;
- Anthropogenic emissions of SO₂ and NOx reported in the INTEX-B and NH₃ from TRACE-P inventories could have been artificially overestimated;
- The DEAD mobilization scheme combined with GOCART dust source function, even works well over the United State [*Fairlie et al.*, 2007], seems to simulate mineral dust surface fluxes with a systematic positive bias.

As a first attempt to invert species-specific emissions with satellite radiance, this study has a number of limitations. Those limitations may impact the uncertainty in posterior emissions, which is supposed to be smaller than uncertainty characterizing either a priori or observational constraints [*Rodgers*, 2000]. While quantification of these is beyond the demonstrative purposes of this paper, we present a qualitative discussion as follows. First, in the stage of aerosol retrieval, we presume aerosol composition is unbiased, and contains errors only in the total amount. As the model inevitably has bias associating aerosol types, improvement of this assumption over regional to global scale can be obtained from innovative satellite measurements. Indeed, the radiance observations have potential information on the aerosol composition. For example, the spectral behavior of the radiance is used to discriminate smoke from mineral dust particles[*King et al.*, 1999; *Kaufman et al.*, 2002]. Radiances measured from multi-viewing-angle are sensitive to aerosol particle size and nonsphericity [*Martonchik et al.*, 2009]. Temporal variation and geographical location can also yield information about aerosol composition. For example, increase of AOD in semi-arid region may reflect the increase of dust, while change of AOD in the Eastern Asia may reflect the increase of industrial emission. Hence, as showed in this study, a combined use of the model-based knowledge of the dominant aerosol sources and the

source-receptor relationship together with the satellite-based temporal variation of AOD at different locations can be a strong constraint for species-specific source estimates. Second, this study also assumes the sole cause of the radiance difference (or the AOD difference) is due to the uncertainty in aerosol emissions. However, other processes can contribute to the difference, e.g. aerosol transport, wet/dry deposition, diurnal variation, prescribed aerosol physical and optical properties, and errors in the meteorological fields and radiative transfer calculation, etc. The third assumption is related to the error covariance matrices that are specified as diagonal with errors based upon literature (but that themselves may have uncertainty). To properly address these issues in future, a logical next step would be to assimilate multiple-spectral and/or multi-angle satellite radiance to the CTM. Furthermore, errors in the processes including emission, transport, and deposition and radiative transfer, should be reasonably characterized and included in the optimization.

The top-down inversion scheme using GEOS-Chem adjoint inverse modeling is a powerful tool to include observational constraints from different platforms for timely updating aerosol emissions. There is also a need of using combined tracer gas and aerosol measurements to simultaneously constrain the aerosol emissions and gas precursors. Encouraging results presented in this study reveal the potential of using aerosol observations from MODIS and MISR, SO_2 and NO_2 from OMI and other sensor, such as SCIAMACHY, in the inversion. Inclusion of those observations will undoubtedly add more information to the optimization of emission.

B.7 Acknowledgements

We thank Jianping Huang for providing the surface PM_{10} data, the AERONET team in NASA GSFC for data services, the HCC of University of Nebraska for computational resources. This research is supported by the NASA Radiation Sciences Program (for Glory

mission) managed by Hal H. Maring, NASA Atmospheric Composition Program managed by Richard E. Eckman, and NASA New Investigator Program as well as a NASA Earth and Space Science Fellowship (to Xiaoguang Xu), both managed by Mingying Wei. This appendix has been published as an article in *Journal of Geophysical Research – Atmospheres* [[Xu et al., 2013](#)].

APPENDIX C

ABBREVIATIONS AND ACRONYMS

| | |
|------|---|
| AE | Ångström Exponent |
| AOD | Aerosol Optical Depth |
| BRDF | Bidirectional Reflectance Distribution Function |

APPENDIX D

SYMBOLS

- A** Averaging kernel matrix
- B^j** Greek matrix, or the coefficients of phase matrix expansion

APPENDIX E

LIST OF PUBLICATIONS GENERATED DURING PHD STUDY

REFERENCES

- Benedetti, A., et al. (2009), Aerosol analysis and forecast in the european centre for medium-range weather forecasts integrated forecast system: 2. data assimilation, *J. Geophys. Res.*, 114(D13), D13,205. [B.1](#)
- Bey, I., et al. (2001), Global modeling of tropospheric chemistry with assimilated meteorology: Model description and evaluation, *J. Geophys. Res.*, 106(D19), 23,073–23,095. [B.2.1](#)
- Bodhaine, B. A., N. B. Wood, E. G. Dutton, and J. R. Slusser (1999), On rayleigh optical depth calculations, *Journal of Atmospheric and Oceanic Technology*, 16(11), 1854–1861. [2.2.1](#)
- Boersma, K. F., D. J. Jacob, H. J. Eskes, R. W. Pinder, J. Wang, and R. J. van der A (2008), Intercomparison of sciamachy and omi tropospheric no₂ columns: Observing the diurnal evolution of chemistry and emissions from space, *Journal of Geophysical Research: Atmospheres*, 113(D16), D16S26. [B.4.3](#)
- Boesche, E., P. Stammes, T. Ruhtz, R. Preusker, and J. Fischer (2006), Effect of aerosol microphysical properties on polarization of skylight: sensitivity study and measurements, *Appl. Opt.*, 45(34), 8790–8805. [4.1](#)
- Bond, T. C., E. Bhardwaj, R. Dong, R. Jogani, S. Jung, C. Roden, D. G. Streets, and N. M. Trautmann (2007), Historical emissions of black and organic carbon aerosol from energy-related combustion, 1850-2000, *Global Biogeochem. Cycles*, 21(2), GB2018. [B.2.1](#), [B.2.4](#)
- Borrego, C., et al. (2008), *Development of Fire Emissions Inventory Using Satellite Data*, pp. 217–225, NATO Science for Peace and Security Series C: Environmental Security, Springer Netherlands, Dordrecht. [B.1](#)

- Boucher, O., et al. (2013), *Clouds and Aerosols. In Climate Change 2013: The Physical Science Basis. Contribution of Working Group I to the Fifth Assessment Report of the Intergovernmental Panel on Climate Change [Stocker T.F., et al. (eds.)]*, p. 571–658, Cambridge University Press, Cambridge, United Kingdom and New York, NY, USA. [1.1](#)
- Bucsela, E. J., E. A. Celarier, M. O. Wenig, J. F. Gleason, J. P. Veefkind, K. F. Boersma, and E. J. Brinksma (2006), Algorithm for no₂ vertical column retrieval from the ozone monitoring instrument, *Geoscience and Remote Sensing, IEEE Transactions on*, 44(5), 1245–1258. [B.4](#)
- Byrd, R. H., P. Lu, J. Nocedal, and C. Zhu (1995), A limited memory algorithm for bound constrained optimization, *SIAM Journal on Scientific Computing*, 16, 1190–1208. [3.3.3](#), [B.2.2](#)
- Cairns, B., B. E. Carlson, A. A. Lacis, and E. E. Russell (1997), An analysis of ground-based polarimetric sky radiance measurements, p. 383–393, Proc. SPIE. [4.1](#)
- Celarier, E. A., et al. (2008), Validation of ozone monitoring instrument nitrogen dioxide columns, *J. Geophys. Res.*, 113(D15), D15S15. [B.4.3](#)
- Chin, M., et al. (2002), Tropospheric aerosol optical thickness from the gocart model and comparisons with satellite and sun photometer measurements, *Journal of the Atmospheric Sciences*, 59(3), 461–483. [1.1.3](#)
- Chowdhary, J., B. Cairns, M. Mishchenko, and L. Travis (2001), Retrieval of aerosol properties over the ocean using multispectral and multiangle photopolarimetric measurements from the research scanning polarimeter, *Geophysical Research Letters*, 28(2), 243–246. [1.1.3](#)
- Chowdhary, J., B. Cairns, and L. D. Travis (2002), Case studies of aerosol retrievals over the ocean from multiangle, multispectral photopolarimetric remote sensing data, *Journal of the Atmospheric Sciences*, 59(3), 383–397. [1.1.3](#)
- Chowdhary, J., B. Cairns, M. I. Mishchenko, P. V. Hobbs, G. F. Cota, J. Redemann, K. Rutledge, B. N. Holben, and E. Russell (2005), Retrieval of aerosol scattering and absorption properties from photopolarimetric observations over the ocean during the clams experiment, *Journal of the Atmospheric Sciences*, 62(4), 1093–1117. [1.1.3](#)

- Coulson, A. (1988), *Polarization and intensity of light in the atmosphere*, VA A Deepak Pub, Hampton. [2.3](#), [2.3](#)
- Coulson, K., J. Dave, and Z. Sekera (1960), *Tables related to radiation emerging from a planetary atmosphere With Rayleigh scattering*, Univ California Press, Berkeley, CA. [2.3](#), [2.3](#)
- Cox, C., and W. Munk (1954), Measurement of the roughness of the sea surface from photographs of the sun's glitter, *Journal of the Optical Society of America*, 44(11), 838–850. [2.2.3](#)
- Curcio, J. (1961), Evaluation of atmospheric aerosol particle size distribution from scattering measurements in the visible and infrared, *Journal of the Optical Society of America*, 51(5), 548–551. [1.1.1](#)
- Dave, J. V. (1971), Determination of size distribution of spherical polydispersions using scattered radiation data, *Applied Optics*, 10(9), 2035–2044. [1.1.1](#)
- de Rooij, W. A., and C. C. A. H. v. d. Stap (1984), Expansion of mie scattering matrices in generalized spherical functions, *Astronomy and Astrophysics*, 131(2), 237–248. [2.2.2](#)
- Deuzé, J. L., F. M. Bréon, P. Y. Deschamps, C. Devaux, M. Herman, A. Podaire, and J. L. Roujean (1993), Analysis of the polder (polarization and directionality of earth's reflectances) airborne instrument observations over land surfaces, *Remote Sensing of Environment*, 45(2), 137–154. [1.1.3](#), [1](#)
- Deuzé, J. L., et al. (2001), Remote sensing of aerosols over land surfaces from polder-adeos-1 polarized measurements, *Journal of Geophysical Research: Atmospheres*, 106(D5), 4913–4926. [1.1.3](#), [1](#)
- Diner, D. J., et al. (1998), Multi-angle imaging spectroradiometer (misr) instrument description and experiment overview, *Geoscience and Remote Sensing, IEEE Transactions on*, 36(4), 1072–1087. [1.1.3](#)
- Ding, S., J. Wang, X. Xu, and R. Spurr (2014), Retrieval of optical depth and vertical distribution of atmospheric aerosols from light intensity and polarization in o2a and o2b bands, in *2014 AGU Fall Meeting*. [2.2](#)

- Drury, E., D. J. Jacob, J. Wang, R. J. D. Spurr, and K. Chance (2008), Improved algorithm for modis satellite retrievals of aerosol optical depths over western north america, *J. Geophys. Res.*, 113(D16), D16,204. [B.1](#)
- Drury, E., et al. (2010), Synthesis of satellite (modis), aircraft (icartt), and surface (improve, epa-aqs, aeronet) aerosol observations over eastern north america to improve modis aerosol retrievals and constrain surface aerosol concentrations and sources, *J. Geophys. Res.*, 115(D14), D14,204. [1.1.3](#), [4.2.1](#), [B.2.1](#)
- Dubovik, O. (2004), *Optimization of Numerical Inversion in Photopolarimetric Remote Sensing, NATO Science Series II: Mathematics, Physics and Chemistry*, vol. 161, book section 3, pp. 65–106, Springer Netherlands. [3.3.3](#), [4.3.1](#)
- Dubovik, O., and M. D. King (2000), A flexible inversion algorithm for retrieval of aerosol optical properties from sun and sky radiance measurements, *J. Geophys. Res.*, 105(D16), 20,673–20,696. [1.1.1](#), [1.1.2](#), [3.3.2](#), [3.3.2](#), [3.3.2](#), [3.3.3](#)
- Dubovik, O., A. Smirnov, B. N. Holben, M. D. King, Y. J. Kaufman, T. F. Eck, and I. Slutsker (2000), Accuracy assessments of aerosol optical properties retrieved from aerosol robotic network (aeronet) sun and sky radiance measurements, *Journal of Geophysical Research*, 105(D8), 9791–9806. [1.1.2](#), [1.1.3](#), [4.4](#), [4.4](#)
- Dubovik, O., B. N. Holben, T. Lapyonok, A. Sinyuk, M. I. Mishchenko, P. Yang, and I. Slutsker (2002a), Non-spherical aerosol retrieval method employing light scattering by spheroids, *Geophysical Research Letters*, 29(10). [1.1.1](#)
- Dubovik, O., B. Holben, T. F. Eck, A. Smirnov, Y. J. Kaufman, M. D. King, D. Tanre, and I. Slutsker (2002b), Variability of absorption and optical properties of key aerosol types observed in worldwide locations, *Journal of the Atmospheric Sciences*, 59(3), 590–608. [1.1.3](#)
- Dubovik, O., et al. (2006), Application of spheroid models to account for aerosol particle nonsphericity in remote sensing of desert dust, *Journal of Geophysical Research: Atmospheres*, 111, D11,208. [1.1.1](#), [1.1.2](#), [1.1.3](#), [4.1](#), [1](#)
- Dubovik, O., T. Lapyonok, Y. J. Kaufman, M. Chin, P. Ginoux, R. A. Kahn, and A. Sinyuk (2008), Retrieving global aerosol sources from satellites using inverse modeling, *Atmos. Chem. Phys.*, 8(2), 209–250. [B.1](#)

- Dubovik, O., M. Herman, A. Holdak, T. Lapyonok, D. Tanre, J. L. Deuze, F. Ducos, A. Sinyuk, and A. Lopatin (2011), Statistically optimized inversion algorithm for enhanced retrieval of aerosol properties from spectral multi-angle polarimetric satellite observations, *Atmos. Meas. Tech.*, 4(5), 975–1018. [2.2.3](#)
- Eck, T. F., et al. (2010), Climatological aspects of the optical properties of fine/coarse mode aerosol mixtures, *Journal of Geophysical Research: Atmospheres*, 115(D19), D19,205. [5.6, 2](#)
- Eck, T. F., et al. (2012), Fog- and cloud-induced aerosol modification observed by the aerosol robotic network (aeronet), *Journal of Geophysical Research: Atmospheres*, 117(D7), D07,206. [5.6, 2](#)
- Emde, C., R. Buras, B. Mayer, and M. Blumthaler (2010), The impact of aerosols on polarized sky radiance: model development, validation, and applications, *Atmos. Chem. Phys.*, 10(2), 383–396. [4.1](#)
- Evans, K. F., and G. L. Stephens (1991), A new polarized atmospheric radiative transfer model, *Journal of Quantitative Spectroscopy and Radiative Transfer*, 46(5), 413–423. [2.3](#)
- Fairlie, D. T., D. J. Jacob, and R. J. Park (2007), The impact of transpacific transport of mineral dust in the united states, *Atmospheric Environment*, 41(6), 1251–1266. [B.2.1, B.3, B.5.5, B.6](#)
- Frankenberg, C., O. Hasekamp, C. O'Dell, S. Sanghavi, A. Butz, and J. Worden (2012), Aerosol information content analysis of multi-angle high spectral resolution measurements and its benefit for high accuracy greenhouse gas retrievals, *Atmos. Meas. Tech.*, 5(7), 1809–1821. [3.2.2](#)
- Fu, T. M., et al. (2012), Carbonaceous aerosols in china: top-down constraints on primary sources and estimation of secondary contribution, *Atmos. Chem. Phys.*, 12(5), 2725–2746. [B.2.3](#)
- Garcia, R. D. M., and C. E. Siewert (1989), The fn method for radiative transfer models that include polarization effects, *Journal of Quantitative Spectroscopy and Radiative Transfer*, 41(2), 117–145. [2.4, 2.3](#)

- Ge, J. M., J. Su, T. P. Ackerman, Q. Fu, J. P. Huang, and J. S. Shi (2010), Dust aerosol optical properties retrieval and radiative forcing over northwestern china during the 2008 china-u.s. joint field experiment, *J. Geophys. Res.*, 115, D00K12. [B.4](#), [B.4.1](#), [B.4.4](#)
- Ginoux, P., M. Chin, I. Tegen, J. M. Prospero, B. Holben, O. Dubovik, and S.-J. Lin (2001), Sources and distributions of dust aerosols simulated with the gocart model, *J. Geophys. Res.*, 106(D17), 20,255–20,273. [B.2.1](#)
- Grassl, H. (1971), Determination of aerosol size distributions from spectral attenuation measurements, *Applied Optics*, 10(11), 2534–2538. [1.1.1](#)
- Halthore, R. N., T. F. Eck, B. N. Holben, and B. L. Markham (1997), Sun photometric measurements of atmospheric water vapor column abundance in the 940-nm band, *Journal of Geophysical Research: Atmospheres*, 102(D4), 4343–4352. [2.2.1](#)
- Han, D., J. Wang, X. Xu, W. Hou, and L. Chen (2014), Application of gosat tanso-cai observations for aerosol optical depth retrieval and surface pm2.5 air quality monitoring, in *2014 AGU Fall Meeting*. [2.2](#)
- Hansen, J. E., and L. D. Travis (1974), Light scattering in planetary atmospheres, *Space Sci. Rev.*, 16, 572–610. [1.1.1](#), [1.1.3](#), [2.1](#), [2.2.1](#), [3.3.1](#), [4.1](#), [4.3.1](#), [4.3.2.3](#)
- Hansen, P. C. (1998), *Rank-Deficient and Discrete Ill-Posed Problems: Numerical Aspects of Linear Inversion*, Soc. for Ind. and Appl. Math., Philadelphia, Pa. [3.3.3](#), [B.2.4](#)
- Hasekamp, O. P., and J. Landgraf (2005a), Retrieval of aerosol properties over the ocean from multispectral single-viewing-angle measurements of intensity and polarization: Retrieval approach, information content, and sensitivity study, *J. Geophys. Res.*, 110(D20), D20,207. [3.2.2](#), [3.3.1](#)
- Hasekamp, O. P., and J. Landgraf (2007), Retrieval of aerosol properties over land surfaces: capabilities of multiple-viewing-angle intensity and polarization measurements, *Applied Optics*, 46(16), 3332–3344. [3.3.1](#)
- Hasekamp, O. P., P. Litvinov, and A. Butz (2011), Aerosol properties over the ocean from parasol multiangle photopolarimetric measurements, *Journal of Geophysical Research: Atmospheres*, 116(D14), D14,204. [1.1.3](#)
- Haywood, J., and O. Boucher (2000), Estimates of the direct and indirect radiative forcing due to tropospheric aerosols: A review, *Rev. Geophys.*, 38(4), 513–543. [1.1](#), [B.1](#)

- Heald, C. L., et al. (2004), Comparative inverse analysis of satellite (mopitt) and aircraft (trace-p) observations to estimate asian sources of carbon monoxide, *J. Geophys. Res.*, 109(D23), D23,306. [B.1](#)
- Heald, C. L., D. J. Jacob, R. J. Park, L. M. Russell, B. J. Huebert, J. H. Seinfeld, H. Liao, and R. J. Weber (2005), A large organic aerosol source in the free troposphere missing from current models, *Geophysical Research Letters*, 32(18), L18,809. [B.2.3](#)
- Henze, D. K., A. Hakami, and J. H. Seinfeld (2007), Development of the adjoint of geos-chem, *Atmos. Chem. Phys.*, 7(9), 2413–2433. [3.1](#), [3.3](#), [B.1](#), [B.2.2](#)
- Henze, D. K., J. H. Seinfeld, and D. T. Shindell (2009), Inverse modeling and mapping us air quality influences of inorganic pm2.5 precursor emissions using the adjoint of geos-chem, *Atmos. Chem. Phys.*, 9(16), 5877–5903. [B.1](#), [B.2.2](#)
- Herman, B. M., S. R. Browning, and J. A. Reagan (1971), Determination of aerosol size distributions from lidar measurements, *Journal of the Atmospheric Sciences*, 28(5), 763–771. [1.1.1](#)
- Hess, M., P. Koepke, and I. Schult (1998), Optical properties of aerosols and clouds: The software package opac, *Bulletin of the American Meteorological Society*, 79(5), 831–844. [2.5](#), [4.2.1](#)
- Holben, B. N., et al. (1998), Aeronet - a federated instrument network and data archive for aerosol characterization, *Remote Sensing of Environment*, 66(1), 1–16. [1.1](#), [1.1.1](#), [1.1.2](#), [4.2.2](#), [B.4](#)
- Holben, B. N., T. F. Eck, I. Slutsker, A. Smirnov, A. Sinyuk, J. Schafer, D. Giles, and O. Dubovik (2006), Aeronet's version 2.0 quality assurance criteria, *Proc. SPIE 6408, Remote Sensing of the Atmosphere and Clouds*, 64080Q. [1.1.3](#), [3.3.5](#), [4.4](#)
- Hou, W., J. Wang, X. Xu, S. Ding, D. Han, J. Leitch, T. Delker, and G. Chen (2014), An algorithm for simultaneous inversion of aerosol properties and surface reflectance from airborne geotaso hyperspectral data, in *2014 AGU Fall Meeting*. [2.2](#)
- Hovenier, J., C. v. d. Mee, and H. Domke (2004), *Transfer Of Polarized Light In Planetary Atmospheres*, 258 pp., Kluwer Academic Publishers, Dordrecht, The Netherlands. [2.1](#)

- Huang, X., Y. Song, M. Li, J. Li, Q. Huo, X. Cai, T. Zhu, M. Hu, and H. Zhang (2012), A high-resolution ammonia emission inventory in china, *Global Biogeochem. Cycles*, 26(1), GB1030. [B.5.2](#), [B.4](#)
- Huang, Z., J. Huang, J. Bi, G. Wang, W. Wang, Q. Fu, Z. Li, S.-C. Tsay, and J. Shi (2010), Dust aerosol vertical structure measurements using three mpl lidars during 2008 china-u.s. joint dust field experiment, *J. Geophys. Res.*, 115, D00K15. [B.1](#), [B.4.4](#)
- IPCC (2007), *Climate Change 2007: The Physical Sciences Basis. Contribution of Working Group I to the Fourth Assessment Report of the Intergovernmental Panel on Climate Change* [Solomon, S., D. Qin, M. Manning, Z. Chen, M. Marquis, K.B. Averyt, M. Tignor and H.L. Miller (eds.)], 996 pp., Cambridge University Press, Cambridge, United Kingdom and New York, NY, USA. [B.1](#)
- Jiang, Z., D. B. A. Jones, M. Kopacz, J. Liu, D. K. Henze, and C. Heald (2011), Quantifying the impact of model errors on top-down estimates of carbon monoxide emissions using satellite observations, *Journal of Geophysical Research: Atmospheres*, 116(D15), D15,306. [B.2.2](#)
- Kahn, R. A., B. J. Gaitley, J. V. Martonchik, D. J. Diner, K. A. Crean, and B. Holben (2005), Multiangle imaging spectroradiometer (misr) global aerosol optical depth validation based on 2 years of coincident aerosol robotic network (aeronet) observations, *J. Geophys. Res.*, 110(D10), D10S04. [B.4](#), [B.4.2](#)
- Kahn, R. A., B. J. Gaitley, M. J. Garay, D. J. Diner, T. F. Eck, A. Smirnov, and B. N. Holben (2010), Multiangle imaging spectroradiometer global aerosol product assessment by comparison with the aerosol robotic network, *J. Geophys. Res.*, 115(D23), D23,209. [1.1.3](#), [B.4.2](#)
- Kaufman, Y. J., A. Gitelson, A. Karnieli, E. Ganor, R. S. Fraser, T. Nakajima, S. Mattoo, and B. N. Holben (1994), Size distribution and scattering phase function of aerosol particles retrieved from sky brightness measurements, *Journal of Geophysical Research: Atmospheres*, 99(D5), 10,341–10,356. [1.1.1](#)
- Kaufman, Y. J., D. Tanré, L. A. Remer, E. F. Vermote, A. Chu, and B. N. Holben (1997), Operational remote sensing of tropospheric aerosol over land from eos moderate resolution imaging spectroradiometer, *Journal of Geophysical Research: Atmospheres*, 102(D14), 17,051–17,067. [1.1.3](#)

Kaufman, Y. J., D. Tanre, and O. Boucher (2002), A satellite view of aerosols in the climate system, *Nature*, 419, 215 – 223. [1.1](#), [B.6](#)

King, M. D., D. M. Byrne, B. M. Herman, and J. A. Reagan (1978), Aerosol size distributions obtained by inversions of spectral optical depth measurements, *Journal of the Atmospheric Sciences*, 35(11), 2153–2167. [1.1.1](#)

King, M. D., Y. J. Kaufman, D. Tanre, and T. Nakajima (1999), Remote sensing of tropospheric aerosols from space: Past, present, and future, *Bulletin of the American Meteorological Society*, 80(11), 2229–2259. [B.6](#)

Knobelispiesse, K., B. Cairns, M. Mishchenko, J. Chowdhary, K. Tsigaridis, B. van Diedenhoven, W. Martin, M. Ottaviani, and M. Alexandrov (2012), Analysis of fine-mode aerosol retrieval capabilities by different passive remote sensing instrument designs, *Optics Express*, 20(19), 21,457–21,484. [3.2.2](#), [4.4](#)

Kopacz, M., D. J. Jacob, D. K. Henze, C. L. Heald, D. G. Streets, and Q. Zhang (2009), Comparison of adjoint and analytical bayesian inversion methods for constraining asian sources of carbon monoxide using satellite (mopitt) measurements of co columns, *J. Geophys. Res.*, 114(D4), D04,305. [B.1](#), [B.2.2](#)

Kopacz, M., et al. (2010), Global estimates of co sources with high resolution by adjoint inversion of multiple satellite datasets (mopitt, airs, sciamachy, tes), *Atmos. Chem. Phys.*, 10(3), 855–876. [B.1](#), [B.2.2](#)

Kopacz, M., D. L. Mauzerall, J. Wang, E. M. Leibensperger, D. K. Henze, and K. Singh (2011), Origin and radiative forcing of black carbon transported to the himalayas and tibetan plateau, *Atmos. Chem. Phys.*, 11(6), 2837–2852. [B.2.2](#)

Krotkov, N. A., S. A. Carn, A. J. Krueger, P. K. Bhartia, and Y. Kai (2006), Band residual difference algorithm for retrieval of so₂ from the aura ozone monitoring instrument (omi), *Geoscience and Remote Sensing, IEEE Transactions on*, 44(5), 1259–1266. [B.4](#)

Ku, B., and R. J. Park (2011), Inverse modeling analysis of soil dust sources over east asia, *Atmospheric Environment*, 45(32), 5903–5912. [B.5.5](#)

Lamsal, L., R. Martin, A. Padmanabhan, A. v. Donkelaar, Q. Zhang, C. Sioris, K. Chance, T. Kurosu, and M. Newchurch (2011), Application of satellite observations for timely

updates to global anthropogenic nox emission inventories, *Geophys. Res. Lett.*, 38(5), L05,810. [B.1](#)

Lee, C., R. V. Martin, A. van Donkelaar, G. O’Byrne, N. Krotkov, A. Richter, L. G. Huey, and J. S. Holloway (2009), Retrieval of vertical columns of sulfur dioxide from sciamachy and omi: Air mass factor algorithm development, validation, and error analysis, *J. Geophys. Res.*, 114(D22), D22,303. [B.4](#)

Lee, C., et al. (2011), So2 emissions and lifetimes: Estimates from inverse modeling using in situ and global, space-based (sciamachy and omi) observations, *J. Geophys. Res.*, 116, D06,304. [B.1](#), [B.5.1](#)

Levelt, P. F., E. Hilsenrath, G. W. Leppelmeier, G. H. J. van den Oord, P. K. Bhartia, J. Tamminen, J. F. de Haan, and J. P. Veefkind (2006), Science objectives of the ozone monitoring instrument, *Geoscience and Remote Sensing, IEEE Transactions on*, 44(5), 1199–1208. [2.2.1](#)

Levy, R. C., L. A. Remer, and O. Dubovik (2007a), Global aerosol optical properties and application to moderate resolution imaging spectroradiometer aerosol retrieval over land, *Journal of Geophysical Research: Atmospheres*, 112(D13), D13,210. [1.1.3](#)

Levy, R. C., L. A. Remer, S. Mattoo, E. F. Vermote, and Y. J. Kaufman (2007b), Second-generation operational algorithm: Retrieval of aerosol properties over land from inversion of moderate resolution imaging spectroradiometer spectral reflectance, *J. Geophys. Res.*, 112(D13), D13,211. [1.1.3](#)

Levy, R. C., L. A. Remer, R. G. Kleidman, S. Mattoo, C. Ichoku, R. Kahn, and T. F. Eck (2010), Global evaluation of the collection 5 modis dark-target aerosol products over land, *Atmos. Chem. Phys.*, 10(21), 10,399–10,420. [1.1.3](#), [B.1](#)

Li, Z., L. Blarel, T. Podvin, P. Goloub, J.-P. Buis, and J.-P. Morel (2008), Transferring the calibration of direct solar irradiance to diffuse-sky radiance measurements for cimel sun-sky radiometers, *Appl. Opt.*, 47(10), 1368–1377. [5.2](#)

Li, Z., et al. (2009), Improvements for ground-based remote sensing of atmospheric aerosol properties by additional polarimetric measurements, *Journal of Quantitative Spectroscopy and Radiative Transfer*, 110(17), 1954–1961. [1.1.2](#), [1.1.3](#), [4.1](#), [4.2.2](#), [5.4](#), [5.4](#)

- Li, Z., L. Blarel, T. Podvin, P. Goloub, and L. Chen (2010), Calibration of the degree of linear polarization measurement of polarized radiometer using solar light, *Appl. Opt.*, 49(8), 1249–1256. [5.2](#)
- Lin, J. T., M. B. McElroy, and K. F. Boersma (2010), Constraint of anthropogenic nox emissions in china from different sectors: a new methodology using multiple satellite retrievals, *Atmos. Chem. Phys.*, 10(1), 63–78. [B.1](#), [B.4.3](#), [B.5.3](#), [B.4](#)
- Liou, K. N. (2002), *An Introduction to Atmospheric Radiation*, 583 pp., Academic Press, San Diego, CA, USA. [2.2.1](#)
- Litvinov, P., O. Hasekamp, and B. Cairns (2011), Models for surface reflection of radiance and polarized radiance: Comparison with airborne multi-angle photopolarimetric measurements and implications for modeling top-of-atmosphere measurements, *Remote Sensing of Environment*, 115(2), 781–792. [2.2.3](#)
- Liu, Y., J. A. Sarnat, V. Kilaru, D. J. Jacob, and P. Koutrakis (2005), Estimating ground-level pm2.5 in the eastern united states using satellite remote sensing, *Environmental Science and Technology*, 39(9), 3269–3278. [B.1](#)
- Lu, Z., et al. (2010), Sulfur dioxide emissions in china and sulfur trends in east asia since 2000, *Atmos. Chem. Phys.*, 10(13), 6311–6331. [B.5.1](#), [B.4](#)
- Lu, Z., Q. Zhang, and D. G. Streets (2011), Sulfur dioxide and primary carbonaceous aerosol emissions in china and india, 1996-2010, *Atmos. Chem. Phys.*, 11(18), 9839–9864. [B.5.1](#), [B.4](#), [B.5.4](#)
- Lucht, W., C. B. Schaaf, and A. H. Strahler (2000), An algorithm for the retrieval of albedo from space using semiempirical brdf models, *Geoscience and Remote Sensing, IEEE Transactions on*, 38(2), 977–998. [2.2.3](#), [2.2.3](#), [4.2.2](#)
- Maignan, F., F. M. Bréon, and R. Lacaze (2004), Bidirectional reflectance of earth targets: evaluation of analytical models using a large set of spaceborne measurements with emphasis on the hot spot, *Remote Sensing of Environment*, 90(2), 210–220. [2.2.3](#)
- Maignan, F., F.-M. Bréon, E. Fédèle, and M. Bouvier (2009), Polarized reflectances of natural surfaces: Spaceborne measurements and analytical modeling, *Remote Sensing of Environment*, 113(12), 2642–2650. [2.2.3](#), [2.2.3](#), [2.2.3](#), [4.2.2](#)

- Martin, R. V., D. J. Jacob, K. Chance, T. P. Kurosu, P. I. Palmer, and M. J. Evans (2003a), Global inventory of nitrogen oxide emissions constrained by space-based observations of no₂ columns, *J. Geophys. Res.*, 108(D17), 4537. [B.1](#)
- Martonchik, J. V., R. A. Kahn, and D. J. Diner (2009), *Retrieval of aerosol properties over land using MISR observations*, Springer, Berlin. [1.1.3](#), [B.4](#), [B.6](#)
- Ministry of Environmental Protection (2009), Report on the state of the environment in china 2008, beijing, china. [B.5.1](#), [B.5.4](#)
- McClatchey, R. A., R. W. Fenn, J. E. A. Selby, F. E. Volz, and J. S. Garing (1972), Optical properties of the atmosphere (third edition), *Report*, Air Force Cambridge Research Labs Hanscom AFB MA. [2.2](#), [2.2](#)
- Mijling, B., R. J. van der A, K. F. Boersma, M. Van Roozendael, I. De Smedt, and H. M. Kelder (2009), Reductions of no₂ detected from space during the 2008 beijing olympic games, *Geophysical Research Letters*, 36(13), L13,801. [B.5.3](#)
- Mishchenko, M. I., and L. D. Travis (1997), Satellite retrieval of aerosol properties over the ocean using polarization as well as intensity of reflected sunlight, *J. Geophys. Res.*, 102(D14), 16,989–17,013. [1.1.3](#), [4.1](#)
- Mishchenko, M. I., and L. D. Travis (1998), Capabilities and limitations of a current fortran implementation of the t-matrix method for randomly oriented, rotationally symmetric scatterers, *Journal of Quantitative Spectroscopy and Radiative Transfer*, 60(3), 309–324. [2.2.2](#)
- Mishchenko, M. I., L. D. Travis, and D. W. Mackowski (1996), T-matrix computations of light scattering by nonspherical particles: A review, *Journal of Quantitative Spectroscopy and Radiative Transfer*, 55(5), 535–575. [2.2.2](#)
- Mishchenko, M. I., L. D. Travis, and A. A. Lacis (2002), *Scattering, Absorption, and Emission of Light by Small Particles*, Cambridge University Press, Cambridge, UK. [1.1.3](#), [2.1](#)
- Mishchenko, M. I., B. Cairns, J. E. Hansen, L. D. Travis, R. Burg, Y. J. Kaufman, J. Vanderlei Martins, and E. P. Shettle (2004), Monitoring of aerosol forcing of climate from space: analysis of measurement requirements, *Journal of Quantitative Spectroscopy and Radiative Transfer*, 88(1-3), 149–161. [1.1](#), [1.1.3](#), [4.3.2.1](#), [4.4](#), [4.3.2.3](#)

- Mishchenko, M. I., et al. (2007), Accurate monitoring of terrestrial aerosols and total solar irradiance: Introducing the glory mission, *Bulletin of the American Meteorological Society*, 88(5), 677–691. [1.1.3](#), [3.3.1](#)
- Muller, J. F., and T. Stavrakou (2005), Inversion of co and nox emissions using the adjoint of the images model, *Atmos. Chem. Phys.*, 5(5), 1157–1186. [B.1](#)
- Myhre, G., et al. (2013), *Anthropogenic and Natural Radiative Forcing*. In *Climate Change 2013: The Physical Science Basis. Contribution of Working Group I to the Fifth Assessment Report of the Intergovernmental Panel on Climate Change [Stocker T.F., et al. (eds.)]*, book section 8, p. 659–740, Cambridge University Press, Cambridge, United Kingdom and New York, NY, USA. [1.1](#)
- Nadal, F., and F. M. Breon (1999), Parameterization of surface polarized reflectance derived from polder spaceborne measurements, *Geoscience and Remote Sensing, IEEE Transactions on*, 37(3), 1709–1718. [2.2.3](#), [4.2.2](#)
- Nakajima, T., M. Tanaka, and T. Yamauchi (1983), Retrieval of the optical properties of aerosols from aureole and extinction data, *Applied Optics*, 22(19), 2951–2959. [1.1.1](#)
- Nakajima, T., G. Tonna, R. Rao, P. Boi, Y. Kaufman, and B. Holben (1996), Use of sky brightness measurements from ground for remote sensing of particulate polydispersions, *Applied Optics*, 35(15), 2672–2686. [1.1.1](#)
- Nassar, R., et al. (2011), Inverse modeling of co2 sources and sinks using satellite observations of co2 from tes and surface flask measurements, *Atmos. Chem. Phys.*, 11(2), 6029–6047. [B.1](#)
- Ohara, T., H. Akimoto, J. Kurokawa, N. Horii, K. Yamaji, X. Yan, and T. Hayasaka (2007), An asian emission inventory of anthropogenic emission sources for the period 1980–2020, *Atmos. Chem. Phys.*, 7(16), 4419–4444. [B.5.2](#)
- Orphal, J., and K. Chance (2003), Ultraviolet and visible absorption cross-sections for hitran, *Journal of Quantitative Spectroscopy and Radiative Transfer*, 82(1-4), 491–504. [2.2.1](#)
- Park, R. J., D. J. Jacob, B. D. Field, R. M. Yantosca, and M. Chin (2004), Natural and transboundary pollution influences on sulfate-nitrate-ammonium aerosols in the united states: Implications for policy, *J. Geophys. Res.*, 109(D15), D15,204. [B.2.1](#)

- Parrington, M., et al. (2012), The influence of boreal biomass burning emissions on the distribution of tropospheric ozone over north america and the north atlantic during 2010, *Atmospheric Chemistry and Physics*, 12(4), 2077–2098. [B.2.2](#)
- Patterson, E. M., D. A. Gillette, and B. H. Stockton (1977), Complex index of refraction between 300 and 700 nm for saharan aerosols, *Journal of Geophysical Research*, 82(21), 3153–3160. [4.2.1](#)
- Phillips, D. L. (1962), A technique for the numerical solution of certain integral equations of the first kind, *J. ACM*, 9(1), 84–97. [1.1.1](#), [3.3.2](#)
- Pope, C. A., M. Ezzati, and D. W. Dockery (2009), Fine-particulate air pollution and life expectancy in the united states, *New England Journal of Medicine*, 360(4), 376–386. [B.1](#)
- Qin, Y., and S. D. Xie (2012), Spatial and temporal variation of anthropogenic black carbon emissions in china for the period 1980–2009, *Atmos. Chem. Phys.*, 12(11), 4825–4841. [B.4](#), [B.5.4](#)
- Ramanathan, V., P. J. Crutzen, J. T. Kiehl, and D. Rosenfeld (2001), Aerosols, climate, and the hydrological cycle, *Science*, 294(5549), 2119–2124. [1.1](#)
- Reid, J. S., et al. (2008), An overview of uae2 flight operations: Observations of summertime atmospheric thermodynamic and aerosol profiles of the southern arabian gulf, *Journal of Geophysical Research: Atmospheres*, 113(D14), D14,213. [1.1.2](#), [4.1](#), [4.2.2](#)
- Reid, J. S., et al. (2009), Global monitoring and forecasting of biomass-burning smoke: Description of and lessons from the fire locating and modeling of burning emissions (flambe) program, *Selected Topics in Applied Earth Observations and Remote Sensing, IEEE Journal of*, 2(3), 144–162. [B.1](#)
- Remer, L. A., et al. (2005), The modis aerosol algorithm, products, and validation, *Journal of the Atmospheric Sciences*, 62(4), 947–973. [1.1.3](#), [B.1](#)
- Ricchiazzi, P., S. Yang, C. Gautier, and D. Sowle (1998), Sbdart: A research and teaching software tool for plane-parallel radiative transfer in the earth’s atmosphere, *Bulletin of the American Meteorological Society*, 79(10), 2101–2114. [2.2](#), [2.3](#)
- Rodgers, C. D. (1998), Information content and optimisation of high spectral resolution remote measurements, *Advances in Space Research*, 21(3), 361–367. [3.2.2](#), [3.2.2](#)

- Rodgers, C. D. (2000), *Inverse Methods for Atmospheric Sounding: Theory and Practice*, World Scientific, Singapore. [3.2.1](#), [3.2.1](#), [3.2.2](#), [3.3.3](#), [B.6](#)
- Rothman, L. S., et al. (2009), The hitran 2008 molecular spectroscopic database, *Journal of Quantitative Spectroscopy and Radiative Transfer*, *110*(9-10), 533–572. [2.2.1](#)
- Sanghavi, S., J. V. Martonchik, J. Landgraf, and U. Platt (2012), Retrieval of aerosol optical depth and vertical distribution using o2 a- and b-band sciamachy observations over kanpur: a case study, *Atmos. Meas. Tech.*, *5*(5), 1099–1119. [3.2.2](#)
- Schulz, M., et al. (2006), Radiative forcing by aerosols as derived from the aerocom present-day and pre-industrial simulations, *Atmos. Chem. Phys.*, *6*(12), 5225–5246. [B.1](#)
- Schuster, G. L., O. Dubovik, and B. N. Holben (2006), Angstrom exponent and bimodal aerosol size distributions, *J. Geophys. Res.*, *111*, D07,207. [2.2.2](#), [3.3.1](#), [4.4](#), [5.2](#)
- Seinfeld, J. H., and S. N. Pandis (2006), *Atmospheric Chemistry and Physics: From Air Pollution to Climate Change, 2nd Edition*, 1232 pp., John Wiley and Sons, Inc., Hoboken, New Jersey. [2.2.2](#), [B.2.1](#)
- Shannon, C. E. (1948), A mathematical theory of communication, *Bell System Technical Journal*, *27*(3), 379–423. [3.2.2](#)
- Shaw, G. E. (1979), Inversion of optical scattering and spectral extinction measurements to recover aerosol size spectra, *Applied Optics*, *18*(7), 988–993. [1.1.1](#)
- Sinyuk, A., et al. (2008), Multi-sensor aerosol retrievals using joint inversion of aeronet and satellite observations: concept and applications. [B.1](#)
- Smirnov, A., B. N. Holben, T. F. Eck, O. Dubovik, and I. Slutsker (2000), Cloud-screening and quality control algorithms for the aeronet database, *Remote Sensing of Environment*, *73*(3), 337–349. [1.1.2](#)
- Spurr, R. (2006), Vlidort: A linearized pseudo-spherical vector discrete ordinate radiative transfer code for forward model and retrieval studies in multilayer multiple scattering media, *Journal of Quantitative Spectroscopy and Radiative Transfer*, *102*, 316–342. [2.2.1](#), [2.2.4](#), [3.3](#), [B.2.3](#)

- Spurr, R., and M. Christi (2014), On the generation of atmospheric property jacobians from the (v)lidort linearized radiative transfer models, *Journal of Quantitative Spectroscopy and Radiative Transfer*, 142(0), 109–115. [A](#)
- Spurr, R., J. Wang, J. Zeng, and M. I. Mishchenko (2012), Linearized t-matrix and mie scattering computations, *Journal of Quantitative Spectroscopy and Radiative Transfer*, 113(6), 425–439. [2.2.2](#), [3.3](#)
- Spurr, R. J. D. (2004), A new approach to the retrieval of surface properties from earthshine measurements, *Journal of Quantitative Spectroscopy and Radiative Transfer*, 83(1), 15–46. [2.2.3](#), [3.3](#)
- Stavrakou, T., and J. F. M_{ller} (2006), Grid-based versus big region approach for inverting co emissions using measurement of pollution in the troposphere (mopitt) data, *J. Geophys. Res.*, 111(D15), D15,304. [B.1](#)
- Streets, D. G., et al. (2003), An inventory of gaseous and primary aerosol emissions in asia in the year 2000, *J. Geophys. Res.*, 108(D21), 8809. [B.1](#), [B.2.1](#), [B.5.2](#), [B.4](#)
- Streets, D. G., Q. Zhang, L. Wang, K. He, J. Hao, Y. Wu, Y. Tang, and G. R. Carmichael (2006), Revisiting china's co emissions after the transport and chemical evolution over the pacific (trace-p) mission: Synthesis of inventories, atmospheric modeling, and observations, *J. Geophys. Res.*, 111(D14), D14,306. [B.1](#)
- Tanaka, M., T. Nakajima, and T. Takamura (1982), Simultaneous determination of complex refractive index and size distribution of airborne and water-suspended particles from light scattering measurements, *Meteorological Society of Japan Journal*, 60, 1259–1272. [1.1.1](#)
- Tanaka, M., T. Takamura, and T. Nakajima (1983), Refractive index and size distribution of aerosols as estimated from light scattering measurements, *Journal of Climate and Applied Meteorology*, 22(7), 1253–1261. [1.1.1](#)
- Taylor, K. E. (2001), Summarizing multiple aspects of model performance in a single diagram, *J. Geophys. Res.*, 106(D7), 7183–7192. [B.4.5](#)
- Textor, C., et al. (2006), Analysis and quantification of the diversities of aerosol life cycles within aerocom, *Atmos. Chem. Phys.*, 6(7), 1777–1813. [B.1](#), [B.2.4](#)

- Twomey, S. (1963), On the numerical solution of fredholm integral equations of the first kind by the inversion of the linear system produced by quadrature, *J. ACM*, 10(1), 97–101. [1.1.1](#), [3.3.2](#)
- Twomey, S. (1977), *Introduction to the Mathematics of Inversion in Remote Sensing and Indirect Measurements*, 243 pp., Dover Publications, Inc., Mineola, NY, USA. [3.3.2](#)
- Twomey, S., and H. B. Howell (1967), Some aspects of the optical estimation of microstructure in fog and cloud, *Applied Optics*, 6(12), 2125–2131. [1.1.1](#)
- van de Hulst, H. C. (1981), *Light Scattering by Small Particles (Dover edition)*, Dover Publications, Mineola, New York. [4.3.1](#), [4.3.1](#)
- van der Werf, G. R., J. T. Randerson, L. Giglio, G. J. Collatz, P. S. Kasibhatla, and A. F. Arellano Jr (2006), Interannual variability in global biomass burning emissions from 1997 to 2004, *Atmos. Chem. Phys.*, 6(11), 3423–3441. [B.1](#)
- van der Werf, G. R., et al. (2010), Global fire emissions and the contribution of deforestation, savanna, forest, agricultural, and peat fires (1997–2009), *Atmos. Chem. Phys.*, 10(23), 11,707–11,735. [B.1](#), [B.2.1](#)
- van Donkelaar, A., et al. (2008), Analysis of aircraft and satellite measurements from the intercontinental chemical transport experiment (intex-b) to quantify long-range transport of east asian sulfur to canada, *Atmos. Chem. Phys.*, 8(11), 2999–3014. [B.1](#), [B.2.1](#)
- Vermeulen, A., C. Devaux, and M. Herman (2000), Retrieval of the scattering and microphysical properties of aerosols from ground-based optical measurements including polarization. i. method, *Appl. Opt.*, 39(33), 6207–6220. [4.1](#)
- Vijay, N., and J. W. Hovenier (2012), Polarized light reflected and transmitted by thick rayleigh scattering atmospheres, *The Astrophysical Journal*, 748(1), 28. [2.3](#)
- Wagner, R., T. Ajtai, K. Kandler, K. Lieke, C. Linke, T. Müller, M. Schnaiter, and M. Vragel (2012), Complex refractive indices of saharan dust samples at visible and near uv wavelengths: a laboratory study, *Atmospheric Chemistry and Physics*, 12(5), 2491–2512. [4.2.1](#)
- Walker, T. W., et al. (2010), Trans-pacific transport of reactive nitrogen and ozone to canada during spring, *Atmos. Chem. Phys.*, 10(17), 8353–8372. [B.1](#)

- Wang, J., and S. T. Martin (2007), Satellite characterization of urban aerosols: Importance of including hygroscopicity and mixing state in the retrieval algorithms, *Journal of Geophysical Research: Atmospheres*, 112(D17), D17,203. [5.4](#)
- Wang, J., X. Xia, P. Wang, and S. A. Christopher (2004), Diurnal variability of dust aerosol optical thickness and angstrom exponent over dust source regions in china, *Geophys. Res. Lett.*, 31(8), L08,107. [B.1](#)
- Wang, J., S. A. Christopher, U. S. Nair, J. S. Reid, E. M. Prins, J. Szykman, and J. L. Hand (2006), Mesoscale modeling of central american smoke transport to the united states: 1. "top-down" assessment of emission strength and diurnal variation impacts, *J. Geophys. Res.*, 111(D5), D05S17. [B.1](#)
- Wang, J., X. Xu, R. Spurr, Y. Wang, and E. Drury (2010), Improved algorithm for modis satellite retrievals of aerosol optical thickness over land in dusty atmosphere: Implications for air quality monitoring in china, *Remote Sensing of Environment*, 114(11), 2575–2583. [1.1.3](#), [3.3.2](#), [B.1](#), [B.2](#), [B.2.1](#), [B.2.3](#), [B.2](#), [B.6](#)
- Wang, J., X. Xu, D. K. Henze, J. Zeng, Q. Ji, S.-C. Tsay, and J. Huang (2012), Top-down estimate of dust emissions through integration of modis and misr aerosol retrievals with the geos-chem adjoint model, *Geophys. Res. Lett.*, 39(8), L08,802. [3.1](#), [3.3](#), [B.1](#), [B.2.4](#), [B.3](#), [B.5.5](#)
- Wang, J., X. Xu, S. Ding, J. Zeng, R. Spurr, X. Liu, K. Chance, and M. Mishchenko (2014), A numerical testbed for remote sensing of aerosols, and its demonstration for evaluating retrieval synergy from a geostationary satellite constellation of geo-cape and goes-r, *Journal of Quantitative Spectroscopy and Radiative Transfer*, 146(0), 510–528. [1](#), [2.2](#), [2.2](#), [2.3](#), [2.4](#), [2.4](#), [2.5](#), [2.6](#)
- Wanner, W., X. Li, and A. H. Strahler (1995), On the derivation of kernels for kernel-driven models of bidirectional reflectance, *Journal of Geophysical Research: Atmospheres*, 100(D10), 21,077–21,089. [2.2.3](#), [2.2.3](#), [4.2.2](#)
- Waquet, F., P. Goloub, J. L. Deuzé, J. F. Léon, F. Auriol, C. Verwaerde, J. Y. Balois, and P. François (2007), Aerosol retrieval over land using a multiband polarimeter and comparison with path radiance method, *Journal of Geophysical Research*, 112(D11). [2.2.3](#)

- Waquet, F., B. Cairns, K. Knobelospiesse, J. Chowdhary, L. D. Travis, B. Schmid, and M. I. Mishchenko (2009), Polarimetric remote sensing of aerosols over land, *J. Geophys. Res.*, 114(D1), D01,206. [1.1.3](#), [2.2.2](#), [3.3.1](#)
- Weaver, C., et al. (2007), Direct insertion of modis radiances in a global aerosol transport model, *Journal of the Atmospheric Sciences*, 64(3), 808–827. [B.1](#)
- Wecht, K. J., D. J. Jacob, S. C. Wofsy, E. A. Kort, J. R. Worden, S. S. Kulawik, D. K. Henze, M. Kopacz, and V. H. Payne (2012), Validation of tes methane with hippo aircraft observations: implications for inverse modeling of methane sources, *Atmospheric Chemistry and Physics*, 12(4), 1823–1832. [B.2.2](#)
- Wendisch, M., and W. Von Hoyningen-Huene (1994), Possibility of refractive index determination of atmospheric aerosol particles by ground-based solar extinction and scattering measurements, *Atmospheric Environment*, 28(5), 785–792. [1.1.1](#)
- Wesely, M. (1989), Parameterization of surface resistances to gaseous dry deposition in regional-scale numerical models, *Atmospheric Environment*, 23(6), 1293–1304. [B.2.1](#)
- Xu, X., and J. Wang (2015), Retrieval of aerosol microphysical properties from aeronet photo-polarimetric measurements: 1. information content analysis, *Submitted to J. Geophys. Res.* [3.4](#), [4.6](#)
- Xu, X., J. Wang, D. K. Henze, W. Qu, and M. Kopacz (2013), Constraints on aerosol sources using geos-chem adjoint and modis radiances, and evaluation with multisensor (omi, misr) data, *Journal of Geophysical Research: Atmospheres*, 118(12), 6396–6413. [3.1](#), [3.3](#), [B.1](#), [B.3](#), [B.4](#), [B.5](#), [B.6](#), [B.8](#), [B.14](#), [B.7](#)
- Xu, X., et al. (2015), Retrieval of aerosol microphysical properties from aeronet photo-polarimetric measurements. 2: A new research algorithm and case demonstration, *Submitted to J. Geophys. Res.* [3.4](#), [5.7](#)
- Yamamoto, G., and M. Tanaka (1969), Determination of aerosol size distribution from spectral attenuation measurements, *Applied Optics*, 8(2), 447–453. [1.1.1](#)
- Yamasoe, M. A., Y. J. Kaufman, O. Dubovik, L. A. Remer, B. N. Holben, and P. Artaxo (1998), Retrieval of the real part of the refractive index of smoke particles from sun/sky measurements during scar-b, *Journal of Geophysical Research: Atmospheres*, 103(D24), 31,893–31,902. [1.1.1](#)

Yang, Z., J. Wang, C. Ichoku, E. Hyer, and J. Zeng (2013), Mesoscale modeling and satellite observation of transport and mixing of smoke and dust particles over northern sub-saharan african region, *Journal of Geophysical Research: Atmospheres*, 118(21), 12,139–12,157.

1.1.3

Zender, C. S., H. Bian, and D. Newman (2003a), Mineral dust entrainment and deposition (dead) model: Description and 1990s dust climatology, *J. Geophys. Res.*, 108(D14), 4416. [B.2.1](#), [B.2.4](#), [B.3](#)

Zeng, J., Q. Han, and J. Wang (2008), High-spectral resolution simulation of polarization of skylight: Sensitivity to aerosol vertical profile, *Geophys. Res. Lett.*, 35(20), L20,801. [4.1](#)

Zhang, J., J. S. Reid, D. L. Westphal, N. L. Baker, and E. J. Hyer (2008), A system for operational aerosol optical depth data assimilation over global oceans, *J. Geophys. Res.*, 113(D10), D10,208. [B.1](#)

Zhang, Q., et al. (2009b), Asian emissions in 2006 for the nasa intex-b mission, *Atmos. Chem. Phys.*, 9(14), 5131–5153. [B.2.1](#), [B.2.4](#), [B.5.1](#), [B.4](#), [B.5.3](#), [B.5.4](#)

Zhao, Y., J. Zhang, and C. P. Nielsen (2013), The effects of recent control policies on trends in emissions of anthropogenic atmospheric pollutants and co2 in china, *Atmos. Chem. Phys.*, 13(2), 487–508. [B.4](#), [B.5.4](#)

Zhu, C., R. H. Byrd, P. Lu, and J. Nocedal (1994), L-bfgs-b: a limited memory fortran code for solving bound constrained op- timization problems, *Technique report*, Northwestern University. [3.3.3](#)

Zoogman, P., et al. (2011), Ozone air quality measurement requirements for a geostationary satellite mission, *Atmospheric Environment*, 45(39), 7143 – 7150. [B.2.2](#)

Ångström, A. (1929), On the atmospheric transmission of sun radiation and on dust in the air, *Geografiska Annaler*, 11, 156–166. [1.1.1](#)